AD NUMBER

AD864117

LIMITATION CHANGES

TO:

Approved for public release; distribution is unlimited. Document partially illegible.

FROM:

Distribution authorized to U.S. Gov't. agencies and their contractors; Critical Technology; OCT 1969. Other requests shall be referred to Army Aviaition Materiel Laboratory, Fort Eustis, VA 23604. Document partially illegible. This document contains export-controlled technical data.

AUTHORITY

usaamrdl ltr, 18 jun 1971

AD

USAAVLABS TECHNICAL REPORT 69-55

THEORETICAL AND EXPERIMENTAL INVESTIGATIONS OF V/STOL PROPELLER OPERATION IN A STATIC CONDITION

By

J. C. Erickson, Jr.

October 1969

U. S. ARMY AVIATION MATERIEL LABORATORIES
FORT EUSTIS, VIRGINIA

CONTRACT DA 44-177-AMC-379(T)
THERM ADVANCED RESEARCH, INC.
ITHACA, NEW YORK

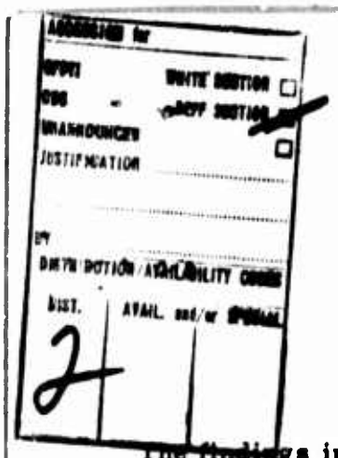

Disclaimers

The findings in this report are not to be construed as an official Department of the Army position unless so designated by other authorized documents.

When Government drawings, specifications, or other data are used for any purpose other than in connection with a definitely related Government procurement operation, the United States Government thereby incurs no responsibility nor any obligation whatsoever; and the fact that the Government may have formulated, furnished, or in any way supplied the said drawings, specifications, or other data is not to be regarded by implication or otherwise as in any manner licensing the holder or any other person or corporation, or conveying any rights or permission, to manufacture, use, or sell any patented invention that may in any way be related thereto.

Trade names cited in this report do not constitute an official endorsement or approval of the use of such commercial hardware or software.

Disposition Instructions

Destroy this report when no longer needed. Do not return it to the originator.

DEPARTMENT OF THE ARMY
HEADQUARTERS US ARMY AVIATION MATERIEL LABORATORIES
FORT EUSTIS, VIRGINIA 23604

This report represents an attempt at the development of a technique for determining the wake and performance characteristics of an isolated propeller during static thrust. Although agreement with experimental results was not satisfactory in certain portions of the wake, the data and comparisons are published for information and the stimulation of ideas.

Project 1F162204A142
Contract DA 44-177-AMC-379(T)
USAAVLABS Technical Report 69-55
October 1969

THEORETICAL AND EXPERIMENTAL INVESTIGATIONS OF V/STOL PROPELLER OPERATION IN A STATIC CONDITION

by

J. C. Erickson, Jr.

Prepared by

Therm Advanced Research, Inc.
Ithaca, New York

for

U. S. ARMY AVIATION MATERIEL LABORATORIES
Fort Eustis, Virginia

SUMMARY

The successful design of a propeller-driven V/STOL aircraft requires the precise calculation and associated optimization of the propeller performance in static operation. A general theory for performance prediction has been formulated based on a continuous vortex representation along the lines of a classical lifting-line model.

As opposed to forward flight, the deformation of the trailing vortex wake is appreciable just behind the propeller, and its determination constitutes the heart of the static thrust problem. Emphasis has been placed on determining a satisfactory force-free approximation to the effective "pitch" of the trailing vortex sheets with the contraction pattern fixed according to a heavily loaded actuator disk theory.

Numerical techniques and associated computer programs have been developed to calculate not only the inflow to the propeller but also the velocity induced along arbitrarily described deformed trailing vortex sheets. In the numerical calculations for a series of specific propellers and representative blade loadings, iterations were made on the effective "pitch" variations as well as on the inflow. Comparisons of predicted and measured performance were not completely satisfactory so far as the "pitch" iterations were pursued, but indications were that the amount of contraction should be iterated as well.

Techniques for gathering and reducing instantaneous hot-wire measurements of the wake velocity were developed. Measurements were carried out for two propellers. Non-repeatable data were obtained in large regions behind the propeller tip in both cases. Theoretical calculations could not be iterated successfully in these cases, so significant theoretical and experimental comparisons could not be made.

Detailed observations have been made on the character of the numerical computations, and certain generalizations have been made which lead to computational simplifications.

FOREWORD

The study presented in this report was undertaken by Therm Advanced Research, Inc. (TAR), Ithaca, New York, as the prime contractor, with Canadair, Ltd., Montreal, Canada, and Dr. I. S. Gartshore, McGill University, Montreal, Canada, as subcontractors. The study was sponsored by the U.S. Army Aviation Materiel Laboratories (USAAVLABS), Fort Eustis, Virginia. The authorized representative of the contracting officer was Mr. W. E. Sickles.

This is the final report prepared under Contract DA 44-177-AMC-379(T), Project 1F162204A142. A detailed report on the experimental test program (Ref. 14) was prepared by Dr. Gartshore and Mr. D. C. Gilmore. Copies of Ref. 14 have been furnished separately to USAAVLABS.

The investigation was carried out under the supervision of Drs. A. Ritter and D. E. Ordway of TAR. The principal investigator was Dr. J. C. Erickson, Jr., who is the author of this final report. Mr. A. L. Kaskel of TAR participated in the development of the numerical analysis and was responsible for the computer programs. Mr. G. R. Hough also performed some analysis. Finally, Dr. G. N. Adams, Mr. J. A. Watt, and Mr. G. Breault of Canadair were responsible for the use of the Canadair Propeller Facility and provided instrumentation for the experimental program.

CONTENTS

ILLUSTRATIONS

TABLES

SYMBOLS

AF	activity factor of propeller blade, Eq. (27)
b	local propeller blade chord, feet
C_L	blade sectional lift coefficient, Eq. (12)
C_{L_i}	blade sectional design lift coefficient
C_P	power coefficient of propeller, Eq. (17)
C_T	thrust coefficient of propeller, Eq. (16)
D_B	distance from bound vortex element $(0,r_p,\theta_p)$ to field point (x,r,θ), Table I
D_T	distance from trailing vortex element (x_v,r_v,θ_v) to field point (x,r,θ), Table I
D_p	propeller tip diameter, feet
dD	elemental profile drag on blade section, Fig. 2
dL	elemental lift on blade section, Fig. 2
$-d\Gamma$	strength of vortex sheet element trailing from $(0,r_p,\theta_p)$, Fig. 1
F/M	figure of merit, Eq. (18), percent
G_ℓ	ℓ^{th} nondimensional Glauert coefficient in representation of Γ, Eq. (22)
h/b	local propeller blade thickness-to-chord ratio
IC_{L_i}	integrated design lift coefficient of propeller blade, Eq. (28)
K_u	iteration factor chosen to achieve convergence of axial component of induced velocity field, Eq. (19)
K_v	corresponding factor for radial component, Eq. (20)
K_w	corresponding factor for tangential component, Eq. (21)

L	number of Glauert coefficients used in representation of Γ, Eq. (22)
L_u	function proportional to local curvature of the projection of a vortex trajectory in plane normal to the x-direction at (x,r,θ), Table II
L_v	corresponding function for the r-direction, Table II
L_w	corresponding function for the θ-direction, Table II
N	number of propeller blades
n	propeller rotational speed, revolutions per second
O_u	Biot-Savart operator for axial induced velocity component, Eq. (9)
O_v	corresponding operator for radial component, Eq. (10)
O_w	corresponding operator for tangential component, Eq. (11)
P	total power absorbed by propeller, horsepower
Q	component of velocity normal to intersection of the trailing vortex sheet with plane through (x,r,θ) normal to the x-axis, Table II
R_h	propeller hub radius, feet
R_p	propeller tip radius, $D_p/2$, feet
r	radial coordinate, Fig. 1
r_o	radial coordinate of point along propeller blade from which the trajectory through the sheet point (x,r,θ) trails
r_p	radial coordinate along p^{th} propeller blade, Fig. 1

r_v	radial coordinate along trajectory of vortex sheet element trailing from $(0,r_p,\theta_p)$, Fig. 1 and Eq. (7)
S_u^I	singular part of U_T for inflow point along blade, Eq. (24)
S_v^I	singular part of V_T for inflow point along blade, Eq. (25)
S_w^I	singular part of W_T for inflow point along blade, Eq. (26)
S_u^s	singular part of U_T for sheet point along trailing vortex sheet, Table II
S_v^s	singular part of V_T for sheet point along trailing vortex sheet, Table II
S_w^s	singular part of W_T for sheet point along trailing vortex sheet, Table II
S	curvilinear coordinate along intersection of trailing vortex sheet with plane normal to the x-axis, Fig. 3
T	total propeller thrust, pounds
t	parametric time for a fluid particle to move along a trailing vortex trajectory
U_B	influence function for axial component of velocity induced at (x,r,θ) by a bound radial vortex element of unit strength and unit length at $(0,r_p,\theta_p)$, Table I
U_T	influence function for axial component of velocity induced at (x,r,θ) by an arbitrarily deformed vortex sheet element of unit strength and semi-infinite length trailing from $(0,r_p,\theta_p)$, Table I
u	axial component of velocity induced at (x,r,θ), taken positive in positive x-direction, Eq. (2)
$\dot{u}$	rate of change of u with respect to t

u_p	axial inflow component at $(0,r_p,\theta_p)$, Fig. 2
u_v	axial velocity component at (x_v,r_v,θ_v)
V_B	radial counterpart of U_B, Table I
V_T	radial counterpart of U_T, Table I
v	radial component of velocity induced at (x,r,θ), taken positive in positive r-direction, Eq. (3)
$\dot{v}$	rate of change of v with respect to t
v_p	radial inflow component at $(0,r_p,\theta_p)$
v_v	radial velocity component at (x_v,r_v,θ_v)
W_B	tangential counterpart of U_B, Table I
W_T	tangential counterpart of U_T, Table I
W	total velocity at a sheet point,, Table II
W_p	total velocity seen by blade section, Fig. 2
w	tangential component of velocity induced at (x,r,θ), taken positive in positive θ-direction, Eq. (4)
$\dot{w}$	rate of change of w with respect to t
w_p	tangential inflow component at $(0,r_p,\theta_p)$, Fig. 2
w_v	tangential velocity component at (x_v,r_v,θ_v)
x	axial coordinate, Fig. 1
x_v	axial coordinate along trajectory of vortex sheet element trailing from $(0,r_p,\theta_p)$, Fig. 1 and Eq. (6)
α	local blade angle of attack, Fig. 2, degrees
β	local blade pitch setting, Fig. 2, degrees
Γ	local bound blade circulation strength

γ	tangent angle of sectional lift-drag polar, Fig. 2
Δt	time increment in marching scheme for trajectory determination
θ	azimuthal coordinate, Fig. 1
θ_p	azimuthal coordinate of p^{th} propeller blade, Eq. (1)
θ_v	azimuthal coordinate along trajectory of vortex sheet element trailing from $(0, r_p, \theta_p)$, Fig. 1 and Eq. (8)
ν_p	Glauert variable running from 0 to π with center midway between propeller hub and tip, Eq. (23)
ρ	fluid density
ϕ_p	angle between r_p and W_p, Fig. 2
φ	angle between local radius and tangent to curvilinear intersection of trailing vortex sheet and plane normal to the x-axis, Fig. 3
Ω	angular speed of propeller, Fig. 1, $2\pi n$, radians per second

INTRODUCTION

High performance in the static, or hover, operating condition is a key design condition for V/STOL propellers because the total thrust must exceed the gross weight of the aircraft for VTOL capability. Furthermore, the payload of these vehicles is typically 20% of the gross weight, so that any improvement in the static performance results in a large percentage of increase in payload capacity.

The design of high-hovering-performance propellers has been hindered by the lack of reliable theoretical methods for predicting the static performance. The principal difficulty in developing a static theory is in finding the force-free location of the trailing vortex system. This is in contrast to the forward flight theory, where the location of the trailing vortex system is determined primarily by the free-stream velocity and propeller rotation. In forward flight, the axial, radial, and tangential deformations of the sheets due to the induced velocity do not occur sufficiently close to the propeller nor in great enough magnitude to have a major effect on the performance. In static operation, however, these deformations occur immediately behind the propeller and are of such magnitude that they must be accurately represented. In fact, the axial induced velocity, which leads only to a perturbation of the pitch of the regular helical trailing vortex sheets in forward flight, determines the entire variation of the effective "pitch" in static operation.

In initial studies of the static thrust problem, we used a simple wake model in which the essential deformation was discontinuous; see Refs. 25, 7, 8 and 9. The results were generally unsatisfactory, but they did indicate that the smooth, continuous deformation of the trailing vortex system must be adequately represented. We began investigation of a continuous deformation model under U.S. Army AVLABS Contract DA 44-177-AMC-165(T) and reported the results in Refs. 10 and 11. Although a so-called refined wake hypothesis developed in that study as an approximation to the force-free condition showed promise of reasonable agreement between performance predictions and test data, it was concluded that the hypothesized wake velocities should be checked by actual computations as well as by test measurements.

In the present investigation, we have proceeded in these directions. In conjunction with Canadair, Ltd., and Dr. I. S. Gartshore and Mr. D. C. Gilmore of McGill University, the instantaneous velocity components in the wakes of two propellers have been measured (Ref. 14). Moreover, numerical techniques have been developed to compute the induced velocity components along the trailing vortex sheets. These techniques have been used to continue the development of a force-free approximation that is satisfactory for reliable performance predictions.

The theoretical formulation presented in Chapter 1 is nearly identical to that of our earlier investigation (Refs. 10 and 11), since the research described in this report is a logical development of the continuous deformation model of the earlier work. The details are repeated here to insure that this report is self-contained with all the assumptions and approximations clearly evident.

CHAPTER 1

THEORETICAL FORMULATION

Basic Equations

We consider a propeller rotating at a constant angular speed Ω in a uniform, inviscid fluid which has a density ρ and is at rest at infinity. The blade thickness-to-chord and chord-to-radius ratios are assumed to be sufficiently small that the classical lifting-line formulation should be a reasonable approximation. We can then represent the propeller blades by radial bound vortex lines accompanied by a force-free system of trailing vortex sheets.

A propeller-fixed cylindrical coordinate system (x, r, θ) is chosen with the axis of rotation as the x-axis; see Figure 1. The N blades are located in the plane $x = 0$ and are arranged symmetrically such that

$$\theta_p = 2\pi(p-1)/N \qquad p = 1, 2, \ldots, N \tag{1}$$

i.e., the $p = 1$ blade coincides with $\theta = 0$.

The induced velocity anywhere in the propeller field is determined by integration of the Biot-Savart law over all the vortex elements comprising the system in terms of their strength, orientation, and distance to the field point of interest, and may be expressed in the form

$$u = \sum_{p=1}^{N} \int_{R_h}^{R_p} \left[\Gamma(r_p)\, U_B - \frac{d\Gamma(r_p)}{dr_p}\, U_T \right] dr_p \tag{2}$$

$$v = \sum_{p=1}^{N} \int_{R_h}^{R_p} \left[\Gamma(r_p)\, V_B - \frac{d\Gamma(r_p)}{dr_p}\, V_T \right] dr_p \tag{3}$$

$$w = \sum_{p=1}^{N} \int_{R_h}^{R_p} \left[\Gamma(r_p)\, W_B - \frac{d\Gamma(r_p)}{dr_p}\, W_T \right] dr_p \tag{4}$$

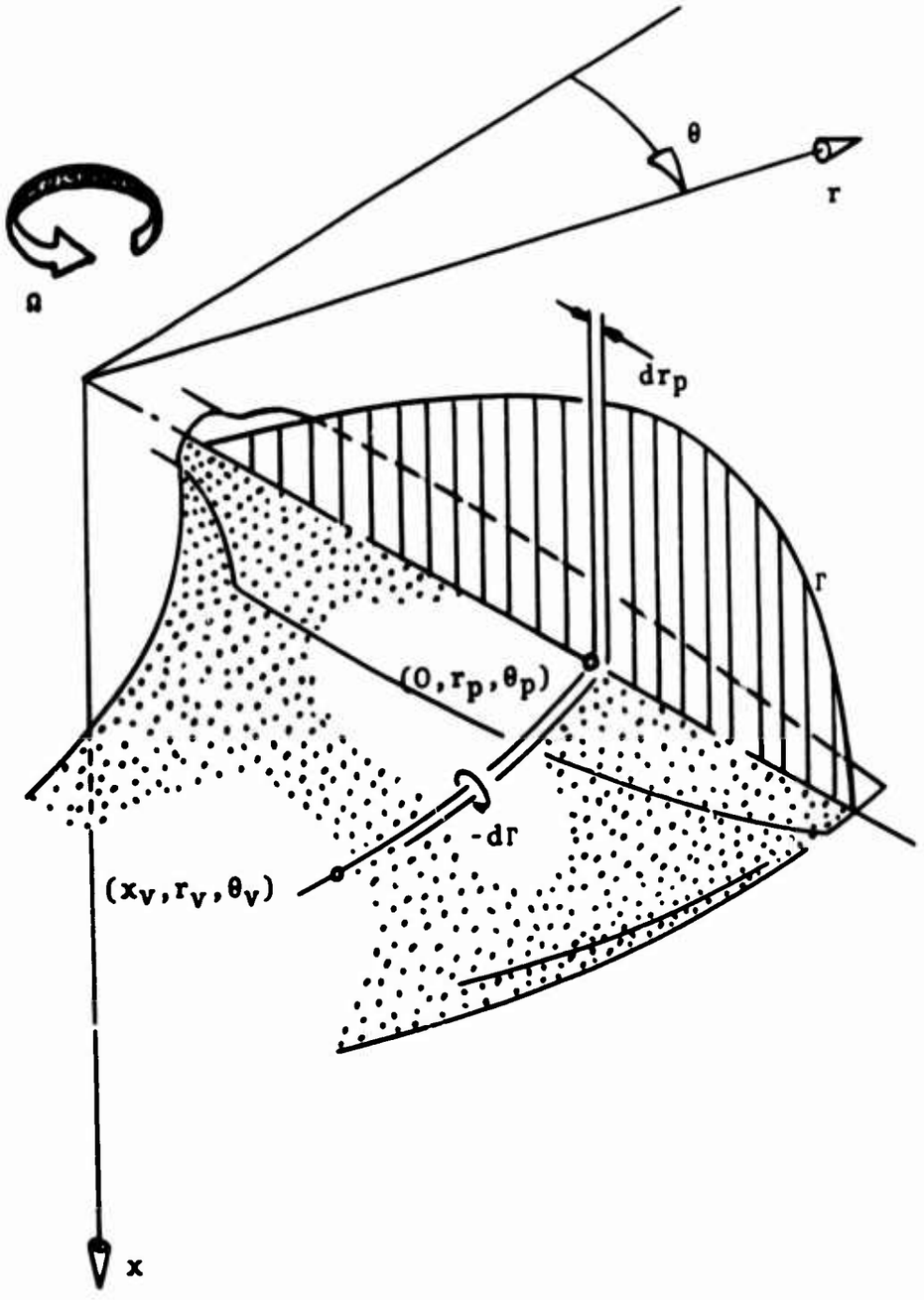

Figure 1. Propeller Coordinates and Vortex Representation.

where

u is the axial component of the velocity induced at a field point (x, r, θ) and taken positive in the positive x-direction,

v is the corresponding radial component, positive in the positive r-direction, and

w is the corresponding tangential component, positive in the positive θ-direction;

R_h is the radius of the propeller hub;

R_p is the radius of the propeller tip;

Γ is the bound blade circulation strength at $(0, r_p, \theta_p)$;

$-d\Gamma$ is the strength of the vortex sheet element trailing from $(0, r_p, \theta_p)$;

r_p is the radial variable of integration along the p^{th} propeller blade;

U_B is the influence function for the axial component of the velocity induced at (x, r, θ) by a bound radial vortex element of unit strength and unit length at $(0, r_p, \theta_p)$;

V_B is the corresponding function for the radial component, and

W_B is the corresponding function for the tangential component; and

U_T is the influence function for the axial component of the velocity induced at (x, r, θ) by an arbitrarily deformed vortex sheet element of unit strength and semi-infinite length trailing from $(0, r_p, \theta_p)$,

V_T is the corresponding function for the radial component, and

W_T is the corresponding function for the tangential component.

The influence functions can be derived from first principles (Ref. 27, pp. 1.10 - 1.12, for example), or they can be obtained from previous results (Ref. 23, pp. 13 - 16). They are summarized in Table I, where

x_V is the axial coordinate of any point on the trajectory of the vortex sheet element trailing from $(0, r_p, \theta_p)$,

r_V is the corresponding radial coordinate, and

θ_V is the corresponding azimuthal coordinate;

u_V is the value of u at (x_V, r_V, θ_V),

v_V is the corresponding value of v, and

w_V is the corresponding value of w; and

t is a time parameter to be defined.

When a point on a lifting line is chosen as a field point, the contribution from the bound vortex for this blade is irrelevant and so discarded, as in wing theory (Ref. 15, pp. 131 - 133).

The contribution from the bound vortices to the induced velocity is simple to calculate. On the other hand, the contribution to the induced velocity from the elements of the trailing vortex sheets is very complicated. Not only do the influence functions require an integration over the length of the element, but, what is even worse, the location or "trajectory" of the element is not fixed. Rather, these elements must drift force free by aligning themselves with the streamlines of the flow, which in differential form (Ref. 27, pp. 1.1 - 1.2, for example) are

$$\frac{dx}{u} = \frac{dr}{v} = \frac{d\theta}{\Omega + (w/r)} \tag{5}$$

These equations can be integrated in terms of the parametric time t that it takes a fluid particle to move along this trajectory, giving

$$x_V = \int_0^t u_V \, d\tau \tag{6}$$

TABLE I

SUMMARY OF INFLUENCE FUNCTIONS

$$U_B = - r \sin(\theta_p-\theta)/4\pi D_B^3$$

$$V_B = x \sin(\theta_p-\theta)/4\pi D_B^3$$

$$W_B = - x \cos(\theta_p-\theta)/4\pi D_B^3$$

$$D_B \equiv [r_p^2 + r^2 - 2r_p r \cos(\theta_p-\theta) + x^2]^{1/2}$$

$$D_T \equiv [r_v^2 + r^2 - 2r_v r \cos(\theta_v-\theta) + (x_v-x)^2]^{1/2}$$

$$U_T = \int_0^\infty \frac{-v_v r \sin(\theta_v-\theta) + (\Omega r_v+w_v)[r_v-r\cos(\theta_v-\theta)]}{4\pi D_T^3}\, dt$$

$$V_T = \int_0^\infty \frac{u_v r_v \sin(\theta_v-\theta) - v_v(x_v-x)\sin(\theta_v-\theta) - (\Omega r_v+w_v)(x_v-x)\cos(\theta_v-\theta)}{4\pi D_T^3}\, dt$$

$$W_T = \int_0^\infty \frac{-u_v[r_v\cos(\theta_v-\theta) - r] + v_v(x_v-x)\cos(\theta_v-\theta) - (\Omega r_v+w_v)(x_v-x)\sin(\theta_v-\theta)}{4\pi D_T^3}\, dt$$

$$r_v = r_p + \int_0^t v_v \, d\tau \tag{7}$$

$$\theta_v = \theta_p + \Omega t + \int_0^t (w_v/r_v) \, d\tau \tag{8}$$

The integrands in Eqs. (6) through (8) are functions of the coordinates along the trajectory, and the coordinates themselves are functions of t.

For convenience, we now introduce a set of operators such that Eqs. (2) through (4) become simply

$$u = O_u(\Gamma, -d\Gamma/dr; u,v,w) \tag{9}$$

$$v = O_v(\Gamma, -d\Gamma/dr; u,v,w) \tag{10}$$

$$w = O_w(\Gamma, -d\Gamma/dr; u,v,w) \tag{11}$$

where

- O_u is the Biot-Savart operator for the axial induced velocity component,
- O_v is the corresponding operator for the radial component, and
- O_w is the corresponding operator for the tangential component.

Note carefully that the operators operate on the bound and trailing vortex strengths with the velocity field itself appearing parametrically. These equations constitute a set of simultaneous, nonlinear, singular integral equations over the domain of the blades and the trailing vortex sheets. This set is complete if Γ is specified.

If Γ is not specified, another equation is required to relate the circulation strength and velocity field through

the propeller geometry. Consider the force and velocity diagram for a typical section of the blade at the radial station $(0, r_p, \theta_p)$, Figure 2, where

W_p is the total local velocity seen by the blade section,

u_p is the local axial inflow [i.e., the axial component of the induced velocity at $(0, r_p, \theta_p)$],

v_p is the corresponding radial inflow (not shown, but perpendicular to the plane of the section), and

w_p is the corresponding tangential inflow;

α is the local blade angle of attack;

β is the local blade pitch setting;

ϕ_p is the angle between Ωr_p and W_p;

γ is the tangent angle of the sectional lift-drag polar;

dD is the elemental profile drag on the blade section; and

dL is the elemental lift on the blade section.

From the definition of the sectional lift coefficient in terms of the local blade chord b, namely

$$C_L \quad 2(dL/dr_p)/\rho W_p^2 \, b \tag{12}$$

the Kutta-Joukowski formula (Ref. 27, pp. 5.21 - 5.22, for example) can be written as

$$\Gamma = b \, W_p \, C_L/2 \tag{13}$$

where the lift coefficient is assumed to be known (Ref. 6, for example) as a function of α for a given section at approximately the local Mach and Reynolds numbers. This is the equation needed in conjunction with Eqs. (9) through (11) to complete the set when the propellor geometry is specified.

$$W_p \equiv [u_p^2 + (\Omega r_p + w_p)^2]^{1/2}$$

$$\alpha \equiv \beta - \phi_p$$

$$\phi_p \equiv \tan^{-1}[u_p/(\Omega r_p + w_p)]$$

$$\gamma \equiv \tan^{-1}(dD/dL)$$

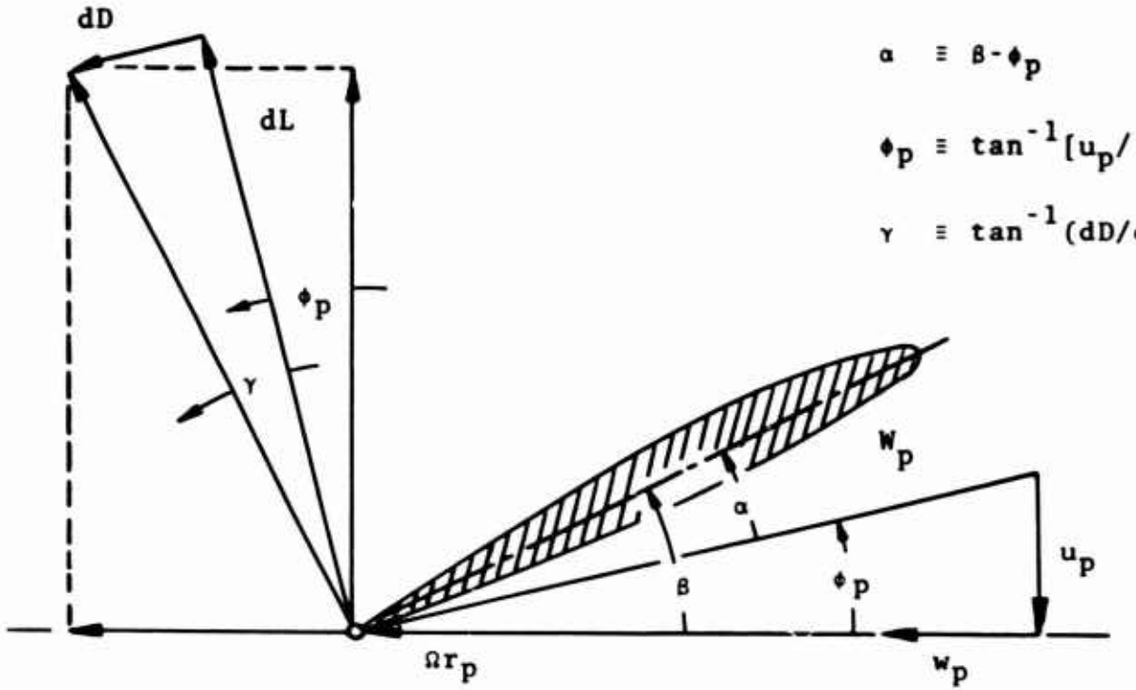

Figure 2. Velocity and Force Diagram at Typical Section.

In either case, the circulation or the propeller geometry specified, the prediction of the overall performance can be computed once the inflow has been calculated. In particular, if we resolve the resultant of dL and dD as indicated by the dotted lines in Figure 2 and integrate along the blade for the N blades, the total thrust T and power P in nondimensional form are

$$C_T = \frac{\pi^2 N}{8} \int_{R_h/R_p}^{1} C_L \frac{\cos(\phi_p+\gamma)}{\cos\gamma} \left(\frac{W_p}{\Omega R_p}\right)^2 \frac{b}{R_p} \, d\left(\frac{r_p}{R_p}\right) \tag{14}$$

$$C_P = \frac{\pi^3 N}{8} \int_{R_h/R_p}^{1} C_L \frac{\sin(\phi_p+\gamma)}{\cos\gamma} \left(\frac{W_p}{\Omega R_p}\right)^2 \frac{b}{R_p} \frac{r_p}{R_p} \, d\left(\frac{r_p}{R_p}\right) \tag{15}$$

where the thrust and power coefficients of the propeller are defined by

$$C_T \quad \pi^2 T/4\rho\Omega^2 R_p^4 = T/\rho n^2 D_p^4 \tag{16}$$

$$C_P \quad \pi^3 P/4\rho\Omega^3 R_p^5 = P/\rho n^3 D_p^5 \tag{17}$$

respectively, with $\Omega = 2\pi n$ and $R_p = D_p/2$.

From the thrust and power coefficients we can calculate the figure of merit F/M (Ref. 21, pp. 353 - 355), given in percent, by

$$F/M \equiv 100\sqrt{2C_T^3/\pi C_P^2} = 79.8\, C_T^{3/2}/C_P \tag{18}$$

To conclude this section, it is of interest to discuss the nondimensionalization of the basic equations of the static thrust problem. As we have implied by the form of Eqs. (16) and (17), the characteristic time is $1/\Omega$ and the characteristic length is R_p. If the equations are nondimensionalized with respect to these quantities, complete similarity would exist were it not for the sectional lift and drag data, which in general must include the effects of Mach number and Reynolds number, as noted earlier.

Outline of Solution

The set of equations described above cannot be solved analytically, so approximate numerical techniques must be employed. Iteration is perhaps the most straightforward approach and the one which we have chosen.

First we rewrite Eqs. (9) through (11) in a different, but equivalent, form; namely,

$$u = u - K_u[u - O_u(\Gamma, \ldots)] \tag{19}$$

$$v = v - K_v[v - O_v(\Gamma, \ldots)] \tag{20}$$

$$w = w - K_w[w - O_w(\Gamma, \ldots)] \tag{21}$$

where

- K_u is a factor chosen as necessary to achieve convergence of the axial component of the induced velocity field,
- K_v is the corresponding factor for the radial component, and
- K_w is the corresponding factor for the tangential component.

These iteration factors may be constant or may depend on any of the variables of the problem.

With the propeller geometry specified, iteration begins by finding a zeroth, or initial, approximation to the inflow and thus the blade circulation through Eq. (13), the Kutta-Joukowski formula. The first approximation to the inflow and wake velocity field follows by operating with the Biot-Savart operator on the zeroth approximation to the blade circulation and some guess at the induced velocity field in the propeller wake. These results, along with the iteration factors and the zeroth approximations to the inflow and the wake velocity field, are then substituted into the right-hand sides of Eqs. (19) through (21) to give the first approximations to the inflow and the wake velocity field,

respectively. The iteration continues by operating, as before, on the first approximations to determine a second, and so forth. Once convergence within a prescribed accuracy is reached, the propeller performance can be calculated.

On the other hand, for the case with the blade circulation specified, iteration would proceed similarly except that the circulation would not change at each step. Upon convergence in this case, the blades could be designed consistent with the Kutta-Joukowski formula, and the performance could then be calculated.

The iteration approach necessitates, at each step of the iteration, calculation of the induced velocity field at a sufficient number of points to define accurately the local streamlines in the propeller wake. Unfortunately, the number of calculations required for adequate representation of the complete distributed vortex sheets is very large. As a result, we looked for some way to reduce the number of calculations but still satisfy the force-free condition of the wake, at least in an approximate sense. This search for a simplified, yet accurate, iterative approach to the prediction of static propeller performance has been the goal of both the earlier and the present investigations.

The question of convergence and the proper choice of the iteration factors in Eqs. (19) through (21) have proved to be important and difficult. They will be treated in depth in our discussion of the numerical results in Chapters 4 through 6.

Continuous Deformation Model

The trailing vortex sheets of a propeller, in general, stretch axially, together with a radial contraction and a tangential distortion. The edges of the sheets are also locally unstable and tend to roll up as for a finite wing.

While these deformations are not of primary significance for the practical determination of aircraft propeller performance for the usual forward flight operating conditions (Ref. 2), they are the heart of the static problem. Without a free stream, not only do the deformations occur much closer to the propeller and so exert more influence, but they are also much larger. In fact, the axial elongation which is only a perturbation of the basic helical sheets in forward flight now determines the total variation of the effective "pitch" of the sheets.

At the beginning of our earlier investigation (Refs. 10 and 11) we decided, on the basis of previous studies (Refs. 7 through 9 and 25), that there was a clear lack of fundamental knowledge on the nature of the roll-up process for propellers. Moreover, we had found that it was important to represent especially well the axial and radial deformation of the distributed trailing vortex sheets immediately behind the propeller. Therefore, we decided at that time to concentrate on the continuous axial stretching and radial deformation of the trailing vortex sheets or, in other words, a "Continuous Deformation Model". In the present investigation we have continued to develop this model with principal emphasis on improvement of the force-free approximation, especially with regard to the axial deformation. This development proceeded throughout the numerical computations of this study and is described in Chapters 4 through 6, including comparisons with test data wherever possible.

Implementation

In order to carry out even approximate iterative solutions to the set of equations that we have formulated, it is necessary to use digital computation techniques, especially for the Biot-Savart operators in Eqs. (2) through (4). Accordingly, we have developed a very general computer program (CODEFVEL); see Chapter 2 of Ref. 10. This program evaluates the Biot-Savart operators for field points (x, r, θ) located on the lifting line or anywhere else except on the trailing vortex sheets proper. CODEFVEL also contains many options for treating wake models other than the Continuous Deformation Model. All of this generality leads, unfortunately, to extremely time-consuming and complicated data preparation (see Appendix I of Ref. 10).

In the present investigation we have developed two separate, simplified programs that are specialized to compute either the inflow at field points along the lifting line only (INFLOWPT), or the velocity induced at field points downstream along the trailing vortex sheets only (SHEETPT). Both of these programs are based upon CODEFVEL, but they do contain many improvements that were indicated by our experience. INFLOWPT, SHEETPT, and the associated numerical analysis for each are described in full in Chapters 2 and 3, respectively.

Once the inflow has been computed, the propeller circulation distribution and performance can be found from Eqs.

(13) through (15) and (18). A short program (PROPERFM) has been developed for this, and it is described in Chapter 2 as well.

Instructions for the preparation of input data are given in Appendix I for all the programs.

CHAPTER 2

METHOD OF INFLOW AND PERFORMANCE COMPUTATION

Description of Computer Programs

Program INFLOWPT was developed from CODEFVEL, as mentioned in Chapter 1, to provide a simpler, quicker means of evaluating the inflow Biot-Savart operators for arbitrary axial, radial, and tangential deformation of the trailing vortex sheets in the Continuous Deformation Model. Just as we had developed a short program (VORTTRAJ) from CODEFVEL for computing only selected trajectories of the trailing vortex elements, we found it convenient to abstract an analogous short program (MRCHINFO) from INFLOWPT. MRCHINFO has the additional option, if desired, of computing the inflow influence functions of the trailing elements as well as their trajectories.

Program PROPERFM was written as an independent program for evaluating the propeller blade circulation and performance. Although provisions were made for its eventual inclusion in INFLOWPT as a series of subroutines, this was not practical for the numerical computations that were actually performed.

The programs were all written in FORTRAN 63 for the CDC 1604 computer. The particular machine that we used was located at the Cornell University Computing Center. A duplicate FORTRAN 63 deck of each program has been cut and supplied to USAAVLABS along with a set of complete listings. Brief operating instructions are provided in Appendix I.

Representation of Circulation Distribution

In general, the blade circulation distribution Γ is tabulated numerically at several radial stations, but for the subsequent integrations in Eqs. (2) through (4) we need Γ in analytic form. A suitable form is a Glauert-type series (Ref. 15, pp. 138 - 139), or

$$\Gamma = \Omega R_p^2 \sum_{\ell=1}^{L} G_\ell \sin\ell \quad \psi_p \qquad (22)$$

$$r_p \equiv 1/2(R_p+R_h) - 1/2(R_p-R_h) \cos \theta_p \qquad (23)$$

where

G_ℓ is the ℓ^{th} nondimensional Glauert coefficient, and

θ_p is the Glauert variable which runs from 0 to π with its center midway between the hub and tip.

This form possesses a square-root behavior at both the tip and the hub. For the tip, this is the proper behavior required for a lifting-line formulation (Ref. 5 pp. 171 - 174, for example). For the hub, it is approximately correct when the blade necks down rapidly at the shank, as on some propellers. On the other hand, when the hub is like the root of a wing, the slope of the circulation distribution should be zero from a rigorous viewpoint. This could have been achieved exactly by an additional condition on the determination of the Glauert coefficients, but practically the contribution of the hub to the overall performance is so small that zero slope can be achieved with or without this condition.

The Glauert coefficients are evaluated by the method of least squares, which minimizes the error at the specified data points (Ref. 26, pp. 363 - 370). INFLOWPT provides for the numerical values of Γ to be given at up to 100 points, with L as high as 25. Usually L = 10 was the best compromise between the accuracy of the Γ fit and the introduction of extraneous fluctuations into the shape of its derivative. This point will be discussed at greater length in the section on checks of the program and also in the section on the calculations for the 12.6° pitch setting of the 65 AF propeller in Chapter 6.

Influence Functions for a Trailing Vortex Element

As pointed out earlier, we must in general calculate the trajectories of the elements of the trailing vortex sheets in order to evaluate the contribution by these sheets to the induced velocity. The method described here is used in INFLOWPT for each element of a distributed, continuous representation of the trailing vortex sheets. However, the

method, and the influence functions computed by it, would be equally applicable to a discrete vortex representation of the trailing sheets.

Physically, most of the wake deformation occurs just downstream of the propeller, say, within a distance of a blade radius or so. Therefore, numerical integration of Eqs. (6) through (8) is necessary only in this region, since farther downstream the trajectories may be approximated as regular helices with suitable pitch.

To carry out the trajectory integrations, a prescribed velocity field along the trailing vortex sheets, either from a guess or from the preceding step of the iteration, has to be stored in the computer as input data. Though the real flow field is not axisymmetric, we need not consider the θ variation because we are always moving along trajectories that are the same for all blades at a given radius. The stored velocity field is specified at a maximum of 30 values each of x and r and 3-point Lagrangian interpolation, first in r and then in x, carried out for the other values in between. We found that for each of 12 radial stations, 9 axial stations were adequate to represent the velocity field between the propeller plane and 1.5 propeller radii downstream.

With the velocity field stored, the trajectory is evaluated in a step-by-step marching scheme using a two-term constant slope method. The first step off the blade is made by multiplying the inflow components by a small, but arbitrary, time increment Δt to find the new location of the vortex sheet element. The second and successive steps are taken by interpolating to determine the velocity at this new location, multiplying it by $2\,\Delta t$, and adding the result to the coordinate of the previous location. With this scheme, the error is of the order of the cube of Δt as opposed to the square of Δt, which an ordinary two-term Taylor series would afford. The increment Δt is constant as the march proceeds, but the increment may be changed to new values at up to nine points downstream to speed the march by increasing and decreasing the Δt increment where allowable. At each change in increment size, the two-term constant slope march begins again as it does from the blade.

Simultaneously with this march, it is convenient to perform the integrations over t for evaluation of the contribution of this deformed trailing vortex element to the influence functions; see Table I. The integrands are calculated at each new location in the march for the element

from each blade, are summed over all the blades, and are integrated by the trapezoidal rule. Running totals of the influence functions are carried as the march proceeds.

The trajectories and influence functions from this scheme were compared, by means of MRCHINFO, with corresponding results from CODEFVEL. After a series of investigations, we settled, for a four-bladed propeller, on 45 marching steps at $\Omega\Delta t = 0.01$, 63 at 0.05, and the remainder at 0.10. For a three-bladed propeller, we took 55 steps at 0.01, 40 at 0.05, and the remainder at 0.10. The march along each trajectory automatically terminates when either all of the specified steps have been taken or the downstream cutoff limit of the input velocity field has been reached, whichever occurs first. In practice, we always specified sufficient steps at $\Omega\Delta t = 0.10$, say, 500, so that each march terminated at a specified cutoff point 1.5 propeller radii downstream. This means of ending the march provides a great time savings over CODEFVEL, in which all elements took the same number of steps. This number was dependent on insuring that the "slowest" element reached the cutoff.

When the termination point is reached, each trajectory is assumed to be of regular helical shape with pitch determined from the axial and tangential velocity components at that point. The computation of the influence functions can then be completed by approximating the contributions of this regular helical part that trails downstream from the termination point to infinity. This approximation consists, as in CODEFVEL, of computing the θ-average of the contributions using results of the theory of the Generalized Actuator Disk (Ref. 17, pp. 13 - 15). The calculation involves simply the evaluation of some well-defined function; namely, the Legendre functions of the second kind and degree plus and minus one-half and the Heuman lambda function. We chose to evaluate the Legendre functions by relating them to the complete elliptic integrals of the first and second kinds (Ref. 3, p. 249), which are computed using a rational approximation (Ref. 1, pp. 591 - 592). For the Heuman lambda function, we took an exact series expansion (Ref. 3, p. 300) and related it, also, to the complete elliptic integrals of the first and second kind. These integrals are calculated as before. Where applicable, the addition formula for the Heuman lambda function (Ref. 3, p. 36) is employed to speed convergence of the series.

Inflow Induced by the Trailing Vortex Sheets

Once the influence functions have been computed, integration of the second terms in Eqs. (2) through (4) must be carried out. We have chosen to perform these integrations for a continuous, distributed trailing vortex sheet representation. Unfortunately, the singularities of the integrand complicate the picture, and special treatment is required in order to carry out these integrations quickly and accurately.

We first see that the square-root behavior of Eq. (22) makes the strength of the elements of the trailing vortex sheets infinite at the hub and the tip. This is no problem, though, if we carry out the integrations in terms of the Glauert variable instead of the original radial variable.

A second and more serious difficulty is the existence of singularities which arise in the influence functions because each inflow point coincides with an element of the trailing vortex system. The nature of these singularities can be determined by direct investigation of the integrands of the influence functions in Table I, but the actual strength of the singularities is dependent upon the particular path along which the inflow point is approached. This path must be determined by the location of the elements of the trailing vortex sheet immediately adjacent to the inflow point, since it is the induction of these elements that gives rise to the singularity. Thus, for inflow points, this path is the radial coordinate along the lifting line. This radial direction is tangent to the trailing vortex sheet at the lifting line but, in general, is not normal to the individual trailing elements due to their contraction. However, the resulting singularity will be nonintegrable over the radius unless the radial inflow is zero there, so that the trailing elements are normal to the lifting line. This is the same nonintegrable singularity that has arisen in attempts to extend lifting-line theory to swept-back wings (Refs. 13, 28, and 20, for example). We handled this difficulty by allowing the first few steps in the marching scheme to be taken with zero radial velocity and constant axial and tangential velocity, i.e., as regular helical elements, after which the trailing elements deform in the desired fashion. Generally we have taken two such steps. We will discuss this point further in the section on the calculations for the 12.6° pitch setting of the 65 AF propeller in Chapter 6.

With elimination of this nonintegrability, we are left with two types of singularities, Cauchy and logarithmic, as shown elsewhere (Ref. 24, pp. 14 - 16). To handle the

integration over these singularities, we break the results into "singular" and "regular" parts. Once the singularity strengths have been determined analytically from the basic equations by approaching the inflow point along the proper radial path, we can define

$$S_u^I \equiv \frac{\Omega r+w}{4\pi[u^2+(\Omega r+w)^2]^{1/2}} \frac{1}{r_p-r} - \frac{(\Omega r+w)^3}{8\pi r[u^2+(\Omega r+w)^2]^{3/2}} \ln \left| \frac{r_p-r}{R_p} \right| \tag{24}$$

$$S_v^I \equiv 0 \tag{25}$$

$$S_w^I \equiv - \frac{u}{\Omega r+w} S_u^I \tag{26}$$

where u and w are the input inflow at r. These singular parts then can be integrated analytically in the usual principal value sense with the derivative of Γ found by differentiation of Eq. (22).

The regular parts for each element of the trailing vortex sheets are determined numerically by subtracting the singular parts from the summation over all the blades of the influence functions. The radial location of the elements is chosen automatically in INFLOWPT by specifying as input an integer number of basic divisions of the 0 to π interval of integration over the Glauert variable. Since the major part of the induction is by the outboard trailing elements, the accuracy of integration is improved by automatically halving the basic division size between $2\pi/3$ and π; i.e., outboard of approximately the 0.8 radial station. Vortex elements are also automatically added close to either side of each inflow point to provide better definition of the regular parts. These elements are used for that inflow point only, and any basic elements falling nearer the inflow point are excluded in the interest of numerical accuracy. The regular parts of the total integrand can be found at any desired station by multiplying the regular parts of the influence functions there, as found from the computed values by 3-point Lagrangian actual integration over the Glauert

variable is carried out by a generalized Gaussian integration scheme. In this scheme, a 10-point Gaussian quadrature is first applied to the total interval of integration. The total interval is in turn subdivided into two intervals, the 10-point Gaussian quadrature is applied to each of these intervals, and the results are added to get the answer. Next, the total interval is subdivided into three intervals, and so on. At each step after the second, the answer is compared with the two values which immediately precede it, and the subdivision is continued until these three values are within a desired accuracy.

Program INFLOWPT can accommodate up to 200 trailing vortex elements and can compute the inflow at up to 40 points. Generally we considered 8 inflow points with basic elements every $\pi/6$, giving a total of 25 trailing elements. The accuracy specified for the Gaussian integration was $\pm$ 0.00005 of the tip rotational speed.

Calculation of Propeller Performance

Program PROPERFM is used to compute the propeller blade circulation distribution and performance by means of the equations in Figure 2 and Eqs. (13) through (15) and (18). The essential inputs are the blade geometrical parameters, the two-dimensional sectional lift and drag data at approximately the local Mach and Reynolds numbers, and the inflow. These data are read in at each desired blade section with the lift coefficients over a range of angles of attack, as well as the drag coefficients either over a range of lift coefficients or over a range of angles of attack given in tabular form. It is necessary to prepare these sectional data in advance by hand. We used the basic Curtiss-Wright data (Ref. 6) extended to high angles of attack by the methods of Ref. 12. Other data could be used equally well, but small changes would have to be made in the program. The integrations in Eqs. (14) and (15) are carried out over the radial variable by means of the generalized Gaussian integration scheme described above.

Checks of Computer Programs

Many checks were made in order to gain confidence in programs INFLOWPT, MRCHINFO, and PROPERFM, as well as to determine the best choice of the input parameters for insuring quick, yet accurate, results.

Initially we checked MRCHINFO and INFLOWPT by duplicating cases that we had run by CODEFVEL for both three- and four-bladed propellers. Successful completion of these checks gave us confidence in the compatibility of the new programs with the earlier one.

An independent check was afforded by comparing our results with existing ones for a particular marine propeller in cruise. We had made calculations earlier of the induced velocity at field points external to the blades and regular helical wake of this propeller for the Naval Ship Research and Development Center using CODEFVEL. Excellent agreement was found by S. B. Denny (Ref. 4) between our results and comparable ones computed with a program developed by J. E. Kerwin (Ref. 18). For completeness we also checked both CODEFVEL and INFLOWPT by computing the inflow to this propeller. The agreement of the axial inflow with that of Kerwin was everywhere within 2.5%, with the worst discrepancies near the hub and tip. These were traced to differences in the fit of Γ and were an early indication of this sensitivity, which we will discuss below.

Besides this comparison of inflow calculations, we also found excellent agreement between our computed influence functions for regular helical elements and tabulated results by W. B. Morgan (Ref. 22). We concluded that our computational methods are indeed adequate in the case of propellers in cruise with regular helical trailing vortex sheets.

Once the computational scheme and computer programs had been checked in this fashion against our previous results as well as against independent ones, we examined the effect on the inflow of varying certain input parameters. By means of numerical experimentation with MRCHINFO and INFLOWPT, we determined the choices that we have described in the previous sections for the numbers of marching steps and their associated increment sizes, the number of elements needed to represent the distributed trailing vortex sheets, the number of points at which the input velocity field must be specified, and the number of Glauert coefficients in the blade circulation fit.

The most important of these is the number of Glauert coefficients for fitting Γ. Numerical experiments with the marine propeller, for which we did not have Γ data outboard of the 0.9 radial station, indicated that small percentage changes in Γ between the 0.9 station and the tip can lead

to much larger percentage changes in the singular part of the axial inflow in the same region. This occurs because the singular part of the axial inflow near the tip, and hub as well, is very sensitive to the higher order Glauert coefficients, being roughly proportional near the hub and tip to the summation to L of the products of the coefficients times the square of their order ℓ. In contrast, Γ is proportional to the summation of the coefficients alone, and its derivative is proportional to the summation of the coefficients times their order. Thus, small changes in the Γ fit near the hub or tip can change the higher order coefficients enough that the changes in Γ become amplified in the singular part of the inflow. Unfortunately, this occurs near the tip where the accuracy of the inflow is most important.

We checked PROPERFM by comparing the predicted performance of the Curtiss-Wright 3(13168A10P3) propeller with the hand calculations report earlier (Ref. 10, p. 52). The differences were on the order of 1 to 2% in thrust and power coefficients and about 1/2% in figure of merit. They arise due to the change from the trapezoidal integration by hand to the generalized Gaussian scheme in PROPERFM.

CHAPTER 3

METHOD OF VORTEX SHEET VELOCITY COMPUTATION

Description of Computer Program

Program SHEETPT was developed from both CODEFVEL and INFLOWPT to provide a means of computing the Biot-Savart operators for field points located on trailing vortex sheets which may have arbitrary axial, radial, and tangential deformation. The basic method of computation is identical to INFLOWPT in most respects. Exceptions are that the actual location of the field points on the sheets must be determined, the singular parts appropriate to these points evaluated, and the velocity induced by the bound blade vortices calculated. All of these differences are described in this chapter.

This program, too, was written in FORTRAN 63 for the CDC Computer, and a duplicate deck and listing have been supplied to USAAVLABS. Brief operating instructions are provided in Appendix I.

Determination of Sheet Point Locations

The first task in computing the velocity along the trailing vortex sheets is to determine the actual location (x, r, θ) of the field points. It is desirable for our purposes to calculate the velocity at several axial positions x along the trajectories from each of several different radii, r_o, say, along the lifting line. Therefore, to determine r and θ for each x and r_o, we must march along each of these elements exactly as we do in the calculation of the influence functions. When the step is taken that goes beyond the first specified x, the march stops, and a 3-point Lagrangian interpolation with this point and the two preceding ones is used to determine r and θ at this x. Next, the velocity components are found at this x as at any point on the sheets by the basic interpolation in the input velocity field. Finally, a numerical differentiation technique based on 3-point Lagrangian interpolation is used to find the time rate of change along the trajectory of the velocity components at the field point. These will be used later in computing the logarithmically singular parts of the influence functions. The march then resumes until r and θ have been determined similarly for all specified x locations.

Program SHEETPT provides for following elements downstream to as many as 10 axial stations from as many as 20 radial stations. Generally, we considered four typical radial stations and four axial stations. It turned out to be more efficient in computing costs to make several runs for each case with each run treating one or two axial locations.

Influence Functions for a Trailing Vortex Element

The marching scheme for determining the trajectories and influence functions in SHEETPT is nearly identical to the one in INFLOWPT. There is one significant difference, though, to insure accurate integration of the influence functions when the trajectories are close to the field points. The march proceeds as usual until it reaches a specified axial distance from each field point x location. There the march automatically changes to a smaller Δt increment, which is used until the march has reached an equal distance beyond the field point. Then the march resumes and continues as usual. This occurs around each x location. Outside of these intervals, the step numbers and increment sizes are specified as in INFLOWPT. The march terminates identically to INFLOWPT, and the regular helical contributions to the influence functions are computed in the same way.

After some numerical experimentation, we settled on a series of step and increment sizes which we used for both three- and four-bladed propellers. In runs with axial locations x of 0.05 and 0.2 propeller radius, we used five marching steps at $\Omega\Delta t = 0.01$ and 500 at 0.05 initially off the lifting line, 500 at 0.05 between the 0.05 and 0.2 stations, and 70 at 0.05 and 500 at 0.10 downstream of the 0.2 station. Within a Δx of 0.043 propeller radius on either side of the field points, $\Omega\Delta t = 0.01$ was used and the march was terminated at 1.7 propeller radii downstream; i.e., 1.5 radii beyond the 0.2 station to be consistent with INFLOWPT practice. In runs where only the axial location x of 0.5 propeller radius was considered, we took five steps at 0.01 and 500 at 0.05 initially and 70 at 0.05 and 500 at 0.10 downstream of 0.5 radius. Within 0.060 propeller radius on each side of 0.5, $\Omega\Delta t = 0.01$ was used and the march was terminated at 2.0 propeller radii downstream. Finally, for axial locations x of 1.0 propeller radius, we used five steps at 0.01, 20 at 0.10, and 500 at 0.05 initially with 70 at 0.05 and 500 at 0.10 downstream of the 1.0 radius. Within

0.060 on either side of 1.0 propeller radius, we used $\Omega\Delta t$ = 0.01 and terminated the march at 2.5 propeller radii downstream.

Vortex Sheet Self-Induced Velocity

Integration of the second terms of Eqs. (2) through (4) is carried out for the sheet points in exactly the same fashion as for the inflow. Singularities again occur when the sheet point and an element of the trailing vortex sheets coincide. Here, too, we can separate the integrand into singular and regular parts so that the integration can be carried out exactly as for the inflow.

The nature of the singularities can be found by direct investigation of the integrands in Table I, and their strengths of the singularities can be found be approaching the sheet point (x, r, θ) along the path appropriate to the adjacent elements of the trailing vortex sheet. To find this path, we examine the curvilinear line which is formed by the intersection of the trailing vortex sheet with the plane passing through the sheet point normal to the x-axis; see Figure 3. The appropriate path is then along this curvilinear line or, in the limit as the point (x, r, θ) is approached and the singularity strengths are determined, along the tangent to the line at the point.

This path is not normal to the trajectory through the sheet point because the radial velocity is generally not zero. However, this is not a problem in this case, because the trajectory extends upstream of the point as well as downstream, and so the singularity is integrable. It is precisely this feature that makes J. Weissinger's (Ref. 31) approximation of placing the lifting line at the one-quarter-chord line and satisfying the downwash at the three-quarter-chord line possible for finite swept wings. The singularities are integrable at the three-quarter-chord line, whereas they are not at the one-quarter-chord line where the trailing vortex sheet originates.

Numerical determination of this path of approach requires computation of the angle γ, which the curvilinear intersection line makes with the local radius through the sheet point. This is done by carrying out marches to determine the r and θ of two closely adjacent points on the intersection line. Once these are found, γ is computed by numerical differentiation of a 3-point Lagrangian interpolation through these two added points and the sheet point.

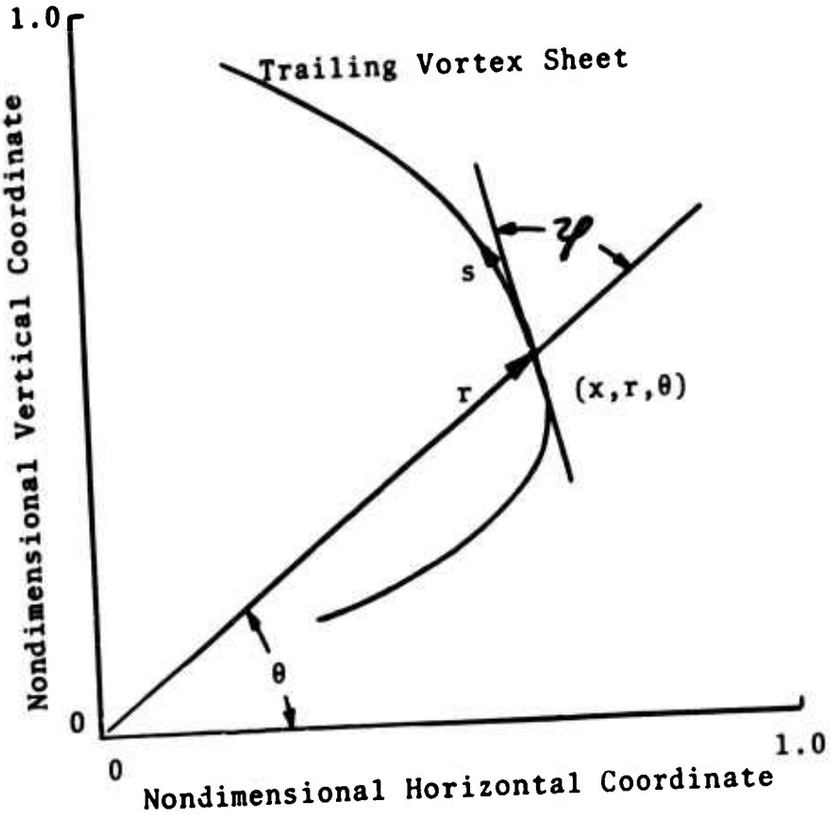

Figure 3. Intersection of Trailing Vortex Sheet With Plane Passing Through (x,r,θ) Normal to x-Axis.

A suitable choice for the location of these added trajectories is coincident with those particular vortex elements which are added to provide better definition of the regular parts, just as in INFLOWPT.

The strengths of the resultant Cauchy and logarithmic singularities can be found analytically from the basic equations by assuming approach along the tangential path. However, the strengths are in terms of a distance along the intersection from the adjacent vortex elements to the sheet point, while the integrals in the second terms of Eqs. (2) through (4) are over the radial coordinate along the lifting line. This is best handled by transforming the distance along the intersection, as measured by a curvilinear coordinate S (see Figure 3), to the radial coordinate r_o along the lifting line. This transformation requires only the computation of the trajectories adjacent to each sheet point. The local dS/dr_o is found by numerical differentiation of the 3-point Lagrangian interpolation among the 3 points. The singularity strengths are now completely determined in terms of the radial coordinate r_o along the lifting line.

The singular parts can now be defined and are given in Table II, where

L_u is a function proportional to the local curvature of the projection of the trajectory in the plane normal to the x-direction at (x, r, θ),

L_v is the corresponding function for the r-direction, and

L_w is the corresponding function for the θ-direction;

Q is the component of the input velocity normal to the intersection of the trailing vortex sheet with the plane through (x, r, θ) normal to the x-axis;

$\dot{u}$ is the rate of change of the input axial velocity component u at (x, r, θ) with respect to the parametric time t along the trajectory,

$\dot{v}$ is the corresponding derivative of v, and

$\dot{w}$ is the corresponding derivative of w; and

W is the total input velocity at the sheet point (x, r, θ).

TABLE II

SINGULAR PARTS OF INFLUENCE FUNCTIONS FOR FIELD POINTS ALONG TRAILING VORTEX SHEETS

$$S_u^s \equiv \frac{W[(\Omega r+w)\cos\ -v\ \sin\ ]}{2\pi Q^2\ (dS/dr_o)}\ \frac{1}{r_p-r_o} + \frac{L_u}{4\pi r W^3}\ \ln\left|\frac{r_p-r_o}{R_p}\right|$$

$$S_v^s \equiv \frac{W\ u\ \sin}{2\pi Q^2(dS/dr_o)}\ \frac{1}{r_p-r_o} + \frac{L_v}{4\pi r W^3}\ \ln\left|\frac{r_p-r_o}{R_p}\right|$$

$$S_w^s \equiv -\frac{Wu\ \cos}{2\pi Q^2(dS/dr_o)}\ \frac{1}{r_p-r_o} + \frac{L_w}{4\pi r W^3}\ \ln\left|\frac{r_p-r_o}{R_p}\right|$$

$$W^2 = u^2 + v^2 + (\Omega r+w)^2$$

$$Q^2 = u^2 + [(\Omega r+w)\ \cos\ \ - v\ \sin\ ]^2$$

$$L_u = -(\Omega r+w)^3 - v^2(\Omega r+w) - v^2\Omega r - rv\dot{w} + r(\Omega r+w)\dot{v}$$

$$L_v = (\Omega r+w)uv + \Omega ruv - r(\Omega r+w)\dot{u} + ru\dot{w}$$

$$L_w = (\Omega r+w)^2 u - ru\dot{v} + rv\dot{u}$$

The singular parts of the self-induced velocity components along the trailing vortex sheets can be found by analytical integration exactly as in INFLOWPT. Finally, the regular parts of the velocity components are computed exactly as in INFLOWPT. The basic element spacing and integration accuracies were chosen the same as with INFLOWPT for consistency.

Velocity Induced by Bound Blade Vortices

The contribution of the bound blade vortices to the induced velocity at field points downstream along the trailing vortex sheets is in general not zero. Since these sheet points do not coincide with the bound vortex elements, the appropriate influence functions are regular throughout the range of interest. This, combined with the algebraic form of these functions and the fixed location of the elements, makes the integration of the first terms of Eqs. (2) through (4) relatively straightforward.

The integration is carried out by means of the generalized Gaussian integration scheme. The integrands of Eqs. (2) through (4) are computed at the radial stations required in the scheme by multiplying the calculated influence functions at these required radial stations by the corresponding values of Γ calculated from Eq. (22). The accuracy used in the integration was ± 0.00005 of the tip rotational speed to be consistent with the velocity induced by the trailing vortex sheets.

Checks of Computer Program

Several checks of SHEETPT were made initially in order to gain confidence in the program as well as to begin interpreting and using its results to achieve a better approximation to the force-free condition on the trailing vortex sheets. Unfortunately, there were few comparable previous results available for checking purposes. This meant that the checking and especially the interpretation of SHEETPT computations continued throughout the entire investigation and will be treated subsequently.

The only check that could be made was for the special case of a propeller in cruise with the assumption of regular helical trailing vortex sheets; so we computed the sheet velocities for the marine propeller that we had considered in the INFLOWPT and MRCHINFO checks. Even here we had no

basis for comparisons of the total induced velocity on the sheets although we could check most of the intermediate steps. For example, the singularity strengths computed from the equations in Table II reduced correctly to twice the strengths computed for this propeller in INFLOWPT, according to Eqs. (24) through (26). The factor of two arises because the trajectories extend upstream as well as downstream through the sheet points. More important, the computed influence functions checked with analytical results based on the symmetry properties afforded by integration along regular helical trajectories. This check involved the use of MRCHINFO for obtaining integrations to finite distances along the trajectories. The interpretation and subsequent use of the final results for this example will be treated in Chapter 4.

A number of runs were then made for a sample case with deformation present. This case was a first approximation and so was by no means close to a converged solution of the equations. Nevertheless, it was a good example for checking because there was a large amount of deformation present in the trailing vortex sheets. Most of the procedure for calculation of the singular parts was checked by hand since these parts constitute the principal differences between SHEETPT and INFLOWPT. A number of minor improvements were made as a result of these detailed examinations. We also investigated the effects of varying some of the input parameters to determine the best choices of marching step increment sizes Δt and locations of the added trajectories that are required for computing γ and dS/dr_o. Finally, in order to help explain certain features observed for the radial variation of the influence functions, a few points were recomputed with only the trailing vortex sheet from one blade present. This gave a clear indication of the strong aerodynmaic interference among the trailing vortex sheets, especially downstream, where the deformation becomes more pronounced.

From all of these computations and checks, we realized that the complicated numerical operations involved, coupled with the large and sometimes locally severe deformations of the sheets, would make careful investigation of all subsequent results necessary. However, even if the velocity at 1 or 2 points for each case seemed to be unusual or difficult to explain, still, overall, the results appeared to be reasonable.

CHAPTER 4

INITIAL THEORETICAL RESULTS

Review of Wake Hypothesis Development

The investigations described in Refs. 10 and 11 were begun with our initial wake hypothesis as an approximation to the force-free condition of the wake. This hypothesis utilized the variations of the three velocity components with distance downstream along constant radii that are predicted by the theory of the generalized actuator disk (Ref. 17). Computations for two different propellers indicated that the predicted performance was excessively optimistic compared with test data. Moreover, preliminary wake velocity test data showed that although the predicted contraction pattern of the envelopes of the elements of the trailing vortex sheets was realistic, the predicted effective "pitch" variations of the elements of the trailing vortex sheets were not. We concluded that most of our attention should be directed toward the determination of the "pitch" variations.

The resulting refined wake hypothesis was based on the initial hypothesis, but changes were made in an attempt to overcome the above difficulties. This refined hypothesis, or force-free approximation, was identical to the initial hypothesis inboard of the 0.5 radial station. Outboard, the axial velocity variations were applied along streamlines instead of along constant radii; i.e., along the trajectories of the elements of the trailing vortex sheets. The radial velocity variations were fixed by assuming that both the initial and refined hypotheses should give the same contraction pattern. After an encouraging preliminary trial, the refined hypothesis was used on a third propeller, and good agreement with performance test data was obtained after three successive approximations. However, a subsequent fourth approximation suggested that less favorable agreement might occur for a fully converged solution. By this time we had concluded that for whatever wake hypothesis we developed, it would be necessary to check the assumed velocity components along the trailing vortex sheets by actual computations and, where feasible, by corresponding test data.

This conclusion was reinforced by a set of independent, unpublished computations for another propeller design. We were unable to achieve a convergent inflow iteration using

the refined wake hypothesis. Not only was the axial inflow becoming unreasonably high over midblade and negative near the tip, but also the amount of contraction was becoming excessive. In turn, agreement with performance test data grew poorer with each successive approximation.

Once program SHEETPT had been written and basically checked, we turned to the four-bladed, 7-foot-diameter 65 Activity Factor (AF) propeller at a pitch setting of 12.6°, as measured at the 0.7 radial station. The blade characteristics of this propeller are given in Appendix II. The airfoil section data appropriate to a tip speed of 800 feet per second and the zeroth approximations to the axial inflow and blade circulation Γ were determined on the basis of Refs. 6 and 12, the same as for the 3(13168A10P3) propeller (see pp. 37 and 40 of Ref. 10). The radial inflow was guessed, and the tangential inflow was found from the generalized actuator disk result, $-N\Gamma/4\pi r$. A first approximation to the inflow and Γ was calculated on the basis of the refined wake hypothesis and displayed characteristics of previous unsuccessful iterations. So, instead of iterating, the first approximation to the induced velocity components along the trailing vortex sheets was computed for elements trailing from the 0.4, 0.7, 0.9, and 0.975 radial stations.

The computed variations of the axial induced velocity u with the distance x downstream increased considerably more rapidly than the assumed variations based on the refined wake hypothesis. In fact, some appeared to reach asymptotic values greater than the limit of 2.0 which is inherent in regular helical wakes. In Figure 4 we have plotted the x-variation of u computed along the trajectory from the 0.9 radial station. This and all subsequent variations are normalized by the corresponding inflow value. For comparison we have also plotted the variations of u assumed in the refined wake hypothesis and those computed for the marine propeller described in the previous chapter. It must be noted that the variations plotted are the trailing contributions only. To these must be added the contribution from the bound blade vortices. This contribution is usually much less than 10% of the trailing contribution. The bound contribution also fluctuates in sign as a function of azimuthal location of the sheet point in question and decays rapidly with x. We have neglected the bound contributions throughout the investigation because they add only a higher order refinement to the basic variations and are significant only when a true, force-free solution is approached more closely than we have been able to approach it.

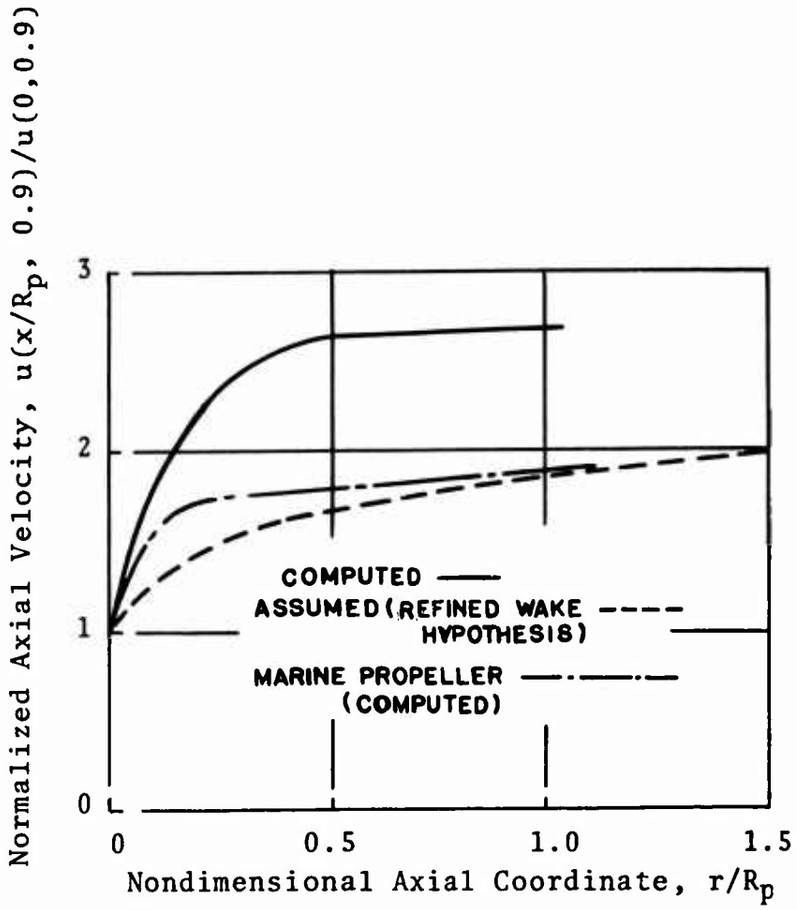

Figure 4. Comparison of Assumed and Computed x-Variation of Axial Induced Velocity Along Trajectory From $r_o/R_p = 0.9$, 65 AF Propeller, $\beta 0.7R_p = 12.6°$, Refined Wake Hypothesis.

The computed x-variations of the radial velocity v indicated initially that more contraction is required, but downstream the results were not clear at all. The computed x-variations of the tangential velocity w increased very rapidly to approach apparent asymptotic values, which are greater than the mean value found by conservation of the circulation. It should be recalled that w is small compared to the local propeller rotational velocity Ωr and so is of secondary importance.

On the basis of the evidence we gathered through all applications of the refined wake hypothesis as well as through the comparisons of the assumed and computed velocity variations, we concluded that the refined wake hypothesis did not provide a representation of the wake that is generally adequate. We continued to feel strongly that the effective "pitch" of the trailing vortex system was the most important feature of the wake, provided that a reasonable contraction pattern existed. Moreover, it appeared that it would be advisable to compute the x-variations of the induced velocity components early in the iteration to aid in obtaining an adequate "pitch" representation and so a force-free solution.

Formulation of New Wake Representation

Simultaneously with our conclusions that the refined wake hypothesis was inadequate as a general approximation to the force-free condition of the wake, new results were obtained at Therm Advanced Research, Inc., by M. D. Greenberg and A. L. Kaskel (Ref. 16) for an exact, force-free actuator disk model of a propeller or rotor in static operation, in and out of ground effect.

The model in Ref. 16 considers the θ-average or, equivalently, the infinite blade number representation of a propeller or rotor with a constant blade circulation distribution and zero hub radius. The trailing vortex system consists of a line vortex along the axis of rotation and a deformed vortex tube from the tip. The exact kinematic and dynamic equations have been solved numerically for the entire flow field. This formulation has the property that, if the tangential velocity w is neglected, the entire streamline contraction pattern is analytically independent of the total loading. If w is included, the pattern is numerically virtually independent of the total loading. This contraction pattern out of the ground effect, illustrated in Figure 5, agrees reasonably well with available flow visualization results.

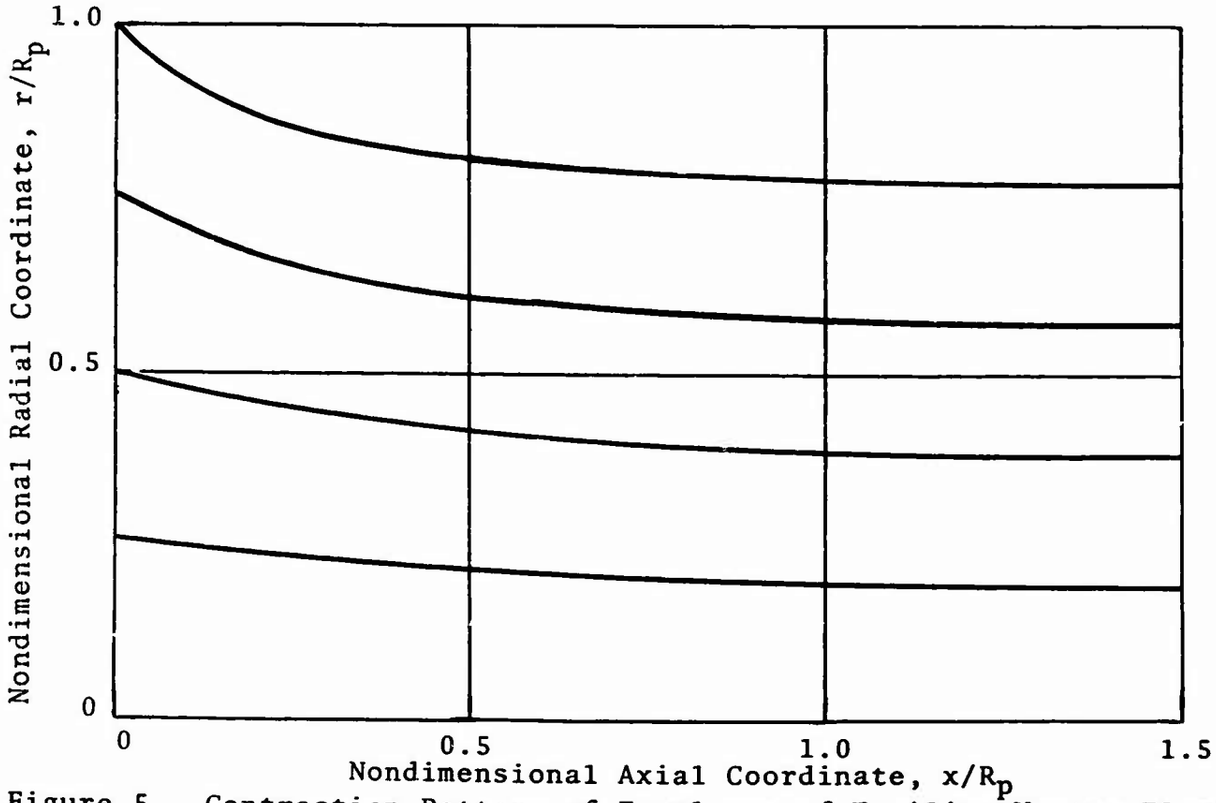

Figure 5. Contraction Pattern of Envelopes of Trailing Vortex Elements, New Wake Representation Based on Ref. 16.

The first important feature of our new wake representation is the specification of the contraction pattern by these actuator disk results; i.e., the ratio of the radial-to-axial velocity components v/u is fixed along each element of the trailing vortex sheets by Ref. 16. This is incorrect far inboard because the radial velocity is usually positive there due to the effect of the distributed trailing vorticity, but this region has very little effect outboard. Also, the x-variations of the tangential velocity w along all the trajectories are fixed according to the values computed for the 65 AF propeller at the 12.6° pitch setting. This leaves the x-variations of the axial velocity u, which determine the effective "pitch" along the trajectories of the elements of the trailing vortex sheets, as the principal variables at our disposal for approximating a force-free wake.

This representation of the wake insured in advance a reasonable contraction pattern and allowed us to concentrate on working toward the force-free effective "pitch." However, v is computed along with the other components, and this permitted us to draw conclusions afterwards about the validity of the assumed fixed contraction pattern.

65 AF Propeller, 12.6° Pitch Setting - Initial Computations

The first case treated by means of the new wake representation was again the 12.6° pitch setting of the 65 AF propeller. We started from the same zeroth approximations and based the x-variations of the axial velocity u on the computations for this case with the refined wake hypothesis.

Three successive approximations to the inflow and blade circulation were computed, and the axial inflow, although initially reasonable, was beginning to diverge as we had observed for some of the refined wake hypothesis computations. Therefore, we computed the third approximation to the x-variations of the velocity components along the trailing vortex sheets. The x-variations of u increased less rapidly with x than assumed inboard of the 0.9 radial station, but at the 0.975 station the x-variations increased much more rapidly and reached a higher asymptotic value.

The outboard variations were modified accordingly to agree with the computed values, and the inflow was recomputed with the second approximation as input. The resulting axial inflow seemed to be too low over midblade and too high at the tip. We decided that when modifying the variations, we should not make changes to the full extent indicated by the

computed variations. Therefore, we changed the variations to lie roughly halfway between the previous two sets and again recomputed the inflow with the second approximation as input. The axial inflow seemed to be reasonable, but the recomputed x-variations of u were close to those assumed initially. We repeated this cycle of changing the x-variations of u and recomputing the inflow and x-variations once more. A convergent trend did seem to be emerging in the x-variations of u, but the inflow and blade circulation were still not close to convergence. Furthermore, the entire iterative process was very inefficient and unwieldy, so we suspended calculations for this case. The calculations were resumed later and are described in Chapter 6.

65 AF Propeller, 8.2° Pitch Setting

We turned our attention next to the 8.2° pitch setting of the same 65 AF propeller operating at a tip speed of 800 feet per second. This case is significant because the instantaneous velocity components in the propeller wake had been measured by means of hot-wire anemometry in the experimental portion of this investigation. These data were obtained to guide and check the theoretical computations. The azimuthal variations of the axial and radial velocity components at several points in the wake are presented in Appendix III, while the full details of the acquisition and reduction of the data are contained in the test report prepared by D. C. Gilmore and I. S. Gartshore of McGill University, Ref. 14.

The theoretical calculations began by obtaining zeroth approximations to the inflow and blade circulation in the same way as for the 12.6° pitch setting of this propeller. We selected the same x-variations of u along the trailing vortex sheets that we had used originally for the 12.6° setting and computed a first approximation to the inflow.

The axial inflow was nearly 50% higher over midblade but was strongly negative outboard of the 0.95 radial station. This held no promise for a successful iteration, so we modified the x-variations of u outboard of the 0.95 station to increase more rapidly with x and to reach a higher asymptotic value. The inflow was then recomputed but still held no promise for iteration because the axial inflow was essentially unchanged outboard.

We examined the wake velocity data next to assess their use as a guide for achieving convergent theoretical computations. A principal feature of the measurements was that

a hot-wire signal which repeated with each blade passage (see Figure 6, for example) could be obtained only in a limited region behind the middle of the blade. On the other hand, inboard near the hub and outboard near the tip, the signal was apparently completely random (see Figure 7) and did not repeat for each blade passage. The extent and growth downstream of the nonrepeatable region are shown in Figure 8 for this case, as well as for the 120 AF propeller at the 10.0° setting; see Chapter 6. Beyond the outer limit of this region and upstream of the propeller, a periodic signal was again obtained. We have been unable to explain the cause of the random signals.

The randomness precluded a meaningful resolution of the basic data into the instantaneous velocity components, and so, practically, we do not have useful data in the tip region. In our theoretical computations, it is the "pitch" of the trailing vortex sheets in this tip region that is most important, because the tip elements principally control the level of the inflow over the rest of the blade. Thus, the absence of data in the tip region limits the use of the wake data to checking the computed values over midblade; that is, the data can be used as a check but not as a guide in defining the "pitch" where the "pitch" is most important. Therefore, in this case where we were unable to iterate successfully, the data were not of immediate use.

The principal difficulty in iterating appears to be an underloading of the propeller near the tip. This was observed in the zeroth approximation where the blade circulation Γ was very low. The indicated negative axial inflow near the tip in the first approximation would lead to a larger Γ there, but we were unable to treat negative axial velocities with any confidence. When the axial velocities are very small, as in the zeroth approximation, or negative, as in the first, the exact location of the trailing vortex elements is extremely important because small changes in their position can cause large interference effects, as we found in earlier studies (see pp. 31 and 33 of Ref. 10).

In view of the difficulties encountered in our theoretical computations, we changed our approach significantly at this point in order to overcome these difficulties. The computations toward this end are described in the next chapter.

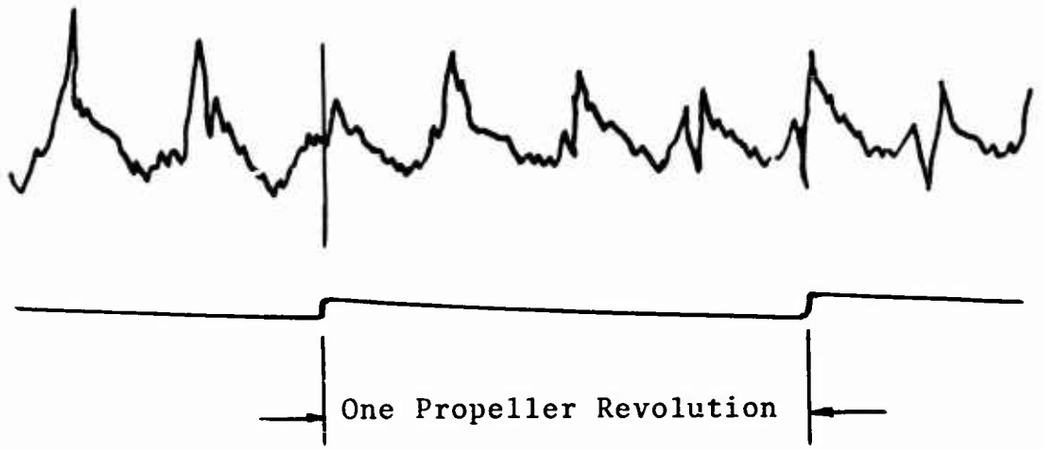

Figure 6. Oscillograph Trace of Typical Hot-Wire Signal Repeatable With Blade Passage; 65 AF Propeller, $\beta 0.7R_p = 8.2°$, $x/R_p = 0.5$, $r/R_p = 0.5$.

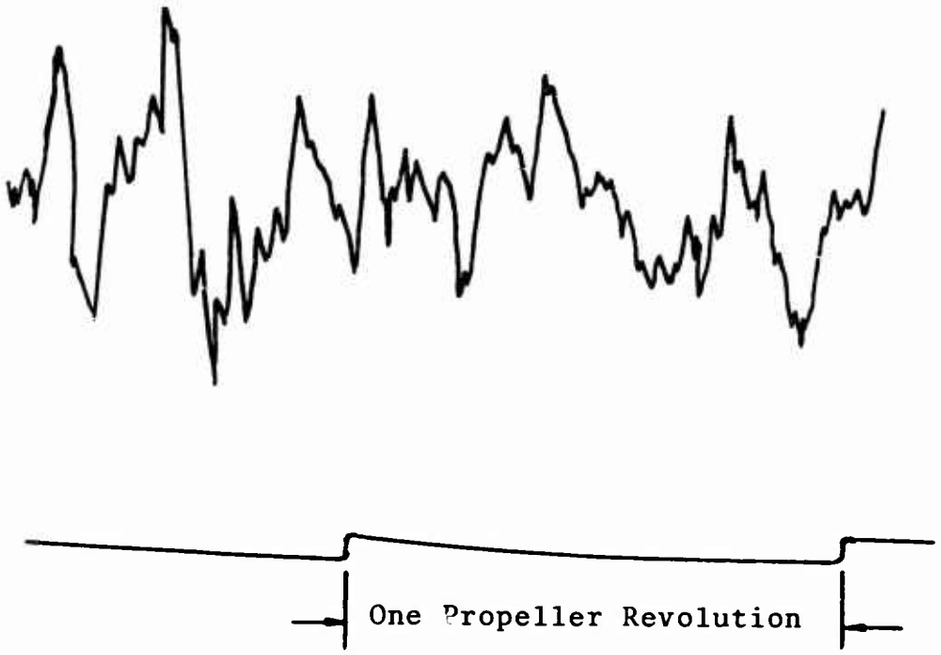

Figure 7. Oscillograph Trace of Typical Hot-Wire Signal Nonrepeatable With Blade Passage; 65 AF Propeller, $\beta 0.7R_p = 8.2°$, $x/R_p = 0.1$, $r/R_p = 0.85$.

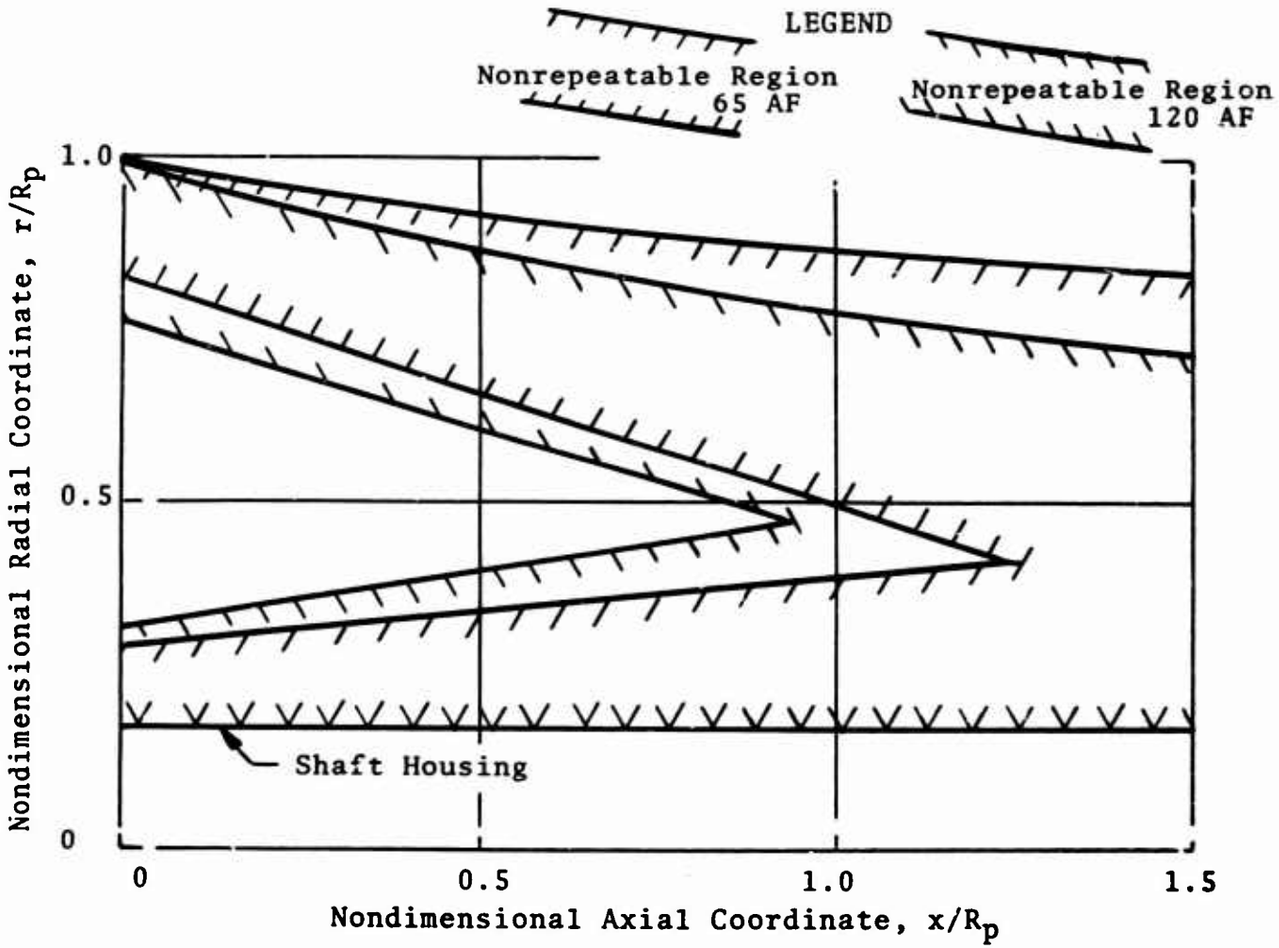

Figure 8. Extent and Growth of Regions of Nonrepeatable Hot-Wire Signals; 65 AF Propeller, $\beta 0.7R_p = 8.2°$; 120 AF Propeller, $\beta 0.7R_p = 10.0°$.

CHAPTER 5

THEORETICAL RESULTS FOR REPRESENTATIVE BLADE LOADINGS

General

An approach that an experienced propeller designer might find useful as an aid in th development of improved blade designs can be outlined as follows. First, a desired blade circulation distribution Γ or, equivalently, a blade loading distribution would be assumed. The solution for the corresponding inflow components would then be found and used in conjunction with Γ to determine an actual blade design. The utility of this approach rests ultimately, of course, on a proven, suitable method for calculating the inflow; i.e., a method that is based on a force-free wake and that has been verified by comparisons with test data for widely varying existing propeller designs.

In the stage of our theoretical development when computations for representative blade loadings were under taken, such computations could only serve to demonstrate the feasibility of such an approach. On the other hand, the same approach offered an important simplification computationally, since Γ remains fixed throughout the iteration and Eq. (13) is not needed in conjunction with Eqs. (2) through (4) to find the inflow. We pursued this approach at this point of the investigation because of the promise it offered in providing important experience and insight into the attainment of force-free solutions to Eqs. (2) through (4).

We selected both a four-bladed Γ, called Representative Blade Loading One (RBL 1), and a three-bladed Γ, called RBL 2. Each of these distributions was found by extrapolating T. Theodorsen's moderate loading extension of the Goldstein optimum analysis (see Eq. (1) on p. 23 of Ref. 29) to zero advance. Contraction was ignored in this extrapolation, and each Γ was truncated to a hub radius at the 0.1 radial station. Both distributions were selected to have comparable loadings and are based upon a "displacement velocity at infinity downstream" (see Ref. 29) of 1/6 of the propeller tip speed. The corresponding induced thrust coefficients (found by eliminating the lift coefficient between Eqs. (13) and (14) while simultaneously neglecting profile drag losses; i.e., $\gamma = 0$) are 0.161 for RBL 1 and 0.154 for RBL 2. The circulation distributions for RBL 1 and RBL 2 are plotted later along with the computed inflow in Figure 9 and 11, respectively.

The zeroth approximations to the axial and tangential components of the inflow were found from the equations implicit in the analysis of M. Knight and R. Hefner (Ref. 19). In particular, the axial inflow is the square root of $N\Omega\Gamma/4\pi$, and the tangential inflow is the familiar $-N\Gamma/4\pi r$. However, we faired both components to finite values at the tip to be more realistic.

Representative Blade Loading One

The four-bladed case, RBL 1, was considered first. With the blade circulation Γ fixed and the zeroth approximations to the inflow determined as above, it remained only to specify the x-variations of the axial velocity u along the trajectories. We chose variations which increased with x initially off the blade at rates consistent with our preceding computations but which reached asymptotic values of exactly 2.0. These variations, then, are not greatly different from those assumed in the refined wake hypothesis and so have some basis in our previous results.

Four successive approximations to the inflow were computed. The axial iteration factors used with Eq. (19) differed from one approximation to the next as we proceeded cautiously toward a solution. We followed this procedure throughout the computations for RBL 1 and RBL 2. Tangential iteration factors of 1.0 were generally taken throughout. The fourth approximation to the axial inflow, with an iteration factor of 1.0, converged to within ±4.0% of the third approximation everywhere along the blade and to within ±1.1% outboard of the 0.9 radial station. We judged this to be sufficient convergence for checking the x-variations of u downstream. The fourth approximations to the axial and tangential inflow are plotted in Figure 9 along with Γ and the zeroth approximations.

In Figure 10 are plotted the assumed radial inflow used as an input to the calculation of the fourth approximation; i.e., as fixed by the assumed contraction pattern and the third approximation to the axial inflow, and the computed fourth approximation with a radial iteration factor of 1.0. The contraction pattern is clearly inadequate inboard, as we knew in advance. However, the agreement outboard is fairly good except that near the tip the indications are that the fixed pattern is providing too much contraction. Finally, the computed induced power coefficient (found by eliminating the lift coefficient between Eqs. (13) and (15) with $\gamma = 0$) is 0.0476 and leads to an induced figure of merit of 108%.

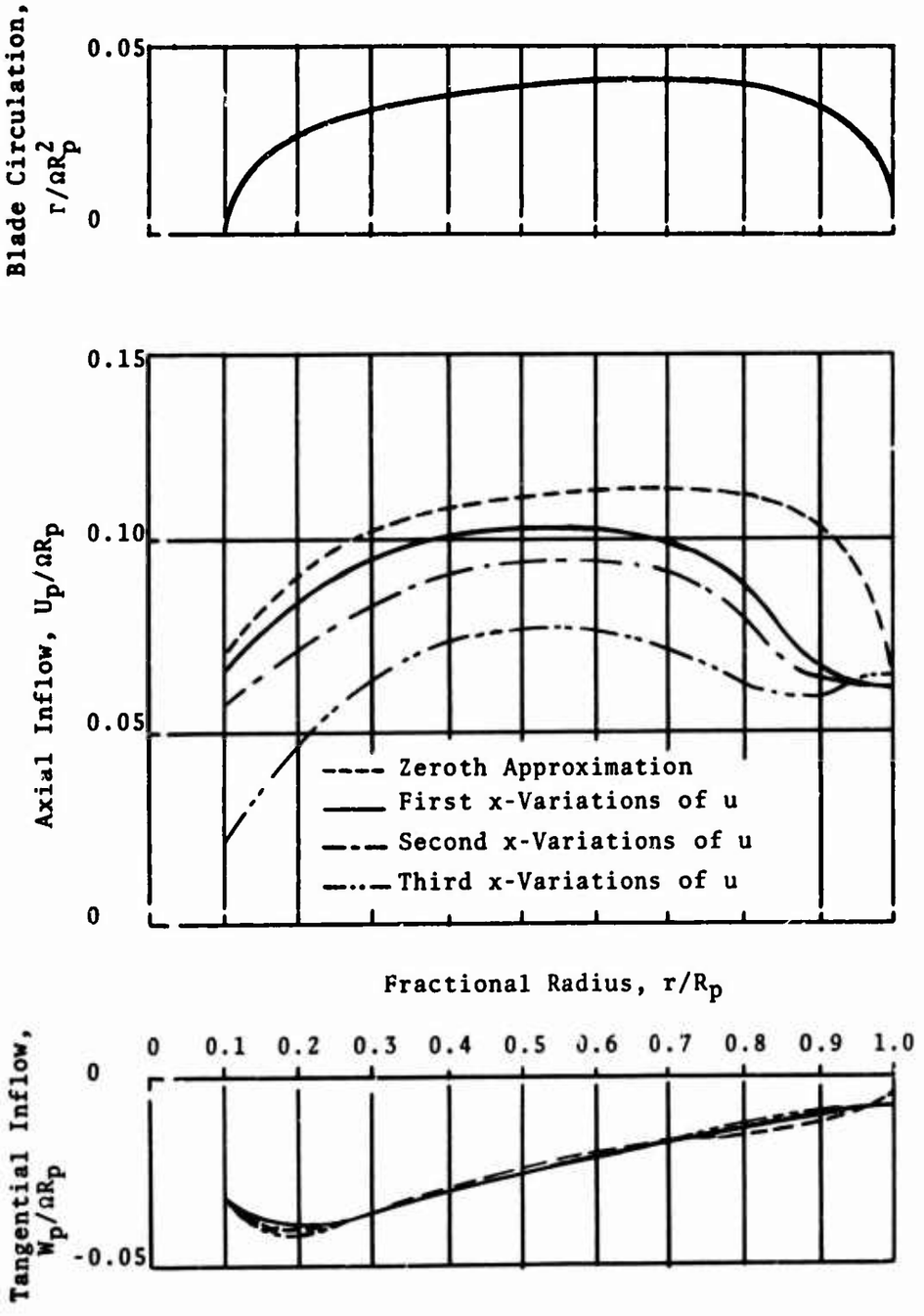

Figure 9. Blade Circulation and Axial and Tangential Inflow, Representative Blade Loading One, First, Second, and Third Assumed x-Variations of Axial Velocity.

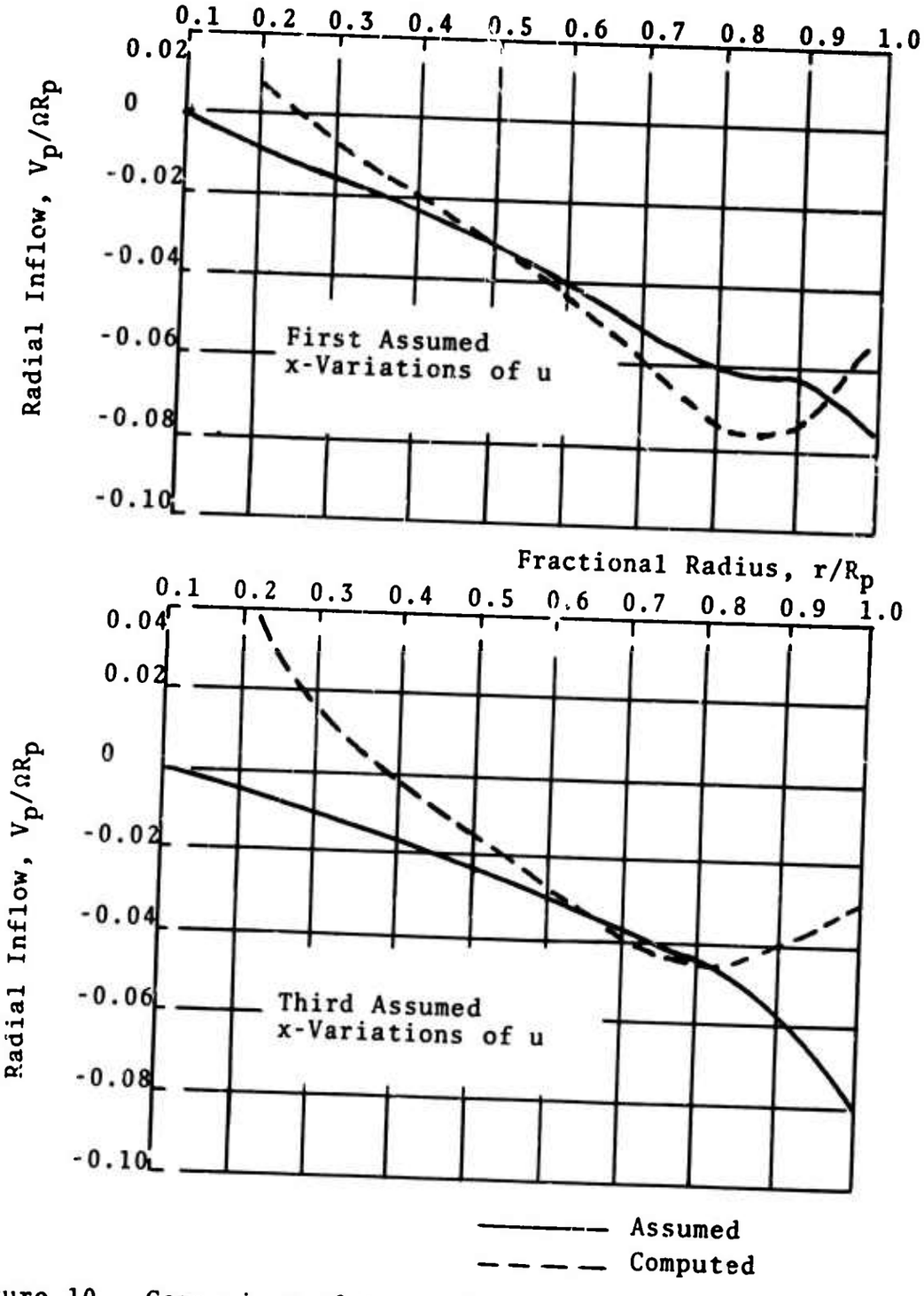

Figure 10. Comparison of Assumed and Computed Radial Inflow, Representative Blade Loading One, First and Third Assumed x-Variations of Axial Velocity.

The next step was to compute the fourth approximation to the x-variations of the induced velocity components along the trailing vortex sheets. At the 0.4 and 0.7 radial stations the computed x-variations of u increased less rapidly with x than assumed, while at 0.9 and 0.975 they increased more rapidly. In light of our experience with the 65 AF propeller, we changed the variations by only about one-third of the differences between the assumed and computed variations. This was performed, moreover, in two steps. First, we changed the variations outboard of the 0.8 station only and computed the inflow. Then we changed the variations inboard of 0.8 as well and recomputed the inflow. The axial inflow between the two differed by less than 1.0% over the entire blade. This gave valuable confirmation of our earlier conclusions that it is the outboard variations that need to be represented more accurately.

With these x-variations as finally modified, and beginning with the previous third approximation as the zeroth, two successive approximations to the inflow were computed. The axial inflow, which converged to within $\pm$1.7% everywhere and within $\pm$0.2% outboard of the 0.9 station, is also plotted in Figure 9. The assumed and computed radial inflow comparison was somewhat poorer than for the first set of variations. The induced performance became even less reasonable, too, with a power coefficient of 0.0434 and a figure of merit of 119%.

The corresponding second approximation to the x-variations of the induced velocity components was computed. Surprisingly, the computed x-variations of u were virtually identical to those computed with the first set of assumed variations, so we modified them to the full extent indicated.

Assuming this third set of x-variations of u and taking the immediately previous first approximation as the zeroth, three successive approximations to the inflow were computed. The axial inflow, again shown in Figure 9, converged to within $\pm$1.5% everywhere along the blade. The comparison of the assumed and computed radial inflow is presented in Figure 10, and agreement is even poorer than for the first two sets of x-variations of u. Furthermore, the indications are clearer that the fixed pattern provides too much contraction. The trend to less reasonable induced performance continued with a power coefficient of 0.0355 and a figure of merit of 145%.

Both the second and third approximations to the x-variations of the induced velocity components were computed with this assumed set of variations. The axial inflow

differed between these two approximations by less than ±5.0% and then only in the sense that the second did not have the minimum at the 0.9 radial station (see Figure 9) but was instead nearly constant outboard of 0.8. At the 0.4 and 0.7 radial stations, the computed x-variations of u were nearly identical in the two cases and were very close to the assumed variations. However, at the 0.9 station especially, and to a lesser degree at the 0.975 station, the computed x-variations of u were markedly different in the two approximations. Both approximations increased with x at close to the assumed rates initially. However, the second approximations continued to increase at close to the assumed rates, while the third approximations reached maxima at about 0.2 blade radius downstream and then decreased. The apparent cause of these large differences is the pronounced change in the degree of distortion of the trailing vortex sheets, resulting from differences in axial inflow which are relatively small in magnitude but which vary rapidly with radius. In particular, these gradients in axial velocity outboard led to a local stretching out of the trailing vortex sheets in the third approximation that was not present in the second. Therefore, for conservation of circulation, the trailing vorticity outboard is more thinly distributed over the sheet in the third approximation. Consequently, the induced velocity is considerably smaller.

These computations completed consideration of RBL 1. We will discuss the results more fully after a description of the RBL 2 computations which were carried out next.

Representative Blade Loading Two

Similar computations were made for RBL 2 with the blade circulation and the zeroth approximations to the inflow based on Ref. 19, as described earlier. To provide comparisons with RBL 1, we selected the same set of x-variations of the axial velocity u that we had used initially for RBL 1.

Three successive approximations to the inflow were computed. The convergent trend was rapid, and the third approximation to the inflow was within ±1.0% of the second. The axial and tangential inflows are plotted in Figure 11 along with Γ and the zeroth approximations. Qualitatively, the assumed and computed radial inflows differed like they did in the third set of x-variations of u for RBL 1. The induced performance is even less realistic than the comparable RBL 1 case, with a power coefficient of 0.0406 and a figure of merit of 119%.

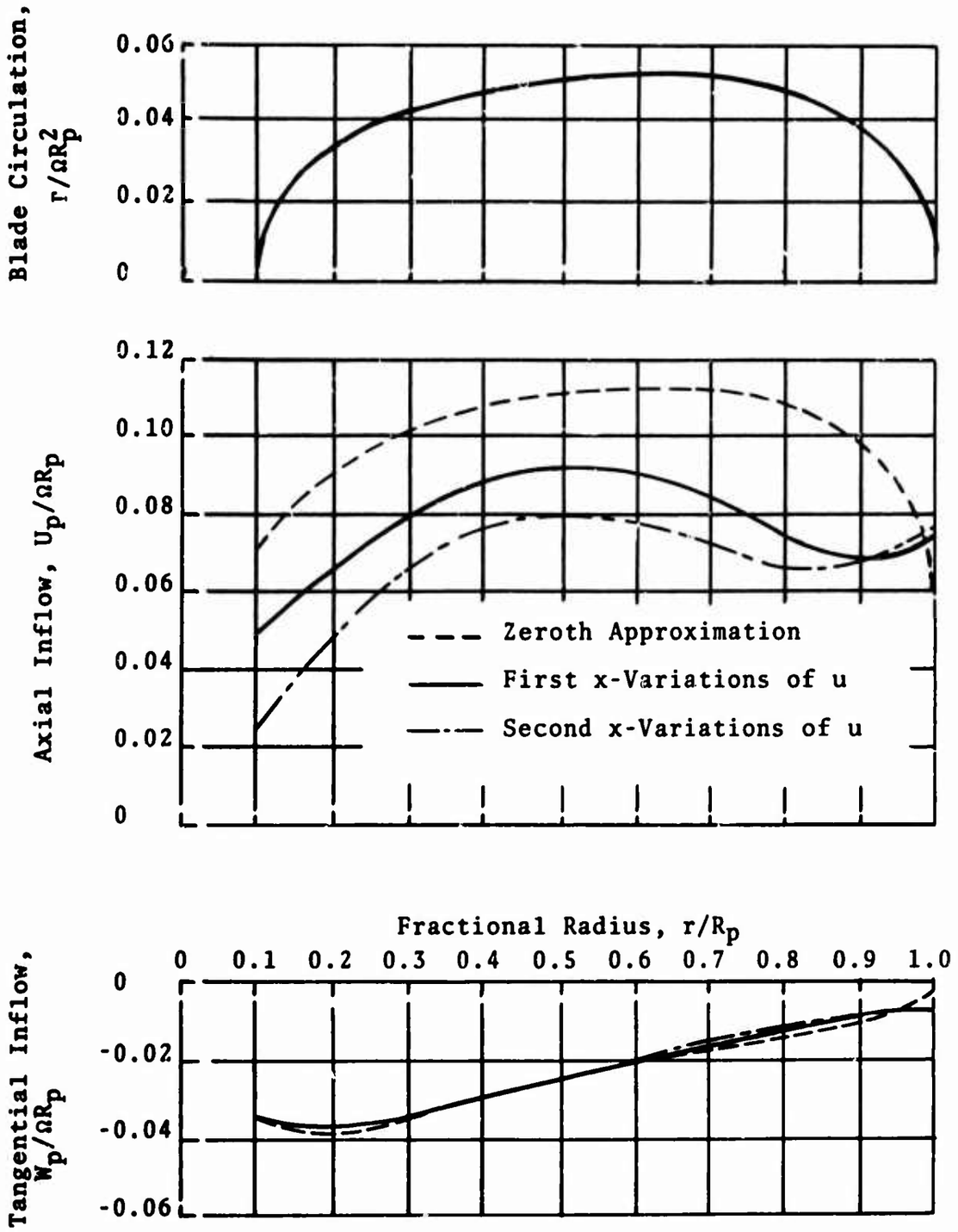

Figure 11. Blade Circulation and Axial and Tangential Inflow, Representative Blade Loading Two, First and Second Assumed x-Variations of Axial Velocity.

Next, the third approximation to the x-variations of the induced velocity components along the trailing vortex sheets was computed. At the 0.4 and 0.7 radial stations, the computed x-variations of 7 increased less rapidly with x than assumed, just as for RBL 1. At 0.9, the computed variation increased more rapidly than assumed initially and then leveled off at a higher asymptotic value. At 0.975, the computed variation also increased more rapidly initially but then reached a maximum and subsequently decreased; see Figure 12. This is the same behavior that we observed for RBL 1. We then modified the x-variations of u to be identical with the third set of variations for RBL 1 inboard of the 0.85 station and to follow the newly computed RBL 2 variations outboard of 0.85, simply ignoring the decrease after the maximum; see Figure 12.

With the second set of x-variations of u, and with the previous second approximation as the zeroth, two successive approximations to the inflow were computed. The second approximation to the axial inflow, which converged to within $\pm 2.6\%$ of the first approximation inboard of the 0.7 radial station and within $\pm 0.1\%$ outboard, is also plotted in Figure 11. The assumed and computed radial inflow comparison was poorer yet, continuing the deteriorating trend that was also shown by the RBL 1 cases in Figure 10. The induced performance became less reasonable, too, with a power coefficient of 0.0357 and a figure of merit of 135%.

The corresponding second approximation to the x-variations of the induced velocity components was computed. At the 0.4 and 0.7 stations, the computed x-variations of u were in good agreement with the assumed values. At 0.9, the computed variation agreed well initially with that assumed but reached a higher asymptotic value. At 0.975, the x-variation of u also agreed well initially but then increased much more rapidly with x; see Figure 12. It is highly encouraging that a maximum did not appear, at least as far downstream as computations were made. This appears to indicate that the maxima and subsequent decreases are only temporary phenomena which may occur at particular steps toward a force-free solution due to local peculiarities in the trailing vortex sheet distortion. The peculiarity here again seems to be a result of the relative stretching of the sheets, which is considerably less than it was for the initial set of variations.

It is clear from the results presented for RBL 1 and RBL 2 that we have not yet obtained force-free solutions for these blade loadings. Nevertheless, the successful inflow

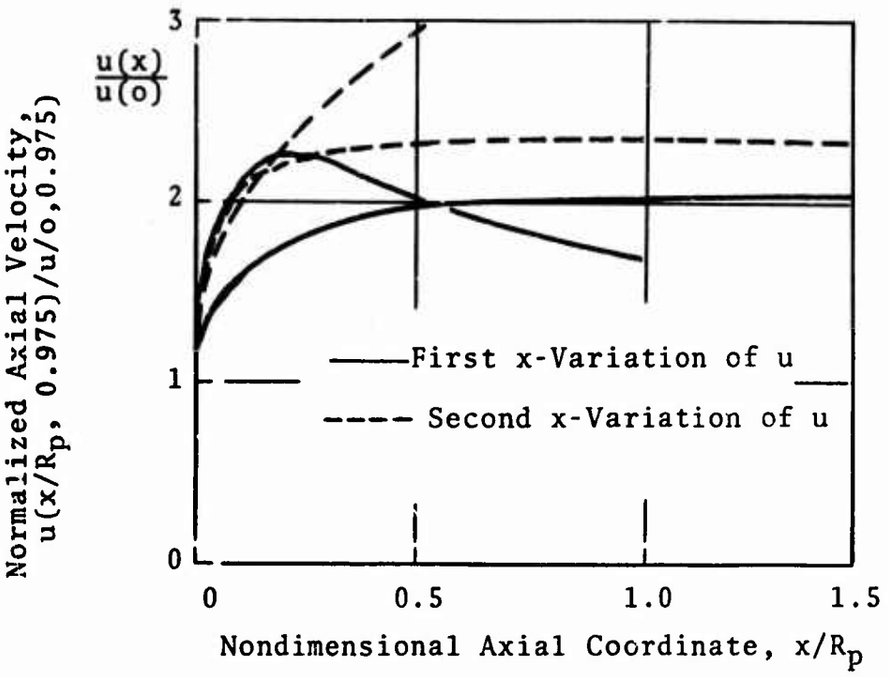

Figure 12. Comparison of Assumed and Computed x-Variation of Axial Induced Velocity Along Trajectory From r_o/R_p = 0.975, Representative Blade Loading Two, First and Second Variations.

iterations that we have achieved led us to return to the specific propeller designs so that comparisons could be made with test data wherever possible. Before these are reported, though, a number of useful observations can be made from the RBL results.

Observations for Representative Blade Loadings

We are presenting in this section certain observations based upon our computations for RBL 1 and RBL 2. However, it must be recognized that these loadings are indicative of thrust coefficients corresponding to the higher blade pitch settings of typical propeller designs. Thus, the applicability of these observations and the subsequent generalizations that we draw are unexplored for loadings at thrust coefficients more typical of lower pitch settings. Regardless, we offer them in the hope that they might provide aid in initiating computations for such cases.

The first area of observations concerns an approximate correlation that we have found for the axial inflow. With the blade circulation distribution Γ fixed, the singular part of the axial inflow is essentially fixed, too, because the coefficients of the singular parts in Eq. (24) are virtually independent of the inflow, as we have observed before (see p. 31 of Ref. 10). As an iteration proceeds, then, for a given set of x-variations of the axial velocity u, it is only the regular part of the axial inflow that differs from one approximation to the next. By consideration of each application of the Biot-Savart operator in Eq. (2), we found that the product of the input axial inflow at a representative radial station near the tip, 0.975 in particular, times the regular part of the output axial inflow at any radial station was relatively invariant throughout the iteration. In an approximate sense, this correlation can be explained by consideration of the Bio-Savart operator in Eq. (2) as broken into singular and regular parts. The correlation seems to imply that the regular part of the trailing axial influence function at any radial station is approximately a function of radius only divided by the input axial inflow at the 0.975 station, since multiplication of both sides of the equation by this quantity gives an integral which is essentially invariant from one approximation to the next. The validity of the inverse proportionality is suggested by the generalized actuator disk result (see Eq. 22 of Ref. 17), that the mean axial inflow at any radius is inversely proportional to the free-stream velocity, which determines the pitch of the trailing vortex sheets in that

case. In the present static case, the input axial inflow at 0.975 is a measure of the effective "pitch" of the trailing vortex sheets. Therefore, the correlation is a quantitative verification of our persistent observation that the effective "pitch" of the trailing vortex sheets near the tip controls the magnitude of the axial inflow at all radii.

The second area of observations concerns the inflow iterations for a specified Γ and set of x-variations of u. These iterative properties have emerged clearly from all the RBL 1 and RBL 2 computations. For both loadings, the zeroth approximations to the axial and tangential inflow based on Ref. 19 were adequate. Axial inflow convergence always began outboard and then continued to improve farther inboard with each successive approximation. This results from the general property that the velocity induced by a distorted helical vortex is much larger at radii smaller than itself than at radii larger than itself. The tangential inflow converged rapidly but is different outboard from $-N\Gamma/4\pi r$, as can be seen from Figures 9 and 11.

Axial inflow convergence proceeds very rapidly when the x-variations of u are changed. In particular, the axial inflow outboard of the 0.9 radial station changes only slightly (see Figures 9 and 11), although the inboard stations are affected greatly. This demonstrates again the insensitivity of the axial inflow to local changes in the x-variation but the profound sensitivity inboard to x-variation changes outboard.

On the basis of these observations, we can recommend a quick way to achieve axial inflow convergence for a fixed Γ. First, compute the Biot-Savart operators with the zeroth approximation as input. Use an axial iteration factor of 1.0 to determine the first approximation outboard of the 0.8 radial station. With the resulting axial inflow at 0.975, use the correlation outlined above to determine the axial inflow at the remaining radii. For all subsequent approximations, use axial iteration factors of 1.0 over the entire blade. Although the above procedure might minimize computer time, overall it might be just as efficient to use axial iteration factors of 1.0 over the entire blade for the first approximation as well as the subsequent ones. Moreover, when the x-variations of u are changed, axial iteration factors of 1.0 should be used because the axial inflow changes only slightly near the tip and so converges very quickly elsewhere.

The third area of observations concerns the iteration toward a satisfactory force-free approximation by means of changes in the x-variations of u. Both RBL 1 and RBL 2 have

similar properties in this regard. There seems to be a definite trend toward agreement between the assumed and computed variations immediately downstream of the lifting line. The results in Figure 12 are typical of this trend. Farther downstream, however, the computed x-variations of u may have features like the observed maxima, which can result even from small changes in the axial inflow. There is evidence, as in Figure 12, that these are only transient phenomena which disappear as we approach more closely a force-free wake.

Although the x-variations of u appeared to be slowly tending toward the force-free state, the computed radial inflow was simultaneously indicating poorer agreement with the assumed distribution given by the specified contraction pattern, as in Figure 10. It appeared that less contraction was necessary than that assumed. The performance was also becoming less realistic with improvement in the x-variations of u. At the end of our computations for RBL 1 and RBL 2, then, the problems involved in iterating to a truly force-free solution still had to be resolved.

CHAPTER 6

THEORETICAL RESULTS FOR SPECIFIC PROPELLERS

General

We returned to computations for specific propeller designs at this point after having achieved a good deal of experience through the treatment of the two representative blade loadings. In the present chapter, we shall discuss these theoretical results and shall make comparisons with test data whenever possible to aid in assessing the theoretical development.

The first two cases discussed in this chapter are examples of high pitch settings and high thrust coefficients. Consequently, they have blade circulation and inflow distributions which resemble the RBL most closely. These cases could be iterated successfully. After they had been brought to a reasonable degree of completion, including a change in the x-variations of u for one of them, we pursued calculations at lower pitch settings. Meaningful results were obtained for two of these, which are indicative of an important regime of static propeller operation.

At all times during these computations, we fed in our best previous experience, even if we had no assurance that a particular choice (say, of iteration factors, apparent correlations, etc) was a valid generalization of an earlier result. Also, although the cases are described basically in chronological order, some of them were carried out, at least in part, simultaneously.

120 AF Propeller, 17.0° Pitch Setting

The first case considered after the RBL was the 17.0° pitch setting, as measured at the 0.7 radial station, of the four-bladed, 7-foot-diameter, 120 Activity Factor (AF) propeller. The characteristics of this blade design are given in Appendix II. This design is simply a scaled-up version of the basic 65 AF blade, although it has a different blade twist distribution β. The airfoil section data appropriate to a tip speed of 700 feet per second and the zeroth approximation to the axial inflow and blade circulation distribution Γ were determined on the basis of Refs. 6 and 12 exactly as for the 65 AF propeller. The zeroth approximation to the tangential inflow was found as usual from Γ and the general-

ized actuator disk result of $-N\Gamma/4\pi r$. The x-variations downstream of the axial velocity u were chosen to be the same set that was used initially for RBL 1 and RBL 2.

Seven successive approximations to Γ and the inflow were computed to achieve convergence of the seventh approximation to the axial inflow to within $\pm 2.6\%$ of the sixth approximation. The axial iteration factors used differed from one approximation to the next as we tried to proceed quickly to convergence. The seventh approximations to Γ and the axial and tangential inflow are plotted in Figure 13 along with the zeroth approximations. The assumed and computed radial inflow compared favorably here, better than in any of the RBL cases. However, the predicted performance is too optimistic compared with the data acquired at this pitch setting in our test program; see Table III.

Next, the seventh approximation to the x-variations of the induced velocity components along the trailing vortex sheets was computed. At the 0.4 and 0.7 radial stations, the computed x-variations of u increase less rapidly than assumed, comparable to RBL 1 and RBL 2. At 0.9, the computed variation agrees closely with the assumed variation. At 0.975, the computed variation increases much more rapidly than assumed and has a maximum and subsequent decrease. The maximum is higher than for either RBL 1 or RBL 2. We modified the x-variations of u accordingly, but we ignored the decrease beyond the maximum at the 0.975 radial station.

Four successive approximations to Γ and the inflow were computed with these modified x-variations of u and with the previous sixth approximation as the zeroth. The axial inflow converged to within $\pm 1.8\%$ except at the 0.2 radial station, where blade stall apparently prevented convergence. Fewer approximations were necessary here because Γ and the axial inflow outboard did not change greatly; see Figure 13. The assumed and computed radial inflow comparison was appreciably less favorable than it had been initially, with indications that there should be less contraction, just as we had found for RBL 1 and RBL 2. Moreover, the performance predictions are in even poorer agreement with the test data; see Table III.

The corresponding fourth approximation to the x-variations of the induced velocity components was computed. At the 0.4 and 0.7 stations, the computed x-variations of u agree well with the assumed variations. At 0.9, the computed variation increases more rapidly with x than assumed but has a maximum and subsequent decrease. At 0.975, the

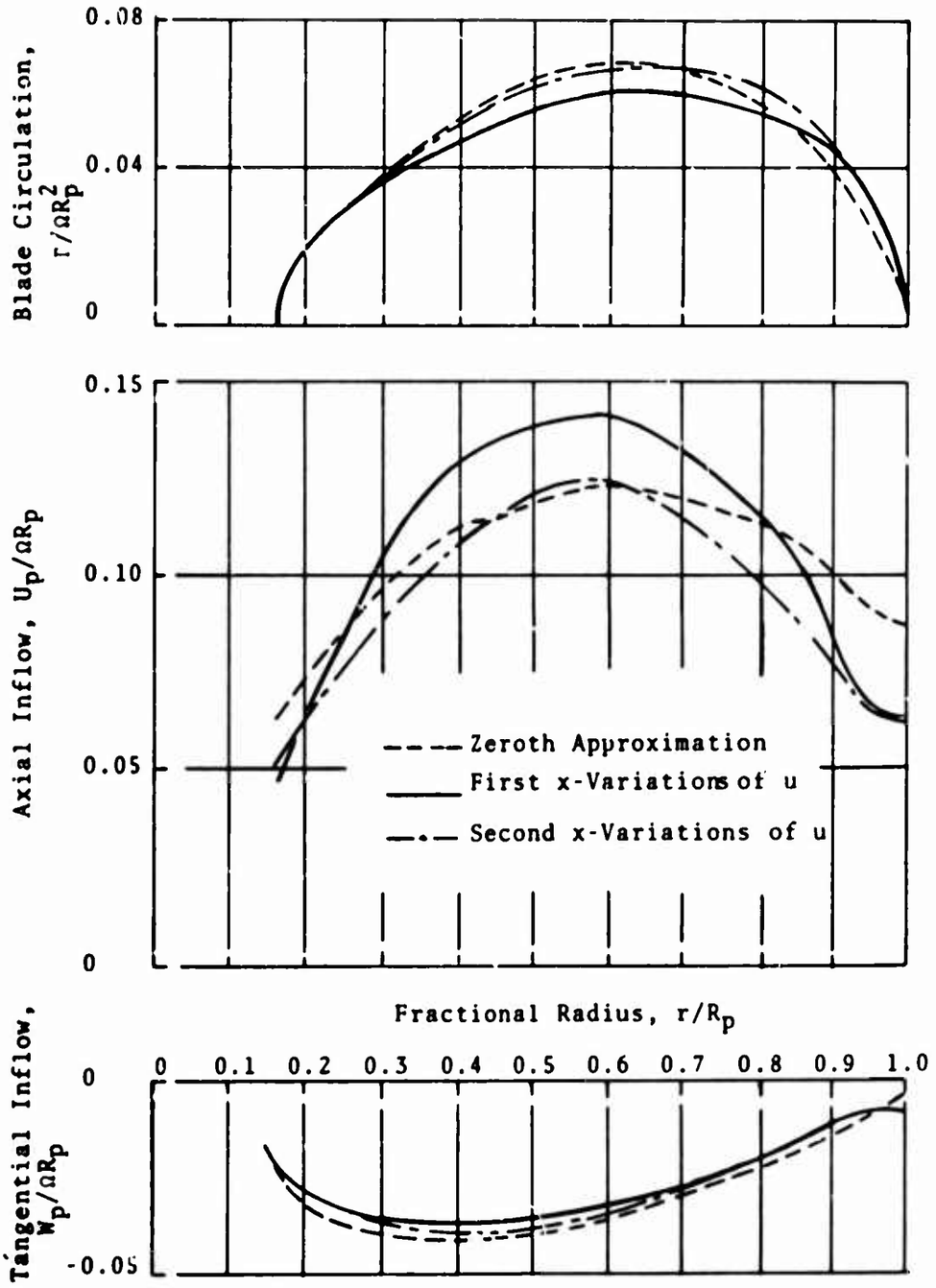

Figure 13. Blade Circulation and Axial and Tangential Inflow; 120 AF Propeller, $\beta 0.7R_p$ = 17.0°, First and Second Assumed x-Variations of Axial Velocity.

TABLE III

PERFORMANCE COMPARISONS

120 AF Propeller
$\beta 0.7R_p = 17.0°$

	C_T	C_P	F/M
Canadair Test	0.1800	0.0870	70%
First x-Variations of u	0.2138	0.1029	77%
Second x-Variations of u	0.2303	0.1096	80%

computed x-variation of u is initially less rapid but continues to increase without the appearance of a maximum like the one that occurred for the original assumed variation.

This concluded our computations for this case. The results and trends resemble RBL 1 and RBL 2 very closely, in that an apparent tendency toward the force-free state in the x-variations of u leads to a less favorable comparison of the predicted performance with test data as well as a greater discrepency between the assumed and computed radial inflow.

The technique that we developed for achieving convergence of the tangential inflow is worth mentioning at this point. It was used for all subsequent cases and is based upon the results for RBL 1 and RBL 2, that the computed tangential inflow differs by only a small amount from $-N\Gamma/4\pi r$. At each step of the iteration we determined for each radial station the ratio of the computed value to $-N\Gamma/4\pi r$. These ratios were then multiplied by the next approximation to $-N\Gamma/4\pi r$ to determine the corresponding approximation to the tangential inflow. This procedure led rapidly to convergence.

Finally, we should remark on the correlation of the regular part of the axial inflow that had been found for the RBL. Here it did not prove useful because there were large discrepancies among all the approximations, especially between the initial and final one. We attempted to generalize the correlation further to account for the changes in Γ from step to step as follows. A rough approximation to an average strength of the derivative of Γ can be found by dividing its maximum value by the radial distance between the maximum and the tip. This distance does not vary much during the iteration. Therefore, we tried to improve the correlation for each application of the Biot-Savart operator in Eq. (2) by dividing the regular part of the output axial inflow by the maximum of the input Γ as well as by multiplying it by the input axial inflow at the 0.975 radial station. Unfortunately, the results indicate almost equally large discrepancies among the iterations here, too. We did use both correlations as a guide later in the early stages of iteration when aid was needed most, but without much success.

3(109652) Propeller, 16.0° Pitch Setting

The next case considered was the 16.0° pitch setting, as measured at the 0.7 radial station, of the three-bladed, full-scale Curtiss-Wright 3(109652) propeller. The blade

design characteristics are given in Appendix II. Computations on the basis of the initial wake hypothesis had been made for this case previously; see Refs. 10 and 11. The airfoil sectional data appropriate to a tip speed of 785 feet per second and the zeroth approximations were determined as usual from Refs. 6 and 12 and the generalized actuator disk results. The same set of x-variations of the axial velocity u was selected that we had used initially for RBL 1, RBL 2, and the 17.0° setting of the 120 AF propeller.

Five successive approximations to Γ and the inflow were computed to achieve convergence of the axial inflow to within ±2.1%, except, as before, at the 0.2 radial station. To investigate this difficulty inboard, we increased the hub radius from 0.125 to 0.167 and computed two further approximations, which did not improve the situation. The seventh approximations to Γ and the axial and tangential inflow are presented in Table IV with the zeroth approximations and the initial wake hypothesis results for comparison. The assumed and computed radial inflows again indicate that there should be less contraction than we have specified. The performance is plotted in Figure 14 with the initial wake hypothesis and Curtiss-Wright test data (Ref. 10) for comparison. It should be noted that the hub radius change led to performance changes of less than ±1.0%.

The seventh approximation to the x-variations of the induced velocity components along the trailing vortex sheets was computed. The computed x-variations of u were qualitatively similar to those for the 17.0° setting of the 120 AF propeller for the comparable input variations. Maxima were observed at both the 0.9 and the 0.975 radial stations.

In view of the unsuccessful trend that we had found in the previous cases by modifying the x-variations of u, and because the indicated changes lead in the same direction here, we terminated computations for this case. Instead, we proceeded to cases with lower pitch settings.

65 AF Propeller, 12.6° Pitch Setting - Final Computations

We returned at this time to the case of the 65 AF propeller at a pitch setting of 12.6°, which we had considered originially; see Chapter 4. We resumed the computation where we had left off, using the x-variations of the axial velocity u that we had found to be most promising at that earlier time.

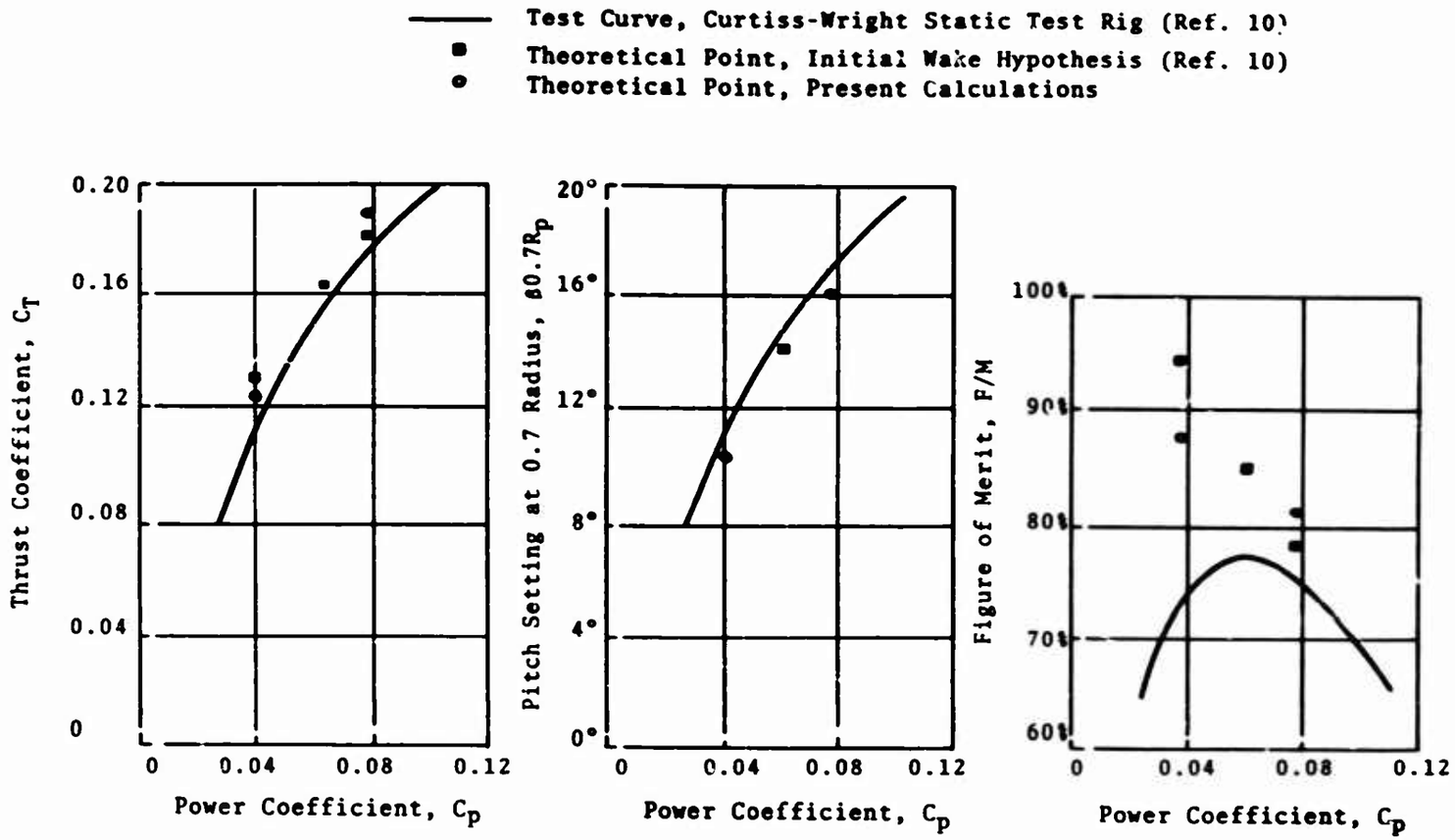

Figure 14. Comparison of Theoretical and Experimental Performance; 3(109652) Propeller, ΩR_p = 785 fps.

TABLE IV

BLADE CIRCULATION AND AXIAL AND TANGENTIAL INFLOW
3(109652) Propeller, $\beta 0.7R_p$ = 16.0°

r/R_p	$\Gamma/\Omega R_p^2$			$u/\Omega R_p$			$w/\Omega R_p$		
	0^{th}*	7^{th}**	IWH***	0^{th}	7^{th}	IWH	0^{th}	7^{th}	IWH
0.167	0	0	0	0.0390	0.0120	0.0100	-0.0080	-0.0070	-0.0100
0.200	0.0154	0.0144	0.0147	0.0486	0.0150	0.0131	-0.0184	-0.0170	-0.0128
0.300	0.0361	0.0342	0.0350	0.0745	0.0500	0.0504	-0.0288	-0.0280	-0.0210
0.400	0.0598	0.0574	0.0575	0.0957	0.0963	0.0948	-0.0339	-0.0339	-0.0350
0.500	0.0657	0.0645	0.0638	0.0975	0.0940	0.0986	-0.0314	-0.0308	-0.0294
0.600	0.0667	0.0668	0.0654	0.0976	0.0929	0.0985	-0.0265	-0.0250	-0.0244
0.700	0.0674	0.0681	0.0655	0.1005	0.0947	0.1038	-0.0230	-0.0212	-0.0214
0.800	0.0620	0.0651	0.0635	0.1011	0.0912	0.0960	-0.0185	-0.0164	-0.0168
0.900	0.0456	0.0506	0.0485	0.0970	0.0815	0.0877	-0.0121	-0.0121	-0.0126
0.950	0.0343	0.0386	0.0428	0.0958	0.0852	0.0744	-0.0086	-0.0117	-0.0101
0.975	0.0262	0.0280	0.0241	0.0972	0.0923	0.1018	-0.0064	-0.0119	-0.0113
1.000	0	0	0	0.0980	0.0960	0.1060	-0.0042	-0.0120	-0.0120

* 0^{th} - Zeroth Approximation
** 7^{th} - Seventh Approximation
*** IWH - Initial Wake Hypothesis (Ref. 10)

Ten successive approximations to Γ and the inflow were computed to achieve axial inflow convergence to within ±2.5% everywhere except at the 0.9 radial station, where it was 8.1% different. This large number of approximations was necessary because the axial inflow was very low outboard (less than one-half of previous cases), and the results were very sensitive to small changes. The tenth approximation to Γ and the axial and tangential inflow are presented in Table V along with the zeroth approximations and, for a further comparison, the Knight and Hefner values according to Ref. 19. The assumed and computed radial inflows do not compare favorably; see Figure 15. Contrasted with the previous cases, though, the indications here are that more contraction is needed outboard. The predicted performance is again much too optimistic compared with the data acquired at this pitch setting in our test program. In particular, the predicted and measured thrust coefficients are 0.1156 and 0.1200, respectively; power coefficients, 0.0377 and 0.0520, respectively; and figures of merit, 83% and 63%, respectively.

The tenth approximation to the x-variations of the induced velocity components along the trailing vortex sheets was computed. At the 0.4 and 0.7 radial stations, the computed x-variations of u increase slightly less rapidly, as has been the usual case. At the 0.9 station, however, the computed variation is in agreement initially but then falls below by a small amount, while at 0.975 the computed variation increases more rapidly initially but as a maximum that is about 30% lower than the assumed asymptotic value. We did not modify the x-variations of u and compute further, but extrapolations based on the previous cases show that there would be a distinct improvement in the agreement with performance test data if this were done.

At this stage of our investigation, we reexamined several choices of basic input parameters that had been selected much earlier. This was appropriate because by now we had achieved convergent inflow iterations in a number of cases.

First, we reduced the distance between the basic elements of the trailing vortex sheets from $\pi/6$ to $\pi/12$. The recomputed axial inflow in the tenth approximation differed by less than ±2.5% everywhere along the blade and was even closer near the tip. This is within what we considered to be convergence for this case. The recomputed performance parameters differed by less than ±1.0%. We concluded that our basic spacing was adequate.

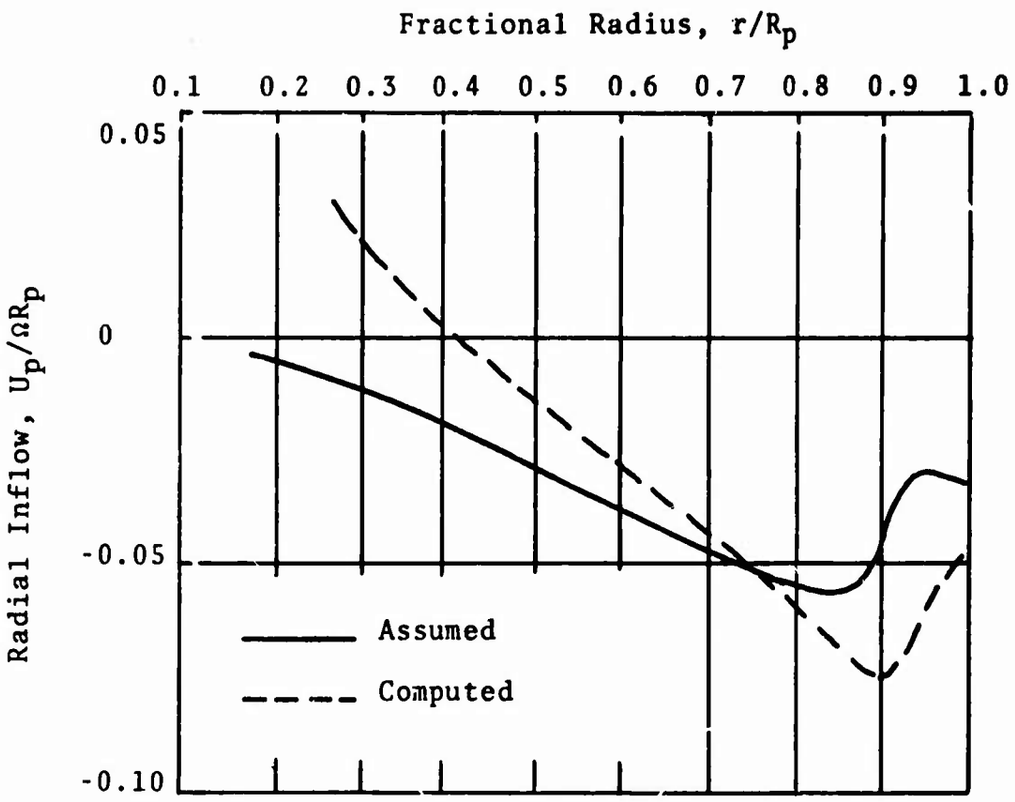

Figure 15. Comparison of Assumed and Computed Radial Inflow; 65 AF Propeller, $\beta 0.7R_p$ = 12.6°.

TABLE V

BLADE CIRCULATION AND AXIAL AND TANGENTIAL INFLOW
65 AF Propeller, $\beta_{0.7R_p} = 12.6°$

r/R_p	$\Gamma/\Omega R_p^2$			$u/\Omega R_p$			$w/\Omega R_p$		
	0th*	K & H**	10th***	0th	K & H	10th	0th	K & H	10th
0.167	0	0	0	0.0250	0.0500	0.0340	-0.0050	-0.0040	-0.0180
0.200	0.0065	0.0057	0.0054	0.0355	0.0580	0.0418	-0.0103	-0.0091	-0.0190
0.300	0.0192	0.0187	0.0185	0.0629	0.0773	0.0624	-0.0204	-0.0198	-0.0220
0.400	0.0270	0.0254	0.0252	0.0723	0.0900	0.0791	-0.0215	-0.0202	-0.0200
0.500	0.0321	0.0294	0.0291	0.0773	0.0968	0.0894	-0.0204	-0.0187	-0.0193
0.600	0.0353	0.0320	0.0321	0.0817	0.1009	0.0933	-0.0187	-0.0170	-0.0173
0.700	0.0340	0.0304	0.0316	0.0787	0.0984	0.0887	-0.0154	-0.0138	-0.0142
0.800	0.0298	0.0261	0.0286	0.0736	0.0911	0.0781	-0.0119	-0.0104	-0.0110
0.900	0.0195	0.0172	0.0226	0.0626	0.0740	0.0465	-0.0069	-0.0061	-0.0066
0.950	0.0129	0.0106	0.0177	0.0546	0.0581	0.0273	-0.0043	-0.0036	-0.0036
0.975	0.0092	0.0088	0.0127	0.0493	0.529	0.0272	-0.0030	-0.0029	-0.0028
1.000	0	0	0	0.0420	0.0505	0.0271	-0.0020	-0.0020	-0.0020

* 0th - Zeroth Approximation
** K & H - Knight and Hefner Approximation (Ref. 19)
*** 10th - Tenth Approximation

Next, we increased the number of Glauert coefficients in the least-squares fit of the blade circulation distribution Γ from 10 to 15, while retaining the same 20 input values. This reduced the maximum difference between input values and the fit from $\pm 0.5\%$ to $\pm 0.2\%$. However, there was a noticeable introduction of "wiggles" into the derivative of Γ and thus in the singular part of the axial inflow. These "wiggles" arise from the amplification effects of the higher order Glauert coefficients that we discussed in Chapter 2. The resultant changes in the tenth approximation to the axial inflow are less than $\pm 2.2\%$ inboard of the 0.85 radial station but are -5.6%, +12.5%, and -12.0% at the 0.9, 0.95, and 0.975 radial stations, respectively. The performance parameters changed by less than 0.3%. We feel, then, that the increases at some radii are balanced by decreases at others, and therefore the "wiggles" are indeed extraneous. We concluded that 10 coefficients had been a wise choice but that further research on the best method of fitting Γ is desirable.

Finally, we permitted the trailing vortex sheet elements to deform immediately behind the lifting line instead of after two undeformed initial steps. Although the influence functions are nonintegrable in a rigorous sense, as we have pointed out in Chapter 2, the numerical integration proceeds smoothly nevertheless. The differences in the tenth approximation to the axial inflow were less than $\pm 2.9\%$ except at 0.975, where it was +4.7%. These are larger differences than we have generally accepted for convergence, although the performance parameters differ by less than $\pm 1.0\%$. We concluded that the axial inflow is sufficiently sensitive to the amount of initial distortion of the trailing vortex elements that an improved criterion, based on physical considerations, should be investigated.

This concluded computations for this case. With the success achieved at this relatively low pitch setting, we turned to two further examples in the hope of generalizing the results obtained here.

120 AF Propeller, 10.0° Pitch Setting

The next case is the 10.0° pitch setting, as measured at the 0.7 radial station, of the 120 AF propeller operating at a tip speed of 700 feet per second. The instantaneous velocity components in the propeller wake had been measured for this case in the experimental portion of this investigation in the same manner as for the 8.2° pitch setting of

the 65 AF propeller. The azimuthal variations of the axial and radial velocity components in the wake are presented in Appendix III, while full details of the experimental investigation are contained in Ref. 14.

The zeroth approximations to the blade circulation Γ and the axial and tangential inflows were determined as usual. The x-variations of the axial velocity u inboard of the 0.8 radial station were chosen from a consensus of all the earlier computations, while outboard of 0.8 they were chosen to be identical to those for the 12.6° pitch setting of the 65 AF propeller because it was the most closely similar case that we have treated.

A first approximation to the inflow was computed. The axial inflow was considerably higher than the input over midblade but was strongly negative outboard of the 0.93 radial station. These results are almost identical to those described in Chapter 4 for the 8.2° setting of the 65 AF propeller. In that case we had changed the x-variations of u outboard without achieving local improvement in the axial inflow, a result which was borne out later when we showed that changes in the x-variations of u outboard do not change the axial inflow significantly outboard (see Figures 9, 11, and 13). Accordingly, we retained the same x-variations of u here, but we chose a first approximation to the axial inflow that was qualitatively similar to our earlier converged results. Unfortunately, the second approximation was even more strongly negative and showed even less change of achieving inflow convergence.

The wake data were again limited in their usefulness in exactly the same way that they were for the 65 AF propeller at 8.2°; see Chapter 4. The extent and growth downstream of the nonrepeatable region are presented in Figure 8.

Therefore, this case as well as the earlier one could not be iterated further with our present knowledge. A good deal of further research, both experimental and theoretical, is required to understand the nature of the flow phenomena in the vicinity of the propeller tip, especially in cases such as these.

3(109652) Propeller, 10.0° Pitch Setting

The final case considered is the 10.0° pitch setting, as measured at the 0.7 radial station, of the 3(109652) propeller operating at a tip speed of 785 feet per second.

This case had been treated in our earlier studies based upon the initial wake hypothesis, and a single approximation had also been calculated with the refined wake hypothesis. The zeroth approximations to Γ and the axial and tangential inflows were found as usual, while the same set of x-variations of u was selected that we had tried at the 10.0° pitch setting of the 120 AF propeller.

Eight successive approximations to Γ and the inflow were computed. The axial inflow converged inboard to within $\pm$2.0%, although outboard the differences were as large as $\pm$6.1% despite the absolute differences being of the same size. The axial inflow near the tip is the lowest of any case we have computed. Again, convergence could not be achieved at the 0.2 radial station. The eighth approximations to Γ and the axial and tangential inflows are presented in Table VI along with the zeroth approximations and the initial wake hypothesis results. The assumed and computed radial inflows do not compare well, and the indications are that more contraction is required outboard, as was shown in Figure 15 for the 65 AF propeller at 12.6°. This is in marked contrast to the 16.0° setting of this same 3(109652) propeller. The predicted performance is again too optimistic compared to test data; see Figure 14.

The eighth approximation to the x-variations of the induced velocity components along the trailing vortex sheets was computed. At the 0.4 and 0.7 radial stations, the computed x-variations of u lie slightly below the assumed values. At the 0.9 station, the computed variation increases more rapidly, has a maximum which is larger than the assumed asymptotic value, and then decreases. At 0.975, the computed variation increases initially at the assumed rate but has a maximum that is less than one-half as large as the assumed asymptote. Qualitatively, the indications for this case are the same as for the 65 AF propeller at 12.6°; namely, that lower asymptotic values of the x-variations of u are needed outboard. Extrapolations based on such modified variations should give performance predictions that are in better agreement with the test data. These extrapolations have not been verified.

Observations for Specific Propellers

The additional complications of the blade circulation Γ changing from one approximation to the next, as well as the geometrical differences in blade design from one propeller to another, limit our observations and generalizations

TABLE VI

BLADE CIRCULATION AND AXIAL AND TANGENTIAL INFLOW
3(1096-2) Propeller, $\beta_{0.7R_p} = 10.0°$

r/R_p	$\Gamma/\Omega R_p^2$			$u/\Omega R_p$			$w/\Omega R_p$		
	0th*	8th**	IWH***	0th	8th	IWH	0th	8th	IWH
0.167	0	0	0	0.0395	0.0300	0.0120	-0.0155	-0.0200	-0.0120
0.200	0.0157	0.0148	0.0148	0.0491	0.0385	0.0220	-0.0187	-0.0230	-0.0147
0.300	0.0342	0.0327	0.0345	0.0722	0.0751	0.0608	-0.0272	-0.0264	-0.0236
0.400	0.0499	0.0425	0.0464	0.0857	0.1040	0.0914	-0.0298	-0.0261	-0.0274
0.500	0.0538	0.0465	0.0491	0.0863	0.1039	0.0959	-0.0257	-0.0226	-0.0228
0.600	0.0517	0.0454	0.0482	0.0836	0.0999	0.0922	-0.0206	-0.0185	-0.0179
0.700	0.0491	0.0438	0.0438	0.0823	0.0940	0.0941	-0.0168	-0.0145	-0.0150
0.800	0.0388	0.0368	0.0420	0.0750	0.0789	0.0678	-0.0116	-0.0103	-0.0096
0.900	0.0243	0.0289	0.0286	0.0642	0.0502	0.0511	-0.0065	-0.0056	-0.0054
0.950	0.0131	0.0199	0.0250	0.0488	0.0326	0.0207	-0.0033	-0.0027	-0.0022
0.975	0.0080	0.0142	0.0200	0.0391	0.0241	0.0104	-0.0020	-0.0018	-0.0011
1.000	0	0	0	0.0275	0.0200	0.0080	-0.0010	-0.0015	-0.0005

* 0^{th} - Zeroth Approximation
** 8^{th} - Eighth Approximation
*** IWH - Initial Wake Hypothesis (Ref. 10)

to a greater extent than for the representative blade loadings. Moreover, we have already made observations about our attempt to generalize the correlation of the regular part in the section for the 120 AF, 17.0° pitch setting case.

The first area of observations concerns the inflow iterations for a given set of x-variations of u. Unfortunately, the iterative properties for the axial inflow have not emerged clearly. The sensitivity that we discussed earlier regarding the fit of Γ contributes to the difficulty. For instance, the convergence did begin outboard generally and proceeded inboard. However, this trend is not as decisive as for the representative blade loadings because Γ changed as well, and so the changes in the axial inflow outboard from step to step were larger than the corresponding changes for a fixed Γ. Nevertheless, the changes were definitely smaller outboard than inboard. Also, it was much more difficult to get the axial inflow outboard even to settle down enough to continue the iteration; we could not, in fact, for the two cases for which we obtained measured wake data. We are unable to recommend precise values for the axial iteration factors, but we found that values between 0.5 and 1.0 were best inboard of the 0.85 radial station and that values between 0.25 and 0.5 were best outboard of 0.85. A successful technique for iterating the tangential inflow has been discussed in the section for the 120 AF propeller at the 17.0° pitch setting.

In several cases, a convergent axial inflow could not be achieved at the 0.2 radial station, due in part to the blade section's being beyond the angle of attack of normal stall. In view of the small effect that the inboard region has on the performance, as witnessed by the small performance change with the hub radius modification for the 3(109652) propeller at the 16.0° pitch setting, it would be sensible just to fix the hub radius consistently at the 0.2 station in all cases.

The second area of observations concerns the iteration toward a satisfactory force-free approximation by means of changes in the x-variations of u. The single case that we did iterate in this fashion behaved identically to RBL 1 and RBL 2; namely, the x-variations of u seemed to be approaching the force-free state, but the computed radial inflow indicated even more strongly that less contraction was needed than had been assumed. Furthermore, the agreement between performance predictions and test data became worse. This case had a thrust coefficient higher than both RBLs. Unfortunately, no changes were made in the x-variations

of u after the first inflow iteration for the two lower pitch-setting, lower thrust-coefficient cases. For these, however, the computed radial inflow indicated that more contraction was needed than had been assumed. It is clear, then, that several problems must be resolved before a sufficiently good approximation to the performance can be achieved.

CONCLUSIONS

Based on the results obtained in this study, we draw the following principal conclusions.

Instantaneous wake velocity data that were repeatable with each blade passage could be obtained only over the middle part of the blade for the 65 AF propeller at the 8.2° pitch setting and for the 120 AF propeller at the 10.0° setting. Near the hub and especially near the tip, the data were random and could not be resolved meaningfully into components. Theoretical computations for these two cases, which are low pitch settings, could not be iterated successfully. Lack of data near the tip prevented guidance of the computations, and lack of convergence prevented checking with the good data.

The refined wake hypothesis was found to be inadequate, in general, as an approximation to the force-free condition of the wake on the basis of poor agreement of performance predictions with test data and an excessive amount of contraction. Accordingly, a new wake representation was formulated which fixed the overall contraction pattern and permitted concentration on the effective "pitch" of the trailing vortex sheets.

A series of computations for thrust coefficients above 0.15 (namely, two representative blade loadings and two propellers, each at one setting) showed that the assumed and computed "pitch" came into closer agreement (i.e., more nearly force free) through changes in the variations of the axial velocity with distance downstream along the trailing vortex sheets. Simultaneously, though, the fixed contraction became progressively too great near the tip, and the performance predictions became too optimistic compared to test data.

A series of computations for thrust coefficients below 0.13 (namely, two propellers, each at one setting) was made without changing the variations of the axial velocity. The fixed contraction for these cases was too small near the tip, but the performance predictions were still too optimistic.

Practical use as a design tool of solutions for specific blade circulation distributions, such as the representative blade loadings, is premature without better theoretical and experimental correlation. However, the representative loadings offer great computational simplifications that can be utilized in future theoretical developments.

LITERATURE CITED

1. Abramowitz, M., and Stegun, I. A., Editors, Handbook of Mathematical Functions With Formulas, Graphs and Mathematical Tables, National Bureau of Standards, Applied Mathematics Series 55, Washington, D. C., 1964.

2. Borst, H. V., and Glover, L. S., Application of Theodorsen's Theory to Strip Analysis Procedure for Single Rotation Propellers, Report No. C-2070, Curtiss-Wright Corp., Propeller Div., Caldwell, N. J., September 2, 1949.

3. Byrd, P. F., and Friedman, M. D., Handbook of Elliptic Integrals for Engineers and Physicists, Springer-Verlag, Berlin, Germany, 1954.

4. Denny, S. B., Comparisons of Experimentally Determined and Theoretically Predicted Pressures in the Vicinity of a Marine Propeller, Naval Ship Research and Development Center, Report 2349, May 1967.

5. Durand, W. F., Editor, Aerodynamic Theory, Vol. II, Dover Publications, Inc., New York, New York, 1963.

6. Enos, L. H., and Borst, H. V., Propeller Performance Analysis Aerodynamic Characterists, NACA 16 Series Airfoils, Report No. C-2000, Curtiss-Wright Corp., Propeller Div., Caldwell, N. J., December 2, 1948.

7. Erickson, J. C., Jr., and Ordway, D. E., A New Approach to the Static Thrust Problem, Phase II, Calculation of Thrust and Torque, Model X-100 Propeller, $\beta_{0.7R_p} = 10.0°$, TAR-TR 632, THERM, Incorporated, May 1963.

8. Erickson, J. C., Jr., and Ordway, D. E., A New Approach to the Static Thrust Problem, Phase III, Further Inflow Calculations with Extensions to Partially Negative Γ Distributions, TAR-TR 635, THERM, Incorporated, August 1963.

9. Erickson, J. C., Jr., and Ordway, D. E., A New Approach to the Static Thrust Problem, Phase IV, Further Development of Performance Calculation Method, TAR-TR 638, THERM, Incorporated, December 1963.

10. Erickson, J. C., Jr., Ladden, R. M., Borst, H. V., and Ordway, D. E., A Theory for VTOL Propeller Operation in a Static Condition, Technical Report 65-69, U.S. Army Aviation Materiel Laboratories, Fort Eustis, Virginia, October 1965, AD 623527.

11. Erickson, J. C., Jr., and Ordway, D. E., "A Theory for Static Propeller Performance", Proceedings, CAL/USAAVLABS Symposium, Aerodynamic Problems Associated with V/STOL Aircraft, Vol. I, Propeller and Rotor Aerodynamics, 22-24 June 1966.

12. Foss, R. L., Strip Analysis Method for Evaluating Static Thrust, Report No. C-2402, Curtiss-Wright Corp., Propeller Div., Caldwell, N. J., November 19, 1952.

13. Gail, A., Letter to the Editor, Journal of the Aeronautical Sciences, Volume 10, Number 8, October 1943, p. 320.

14. Gilmore, D. C., and Gartshore, I. S., Measurements of the Instantaneous Velocities in the Wake of Two Propellers Operating at Zero Advance Ratio, Department of Mechnaical Engineering, McGill University, Final Report Submitted to Therm Advanced Research, Inc., January 11, 1967.

15. Glauert, H., The Elements of Aerofoil and Airscrew Theory, Second Edition, Cambridge University Press, Cambridge, England, 1948.

16. Greenberg, M. D., and Kaskel, A. L., Inviscid Flow Field Induced by a Rotor in Ground Effect, NASA, CR-1027, May 1968.

17. Hough, G. R., and Ordway, D. E., The Generalized Actuator Disk, TAR-TR 6401, Therm Advanced Research, Inc., January 1964; also "The Generalized Actuator Disk", Developments in Theoretical and Applied Mechanics, Volume II, Proceedings of the Second Southeastern Conference on Theoretical and Applied Mechanics, Pergamon Press, Oxford, England, 1965, pp. 317-336.

18. Kerwin, J. E., and Leopold, R., "A Design Theory for Subcavitating Propellers", Transactions of the Society of Naval Architects and Marine Engineers, Volume 72, 1964, pp. 294-335.

19. Knight, M., and Hefner, R. A., Static Thrust Analysis of the Lifting Airscrew, NACA TN No. 626, December 1937.

20. Lin, C. C., Letter to the Editor, Journal of the Aeronautical Sciences, Volume 11, Number 3, July 1944, pp. 195-196.

21. von Mises, R., Theory of Flight, Dover Publications, Inc., New York, New York, 1959.

22. Morgan, W. B., Propeller Induction Factors, David Taylor Model Basin (now NSRDC), Report 1183, November 1957.

23. Ordway, D. E., Sluyter, M. M., and Sonnerup, B. U. O., Three-Dimensional Theory of Ducted Propellers, TAR-TR 602, THERM, Incorporated, August 1960.

24. Ordway, D. E., and Greenberg, M. D., General Harmonic Solutions for the Ducted Propeller, TAR-TR 613, THERM, Incorporated, August 1961.

25. Ordway, D. E., and Erickson, J. C., Jr., A New Approach to the Static Thrust Problem, Phase I, Formulation and Preliminary Assessment of Mathematical Model, TAR-TR 631, THERM, Incorporated, March 1963.

26. Scarborough, J. B., Numerical Mathematical Analysis, The Johns Hopkins Press, Baltimore, Maryland, 1930.

27. Sears, W. R., Theoretical Aerodynamics, Part 1: Introduction to Theoretical Hydrodynamics, 1957 Edition, Published by Author, Ithaca, New York, 1957.

28. Theilheimer, F., Letter to the Editor, Journal of the Aeronautical Sciences, Volume 10, Number 8, October 1943, pp. 320-321.

29. Theodorsen, T., Theory of Propellers, McGraw-Hill, New York, New York, 1948.

30. Tibery, C. L., and Wrench, J. W., Jr., Tables of the Goldstein Factor, David Taylor Model Basin (now NSRDC), Report 1534, December 1964.

31. Weissinger, J., The Lift Distribution of Swept-Back Wings, NACA, TM No. 1120, March 1947.

APPENDIX I

OPERATING INSTRUCTIONS FOR COMPUTER PROGRAMS

General

Brief operating instructions are presented to outline the use of the computer programs for the inflow velocity components (INFLOWPT), for the induced velocity components along the trailing vortex sheets (SHEETPT), for the propeller blade circulation and performance (PROPERFM), and for the vortex element trajectories and associated influence functions (MRCHINFO). These instructions consist of descriptions of the input data required, the punch format, and the print-out. All angles are in degrees, and the remaining data, unless noted otherwise, must be nondimensionalized with respect to the characteristic time $1/\Omega$ and the characteristic length R_p.

Program INFLOWPT

It is assumed that the following basic data are known; namely, distributions of the blade circulation and inflow as well as the variations with axial distance downstream of the induced velocity components along the trailing vortex sheets.

Specify the number of propeller blades (NB), the propeller hub radius (RH), the total number of points at which the inflow is desired (NI), and the radial coordinates (RI) of these inflow points. NI cannot exceed 40.

Specify the number of Glauert coefficients (NC) and the input values of the blade circulation (G) at each of the total number (NG) of Glauert variable locations (PG). NC and NG cannot exceed 25 and 100, respectively.

Specify the normalized variations along the trajectories of the axial (UW) and tangential (WW) velocity components at a total number (JW) of radial stations (RW) for each of a total number (IW) of axial stations (XW). Specify the ratio of radial-to-axial velocity (VW) along the trajectories for the same stations. Specify the magnitudes of the free-stream velocity (UFS) and the axial (UFAC) and tangential (WFAC) inflow components for the same JW radial stations. IW and JW cannot exceed 30 each. In the present form of the program, VFAC is not used, but zeroes must be read in.

Specify the number of steps (NSTEPSTR) and the associated step size of the time increment (STEPSTRT) for the initial undeformed march from the blade. For the remainder of the march, specify the number of steps (NSTEP) at each of the total number (NINCSIZE) of marching step time increment sizes (STEP). NINCSIZE cannot exceed 10. Specify the axial location (XCUTOFF) at which the march is terminated; this location must coincide with XW(IW). Specify the absolute value of accuracy (ERR) required in computing the Heuman lambda function (0.0001 was used). Specify the parameter (NE) that determines the fraction of π, i.e., π/NE, between the basic trailing vortex elements.

Specify the absolute value of accuracy (ACC) required in the Gaussian integration scheme and the maximum number of subdivisions (NLIMIT) permitted before termination.

Specify, finally, the month (IM), day (ID), and year (IY) of the run, the run number (NUMRUN), and a title for the run (TITLE). TITLE cannot exceed 80 alphanumeric characters.

The punch format for program INFLOWPT is given in Table VII and includes the input quantities and the field specification.

The print-out of INFLOWPT consists of the following: a title page; the axial, radial, and tangential velocity components of the stored input; identification of the automatically selected elements of the trailing vortex sheets; the Glauert coefficients and the fit of the blade circulation and its derivative with respect to the Glauert variable; and the strengths of the Cauchy and logarithmic singularities as defined in Eqs. (24) through (26). For each trailing element the following are printed out at all inflow points: the contributions to the total influence functions from the deformed portion of the trajectory; the total influence functions; and the regular parts of the total influence functions. For each inflow point there is printed out the regular part of the total influence functions from all trailing elements contributing to that point. The final results consist of the following print-out: the contribution to the inflow components from the regular part of the integrand; the contribution from the Cauchy singular part; the contribution from the logarithmically singular part; the total singular contribution; and the total inflow components.

TABLE VII

INPUT PUNCH FORMAT - PROGRAM INFLOWPT

Input Quantity	Field Spec.
IM, ID, IY	16I5
NUMRUN	16I5
TITLE(1) - TITLE(10)	10A8
NB, NE, NI, NG, NC, NINCSIZE	16I5
NLIMIT, IW, JW	16I5
RH, XCUTOFF	10F8.5
ACC, ERR	10F8.5
XW(1) - XW(IW)	10F8.5
RW(1) - RW(JW)	10F8.5
UW(1,1) - UW(IW,1) . . . UW(1,JW) - UW(IW,JW)	10F8.5
VW(1,1) - VW(IW,1) . . . VW(1,JW) - VW(IW,JW)	10F8.5
WW(1,1) - WW(IW,1) . . . WW(1,JW) - WW(IW,JW)	10F8.5

TABLE VII-contd.

UFS(1) - UFS(JW)	10F8.5
UFAC(1) - UFAC(JW)	10F8.5
VFAC(1) - VFAC(JW)	10F8.5
WFAC(1) - WFAC(JW)	10F8.5
RI(1) - RI(NI)	10F8.5
PG(1) - PG(NG)	10F8.5
G(1) - G(NG)	10F8.5
NSTEPSTR, STEPSTRT	I5,F8.5
NSTEP(1) - NSTEP(NINCSIZE)	16I5
STEP(1) - STEP(NINCSIZE)	10F8.5

Program SHEETPT

The same basic data are required as for INFLOWPT.

Specify the number of propeller blades (NB), the propeller hub radius (RH), the number of axial positions downstream (NXF) at which the sheet velocities are to be computed and their locations (XF), the number of trajectories (NRB) along which the sheet velocities are to be computed and their radial coordinates at the blade (RB), and the number of added auxiliary trajectories (NRA) adjacent to the sheet velocity trajectories and their radial coordinates at the blade (RA). NXF, NRB, and NRA cannot exceed 10, 20, and 40, respectively.

Specify the number of Glauert coefficients (NC) and the input values of the blade circulation (G) at each of the total number (NG) of Glauert variable locations (PG). Neither NC nor NG can exceed 100.

Specify the normalized variations along the trajectories of the axial (UW) and tangential (WW) velocity components at a total number (JW) of radial stations (RW) for each of a total number (IW) of axial stations (XW). Specify the ratio of radial-to-axial velocity (VW) along the trajectories for the same stations. Specify the magnitudes of the free-stream velocity (UFS), and the axial (UFAC) and tangential (WFAC) inflow components for the same JW radial stations. IW and JW cannot exceed 30 each. In the present form of the program, VFAC is not used, but zeroes must be read in.

Specify the number of steps (NSTEPSTR) and the associated step size of the time increment (STEPSTRT) for the initial undeformed march from the blade. For the remainder of the march up to XF(1) and for the march after each XF, specify the number of steps (NSTEP) at each of the total number (NINCSIZE) of marching step time increment sizes (STEP). NINCSIZE cannot exceed 10. Specify the marching step time increment size (STEPT) that is used within an axial interval (DELTAX) on either side of each XF. Specify the axial location (XCUTOFF) at which the march is terminated; this location must coincide with XW(IW). Specify the absolute value of accuracy (ERR) required in computing the Heuman lambda function (0.0001 was used). Specify the parameter (NE) that determines the fraction of π, i.e., π/NE, between the basic trailing vortex elements.

Specify the absolute value of accuracy (ACC) required in the Gaussian integration scheme and the maximum number of subdivisions (NLIMIT) permitted before termination.

Use the following values: for (RLIMT), 0.987; for (RVDNA), 0.025; for (RVDNB), 1.950; for (RVUPA), 2.050; for (RVUPB), 2.040; and for (RVUPC), 2.026.

Specify, finally, the month (IM), day (ID, and year (IY) of the run, the run number (NUMRUN), and a title for the run (TITLE). TITLE cannot exceed 80 alphanumeric characters.

The punch format for program SHEETPT is given in Table VIII and includes the input quantities and the field specification.

The print-out of SHEETPT consists of the following: a title page; the axial, radial, and tangential velocity components of the stored input; identification of the automatically selected elements of the trailing vortex sheets; the Glauert coefficients and the fit of the blade circulation and its derivative with respect to the Glauert variable; identification of the coordinates of the auxiliary points along the trailing vortex sheets that are used in determining γ and the derivative of S; identification of the coordinates of the sheet points; and the strengths of the Cauchy and logarithmic singularities as defined in Table II along with γ and the derivative of S. For each trailing element the following are printed out at all sheet points: the contributions to the total influence functions from the deformed portion of the trajectory; the total influence functions; and the regular parts of the total influence functions. For each sheet point there is printed out the regular part of the total influence functions from all trailing elements contributing to that point. The final results consist of the following print-out: the contribution to the sheet velocity components from the regular part of the trailing vortex integrand; the contribution from the Cauchy singular part; the contribution from the logarithmically singular part; the total singular contribution; the total trailing vortex sheet contribution (i.e., the sum of the regular and singular contributions); the contribution from the bound blade vortices; and the total induced velocity components at the sheet points.

TABLE VIII

INPUT PUNCH FORMAT - PROGRAM SHEETPT

Input Quantity	Field Spec.
IM, ID, IY	16I5
NUMRUN	16I5
TITLE (1) - TITLE (10)	10A8
NB, NE, NRB, NRA, NXF, NG, NC	16I5
NLIMIT, IW, JW	16I5
RH, XCUTOFF, DELTAX, STEPT	10F8.5
ACC, ERR	10F8.5
XW(1) - XW(IW)	10F8.5
RW(1) - RW(JW)	10F8.5
UW(1,1) - UW(IW, 1) . . . UW(1,JW) - UW(IW,JW)	10F8.5
VW(1,1) - VW(IW,1) . . . VW(1,JW) - VW(IW,JW)	10F8.5
WW(1,1) - WW(IW,1) . . . WW(1,JW) - WW(IW,JW)	10F8.5

TABLE VIII-contd.

UFS(1) - UFS(JW)	10F8.5
UFAC(1) - UFAC(JW)	10F8.5
VFAC(1) - VFAC(JW)	10F8.5
WFAC(1) - WFAC(JW)	10F8.5
RB(1) - RB(NRB)	10F8.5
RA(1) - RA(NRA)	10F8.5
XF(1) - XF(NXF)	10F8.5
PG(1) - PG(NG)	10F8.5
G(1) - G(NG)	10F8.5
NSTEPSTR, STEPSTRT	I5,F8.5
NINCSIZE(1)	16I5
NSTEP(1,1) - NSTEP(1,NINCSIZE(1))	16I5
STEP(1,1) - STEP(1,NINCSIZE(1))	10F8.5
.	
.	
.	
NINCSIZE(NXF+1)	16I5
NSTEP(NXF+1,1) - NSTEP(NXF+1,NINCSIZE(NXF+1))	16I5
STEP(NXF+1,1) - STEP(NXF+1,NINCSIZE(NXF+1))	10F8.5
RLIMT, RVDNA, RVDNB, RVUPA, RVUPB, RVUPC	10F8.5

Program PROPERFM

It is assumed that the following basic data are known; namely, the geometrical characteristics of the propeller, the sectional lift and drag data, and the inflow.

Specify the number of propeller blades (NB), the hub radius (RHB), the tip radius in feet (RP), and the tip speed in feet per second (PTS).

Specify at each of the total number (NRB) of radial stations (RB) the blade chord in feet (B); the Mach number (MN); the Reynolds number times ten to the minus sixth power (REN); a quantity (ICDCURVE) that is 1 if the drag coefficient (YCD) at that RB is given as a function of angle of attack (XAL) and is 2 if YCD is given as a function of lift coefficient (XCL) ; a quantity (CDZ) which is the drag coefficient for a 20° angle of attack at that RB if ICDCURVE = 1 or is the drag coefficient for an 8° angle of attack if ICDCURVE = 2. NRB cannot exceed 15.

Specify the total number of points (NXAL) at which XAL is given and the total number of points (NXCL) at which XCL is given. Specify for each RB the lift coefficient (YCL) at each value of XAL, and specify YCD at each value of XAL if ICDCURVE = 1 or at each value of XCL if ICDCURVE = 2. Specify a factor (CDFAC) to multiply the drag coefficient, if desired; usually 1.0 was taken. Neither NXAL nor NXCL can exceed 60.

Specify for each RB the free-stream velocity (CUB), the axial (SUB) and tangential (SWB) inflow, and the blade pitch angle (BETA).

Specify, finally, the month (IM), day (ID), and year (IY) of the run, the run number (NUMRUN) and case (NUMCASE), and a title for the case (PROPID). PROPID cannot exceed 80 alphanumeric characters.

The punch format for program PROPERFM is given in Table IX and includes the input quantities and the field specification. Note that the YCD input is given for ICDCURVE = 1; if ICDCURVE = 2, the upper limit would be NXCL rather than NXAL.

The print-out of PROPERFM consists of a title page first. Then, for each radial station, all the input quantities described above are listed, including the lift and drag data as well as the following computed quantities:

TABLE IX

INPUT PUNCH FORMAT - PROGRAM PROPERFM

Input Quantity	Field Spec.
IM, ID, IY	16I5
NUMRUN, NUMCASE	16I5
NB, NRB, NXAL, NXCL	16I5
RP, RHB, PTS	10F8.5
RB(1) - RB(NRB)	10F8.5
B(1) - B(NRB)	10F8.5
CDℓ(1) - CDℓ(NRB)	10F8.5
MN(1) - MN(NRB)	10F8.5
REN(1) - REN(NRB)	10F8.5
XAL(1) - XAL(NXAL)	10F8.5
XCL(1) - XCL(NXCL)	10F8.5
ICDCURVE(1) - ICDCURVE(NRB)	16I5
YCL(1,1) - YCL(1,NXAL)	10F8.5
YCD(1,1) - YCD(1,NXAL)	10F8.5
.	
.	
.	
YCL(NRB,1) - YCL(NRB,NXAL)	10F8.5
YCD(NRB,1) - YCD(NRB,NXAL)	10F8.5
PROPID(1) - PROPID(10)	10A8

TABLE IX-contd.

CUB(1) - CUB(NRB)	10F8.5
SUB(1) - SUB(NRB)	10F8.5
SWB(1) - SWB(NRB)	10F8.5
BETA(1) - BETA(NRB)	10F8.5
CDFAC	10F8.5

the Glauert variable of the radial station, the nondimensionalized blade chord, the total local velocity seen by the station, the angle between the rotational velocity and total velocity, the local blade angle of attack, the local lift and drag coefficients, the local blade circulation Γ, the nondimensionalized value of $-N\Gamma/4\pi r$ from the local Γ, and the radial derivatives of the thrust and power coefficients. On a first summary page, all the above computed quantities are repeated, and the integrated thrust and power coefficients and figure of merit are presented. On a second summary page, the data on the first summary page are repeated but with the drag coefficients all set identically equal to zero. Finally, the integrated induced thrust and power coefficients and figure of merit are presented.

Program MRCHINFO

This program was abstracted from INFLOWPT and assumes knowledge of most of the same basic data. There is some flexibility in the use of MRCHINFO, but we have selected the mode that gives the total influence functions at a number of inflow points as well as the trajectory.

Specify (IM), (ID), (IY), (NUMRUN), (TITLE), (IW), (JW), (XW), (RW), (UW), (VW), (WW), (UFS), (UFAC), (VFAC), (WFAC), (RH), (NB), (NI), (RI), (NSTEPSTR), (NINCSIZE), (STEPSTRT), (XCUTOFF), (ERR), (NSTEP) and (STEP) exactly the same as for program INFLOWPT. Specify further a case number (ICASE). Use the following values: for (INFO), 2; for (IDATA), 1. Specify the coordinate of the desired trailing vortex element (VORTEXPT). This coordinate may be expressed in blade radii or in the Glauert variable in degrees, provided the latter is greater than 1°. Specify a factor (CONTRFAC) that multiplies VW uniformly to provide for a different amount of contraction than that fixed by the basic VW field.

The punch format for program MRCHINFO is given in Table X and includes the input quantities and the field specification.

The print-out of MRCHINFO consists of the following: a title page; the axial, radial, and tangential velocity components of the stored input; and identification of the number of steps at each of the marching step time increment sizes. For the trailing element the following are printed out: at each step of the march, the coordinates and velocity components together with the cumulative contributions to the axial, radial, and tangential influence

TABLE X

INPUT PUNCH FORMAT-PROGRAM MRCHINFO

Input Quantity	Field Spec.
IM, ID, IY	16I5
INFO, IDATA	16I5
NUMRUN, ICASE	16I5
TITLE(1) - TITLE(10)	10A8
IW, JW	16I5
XW(1) - XW(IW)	10F8.5
RW(1) - RW(JW)	10F8.5
UW(1,1) - UW(IW,1) . . . UW(1,JW) - UW(IW,JW)	10F8.5
VW,(1,1) - VW(IW,1) . . . VW(1,JW) - VW(IW,JW)	10F8.5
WW(1,1) - WW(IW,1) . . . WW(1,JW) - WW(IW,JW)	10F8.5
UFS(1) - UFS(JW)	10F8.5
UFAC(1) - UFAC(JW)	10F8.5

TABLE X-contd.

VFAC(1) - VFAC(JW)	10F8.5
WFAC(1) - WFAC(JW)	10F8.5
CONTRFAC	10F8.5
VORTEXPT, RH	10F8.5
NB,NI	16I5
RI(1) - RI(NI)	10F8.5
NSTEPSTR, NINCSIZE, STEPSTRT,XCUTOFF, ERR	2I5,3F8.5
NSTEP(1) - NSTEP(NINCSIZE)	16I5
STEP(1) - STEP(NINCSIZE)	10F8.5

functions at all the inflow points; the contributions to the total influence functions from the deformed portion of the trajectory; and the total influence functions.

APPENDIX II

BLADE CHARACTERISTICS

Three propellers are considered in the text for both theoretical calculations and comparison with test data; namely, the four-bladed Canadair 65 Activity Factor and 120 Activity Factor propellers and the three-bladed Curtiss-Wright 3(109652) propeller. The digits within the parentheses of the latter refer to the blade design. The geometries and characteristics of these blade designs are given in Figures 16 through 18, with h/b as the local blade thickness-to-chord ratio and

$$AF \equiv \frac{100,000}{16} \int_{0.2}^{1.0} \frac{b}{2R_p} \left(\frac{r_p}{R_p}\right)^3 d\left(\frac{r_p}{R_p}\right) \tag{27}$$

$$IC_{L_i} \equiv 4 \int_{0.2}^{1.0} C_{L_i} \left(\frac{r_p}{R_p}\right)^3 d\left(\frac{r_p}{R_p}\right) \tag{28}$$

where

AF is the activity factor of the blade,

IC_{L_i} is the integrated design lift coefficient of the blade, and

C_{L_i} is the blade sectional design lift coefficient (Ref. 6, pp. 2 - 5, for example).

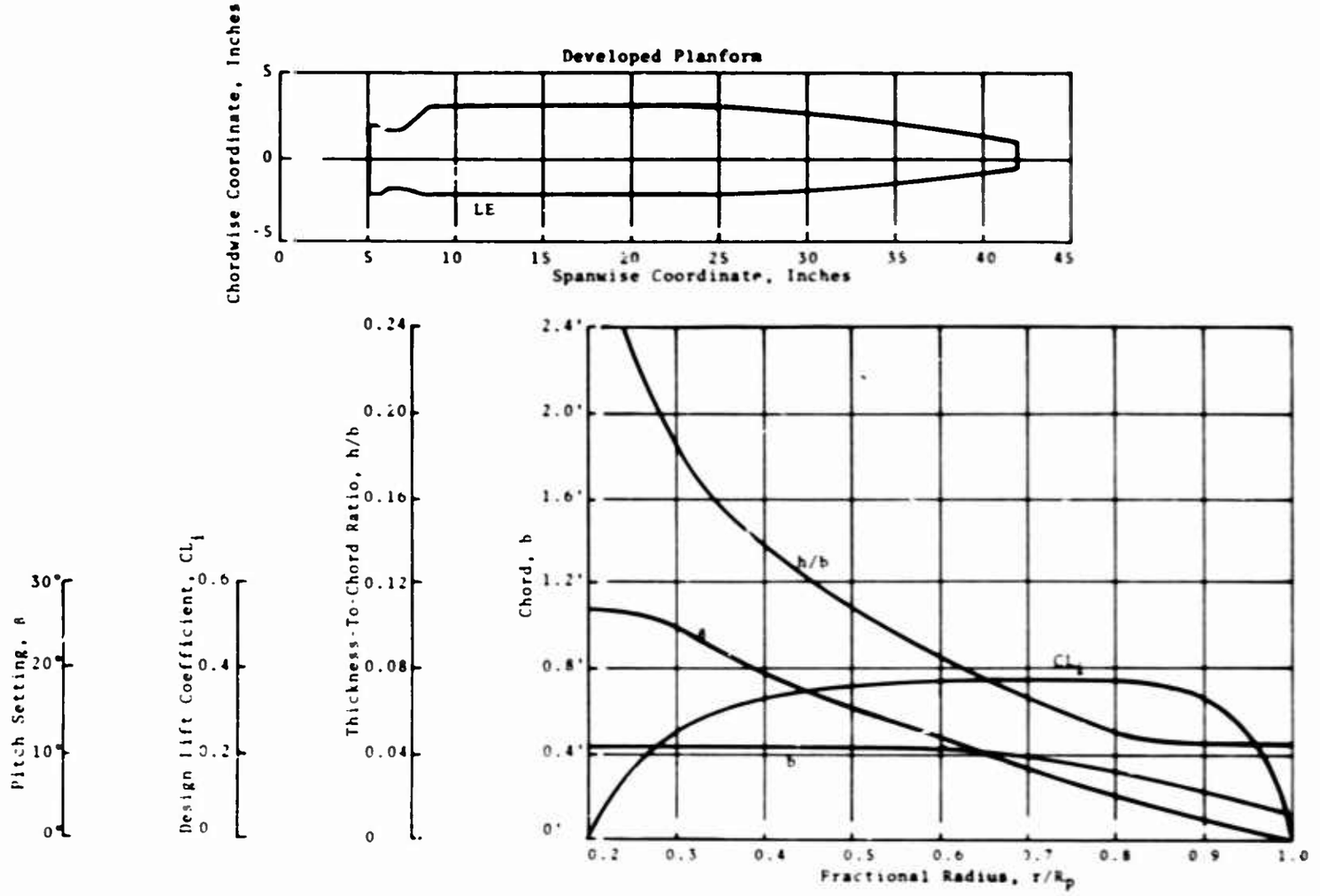

Figure 16. Blade Characteristics, 65 AF Design, NACA 65-Series Sections, $2R_p$ = 7'0", AF = 65, IC_{L_i} = 0.320.

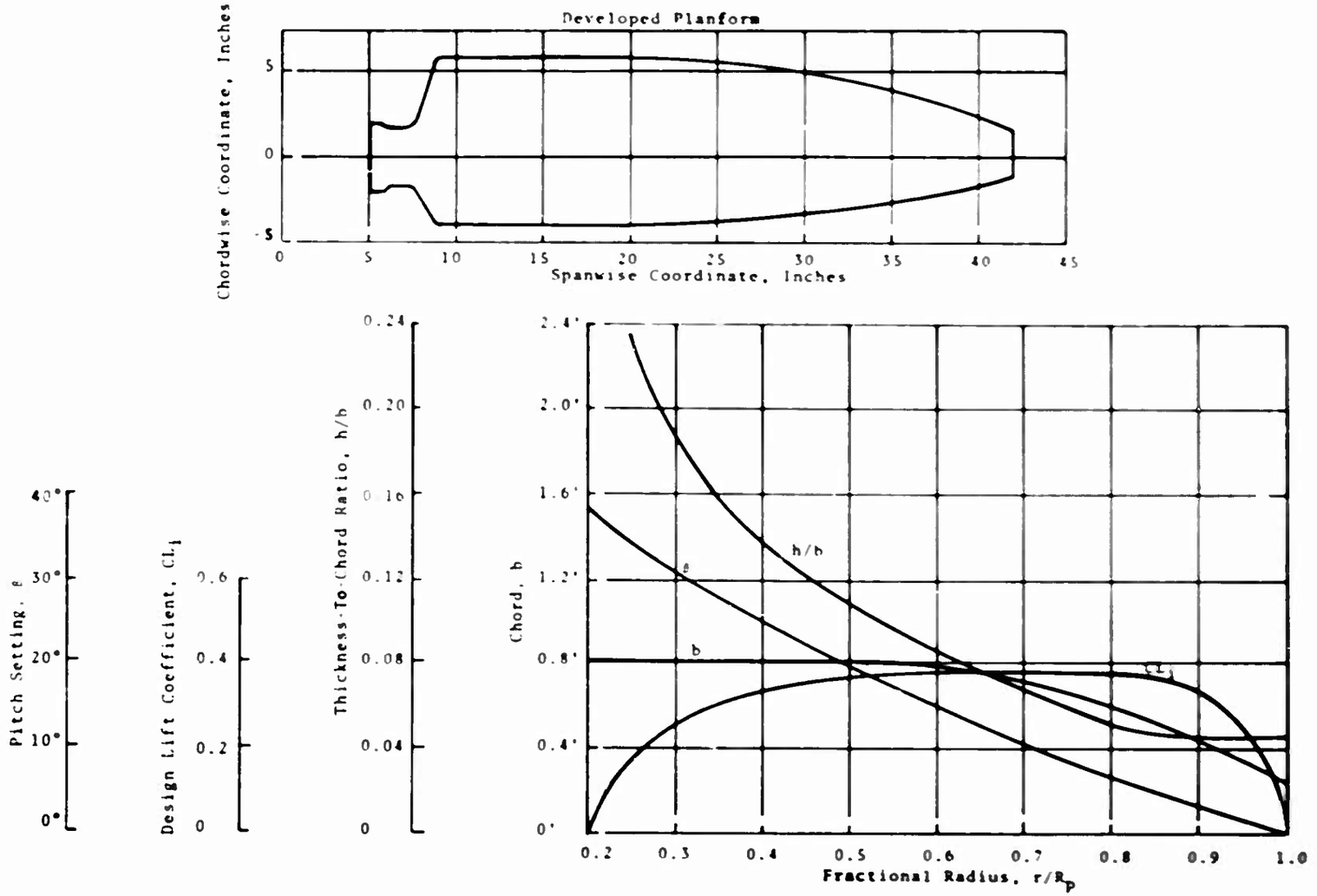

Figure 17. Blade Characteristics, 120 AF Design, NACA 65-Series Sections, $2R_p$ = 7'0", AF = 120, $^{IC}L_i$ = 0.320.

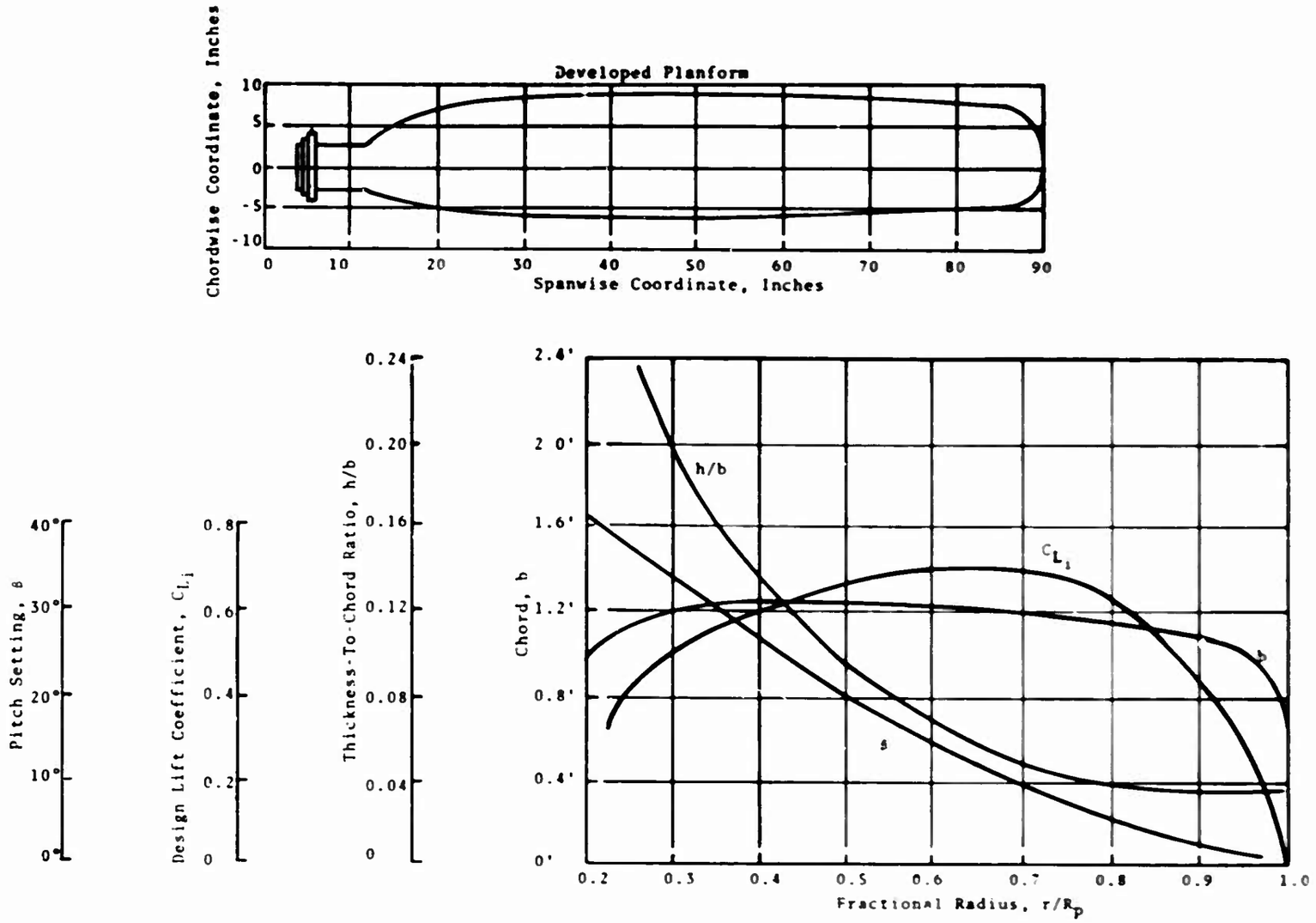

Figure 18. Blade Characteristics, 109652 Design, NACA 65-Series Sections, $2R_p$ = 15'0", AF = 115, IC_{L_i} = 0.500.

APPENDIX III

RESULTS OF INSTANTANEOUS WAKE VELOCITY MEASUREMENTS

In the experimental portion of this investigation, the instantaneous velocity components in the wakes of the 65 AF and 120 AF propellers at one pitch setting each were measured by means of hot-wire anemometry. The Canadair, Ltd., static thrust facility was used, and the performance was measured for these propellers over a range of pitch settings. The full details of the acquisition and reduction of the data are contained in the test report prepared by D. C. Gilmore and I. S. Gartshore of McGill University, Ref. 14.

However, subsequent to the preparation of Ref. 14, the basic velocity-voltage calibration procedure was reexamined. This led to a redetermination of the calibration constants in terms of true voltage instead of the voltage read on the hot-wire control unit. The velocity components, as reduced on the basis of the revised calibration, showed appreciable changes, which will be seen in the presentation of results that follows. These changes display clearly the importance of accurate velocity-voltage calibrations, which is emphasized in Ref. 14.

The instantaneous axial and radial components of the velocity at various field points behind the 65 AF propeller, operating at the 8.2° pitch setting and a tip speed of 800 feet per second, are presented in Figure 19. The corresponding results for the 120 AF propeller at the 10.0° setting and a 700-foot-per-second tip speed are given in Figure 20. These components, nondimensionalized with propeller tip speed, are plotted as a function of the azimuthal coordinate θ in propeller-fixed coordinates, rather than as a function of time in the space-fixed coordinates in which they were actually measured. Note that for convenience the negative of the radial component has been plotted. The tangential component is not presented because it is so much smaller in magnitude than the other two components that it cannot be resolved accurately; see Ref. 14. The data that are presented were reduced on the basis of the revised calibration constants, with the original results of Ref. 14 included for comparison. The algebraic sign of the differences between results based on the original calibrations and those based on the revised calibrations depends upon the particular hot-wire probe used. The significance of the repeated data points is discussed on pp. 29 and 30 of Ref. 14.

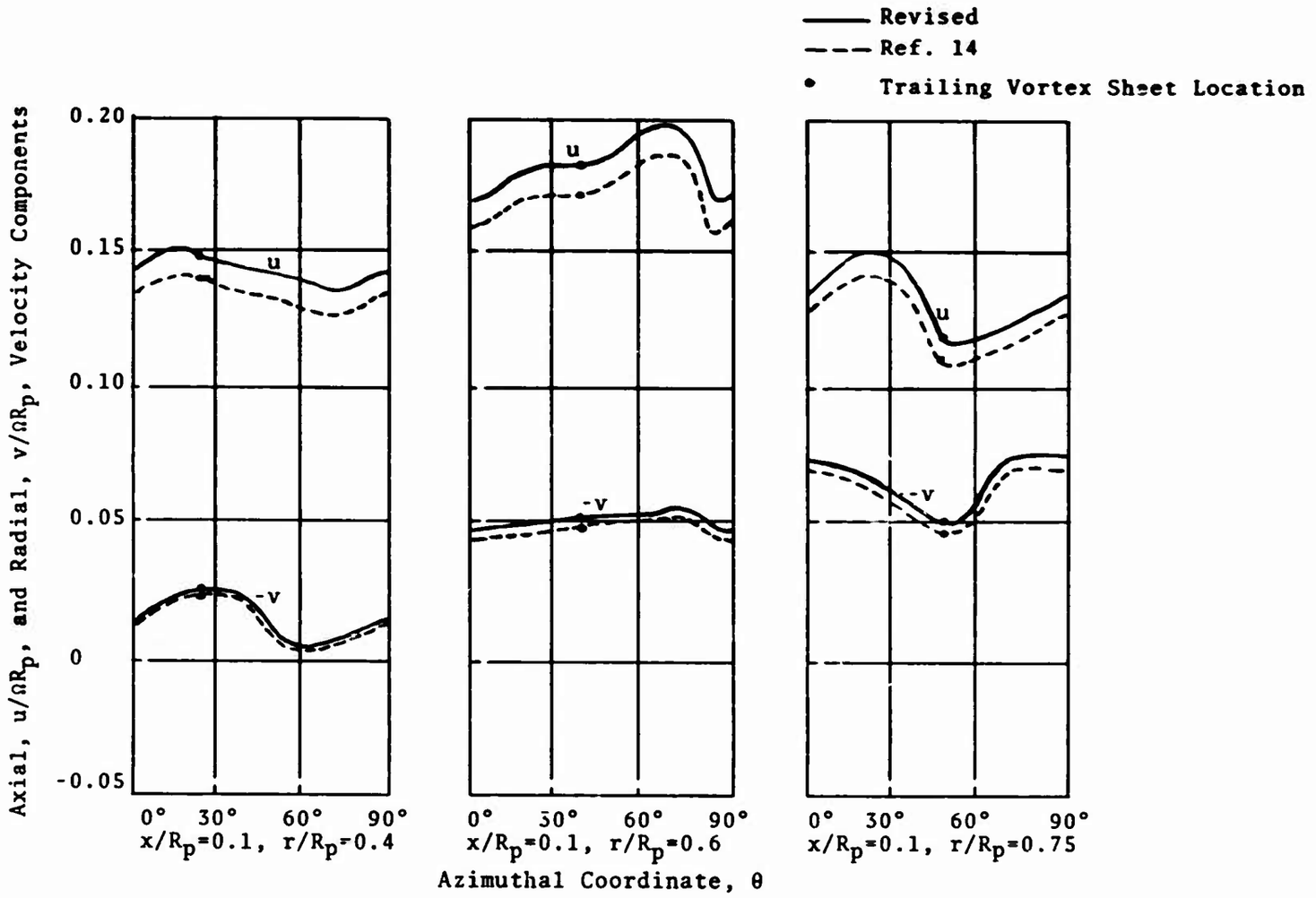

Figure 19. Azimuthal Variation of Measured Instantaneous Axial and Radial Velocity Components; 65 AF Propeller, $\beta 0.7R_p = 8.2°$, $\Omega R_p = 800$ fps.

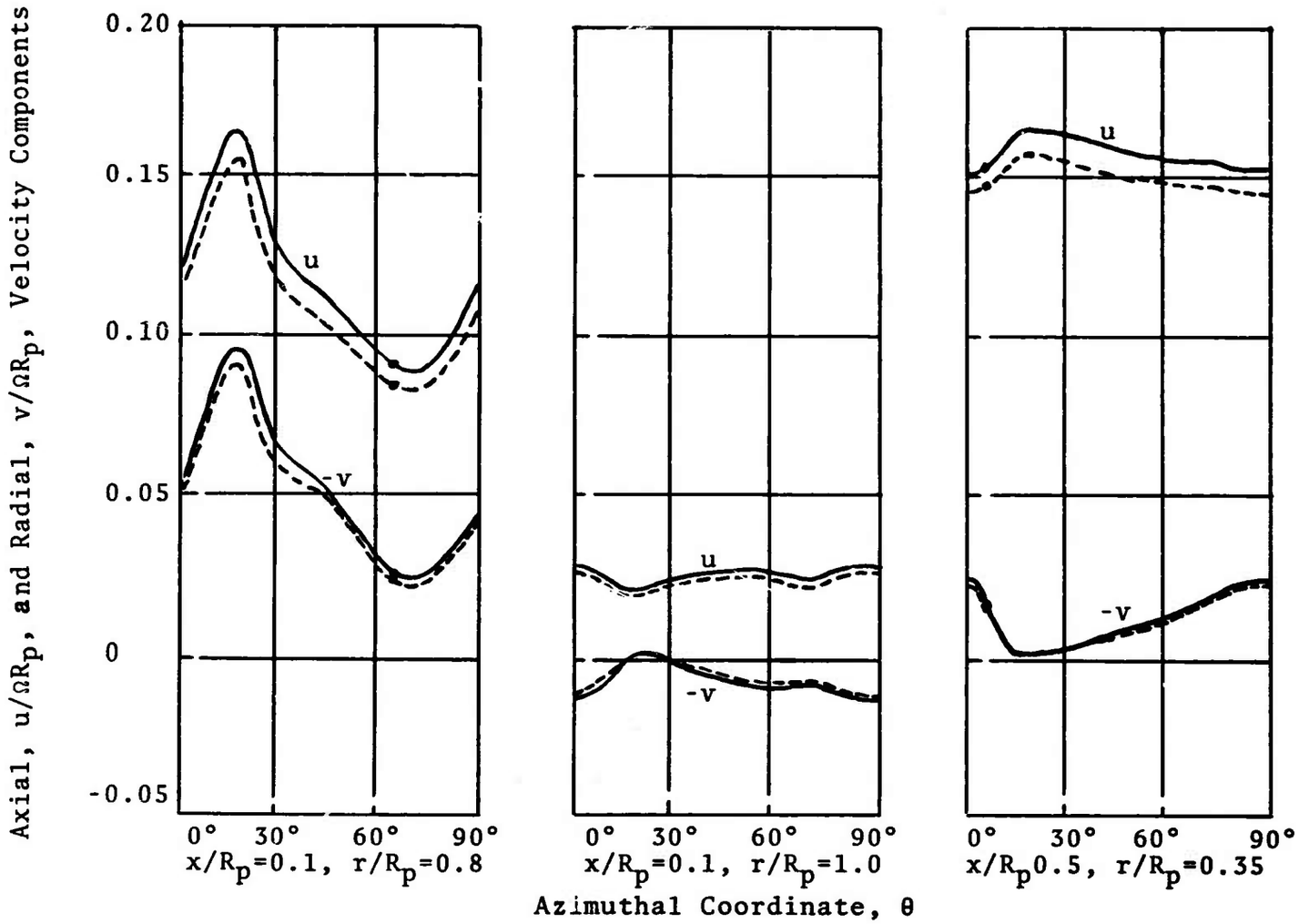

Figure 19. Contd.

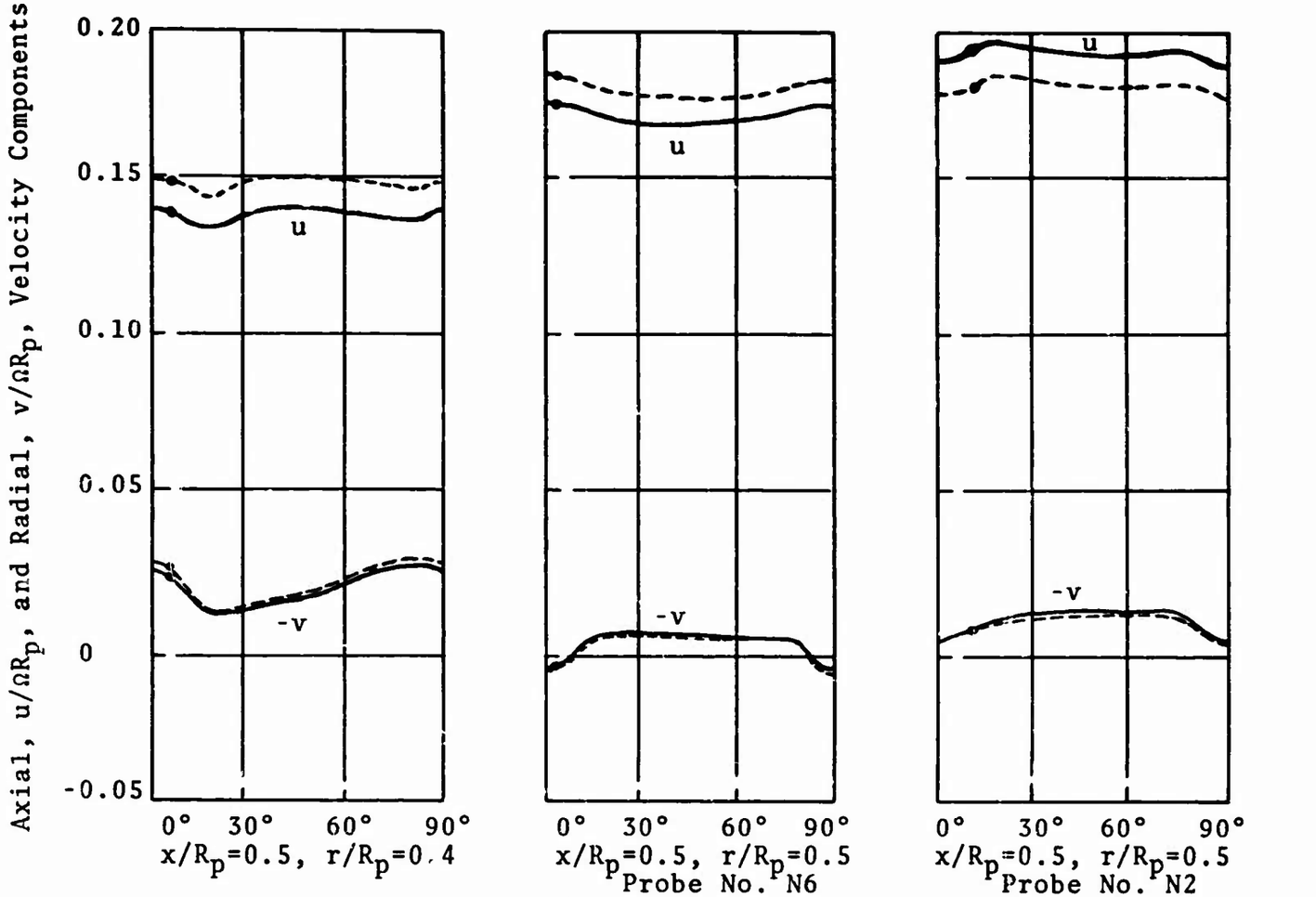

Figure 19. Contd.

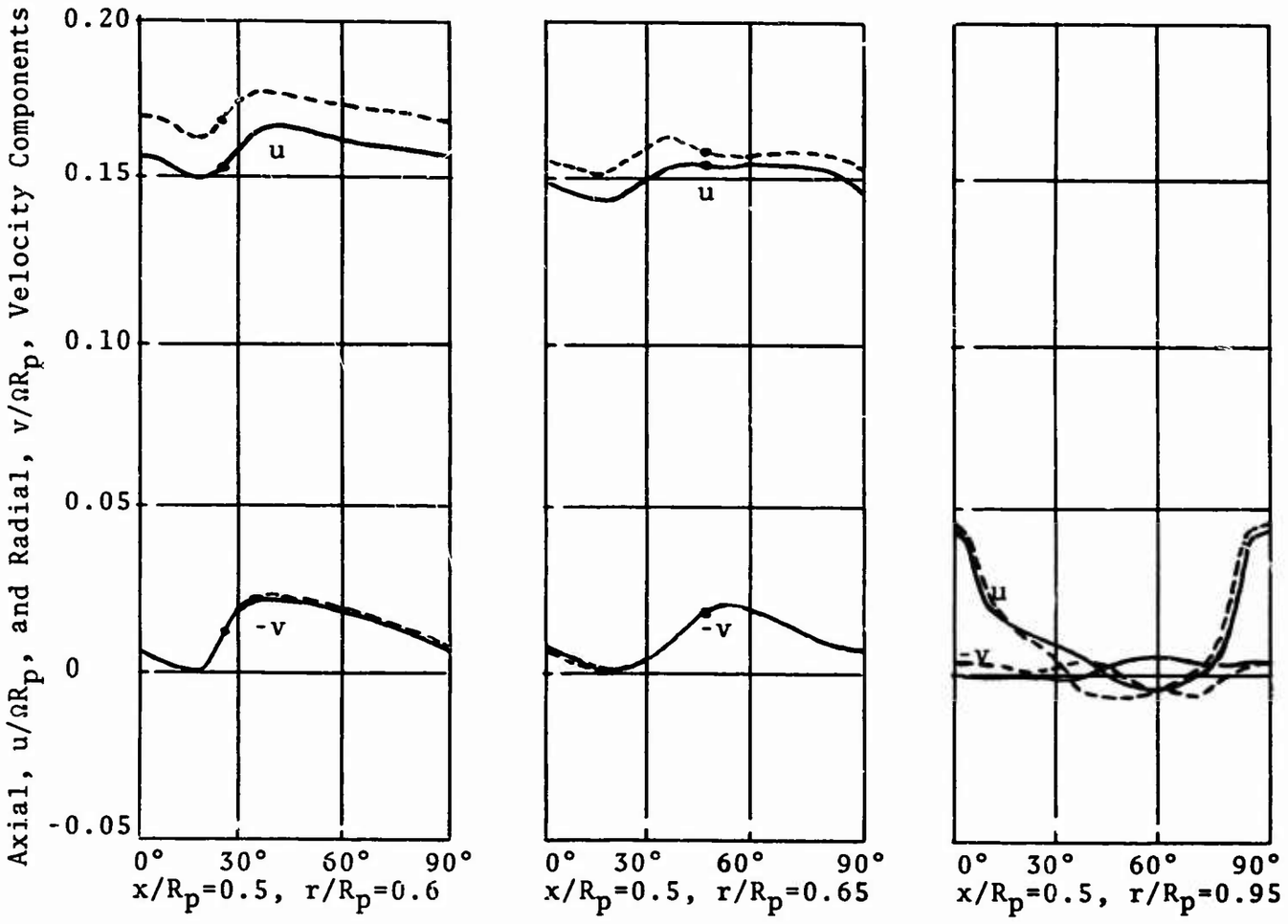

Figure 19. Contd.

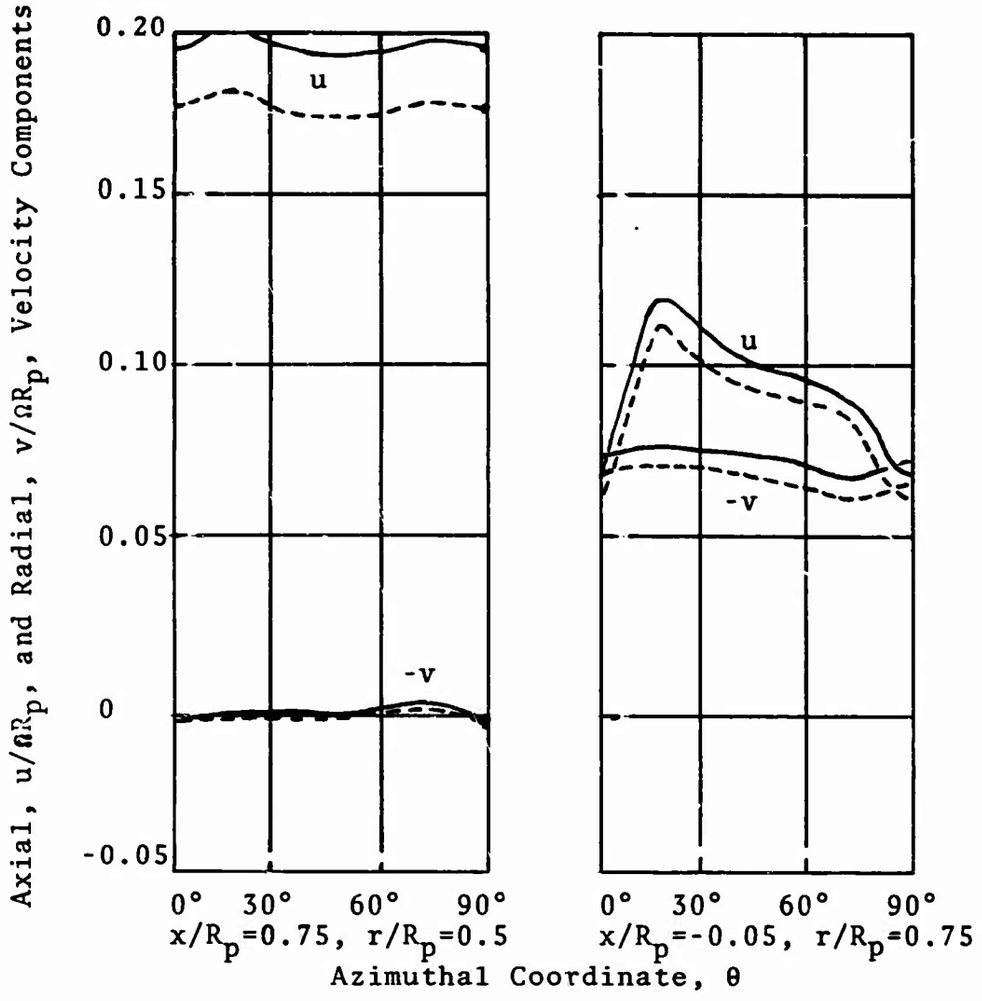

Figure 19. Contd.

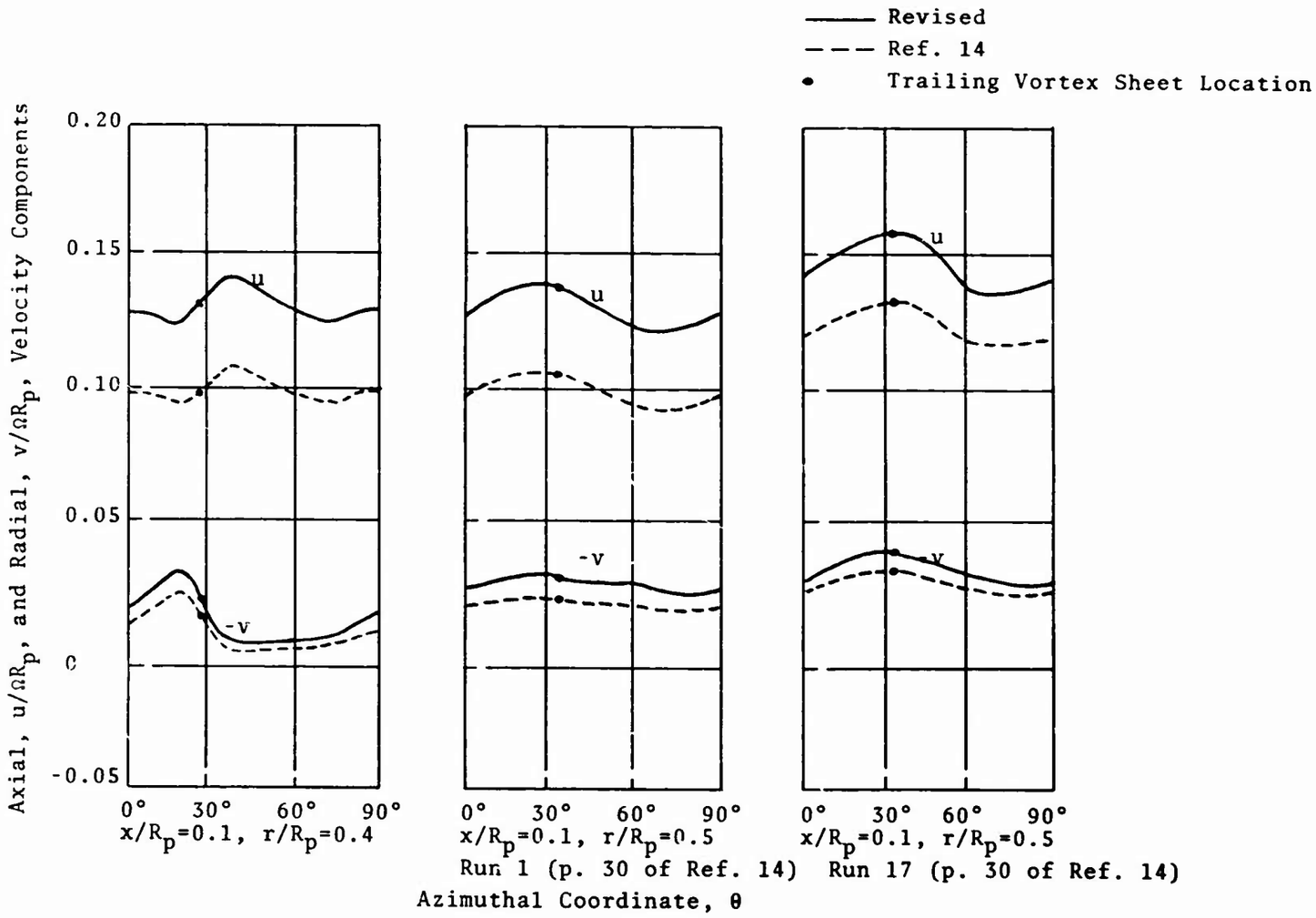

Figure 20. Azimuthal Variation of Measured Instantaneous Axial and Radial Velocity Components; 120 AF Propeller, $\beta 0.7R_p$ = 10.0°, ΩR_p = 700 fps.

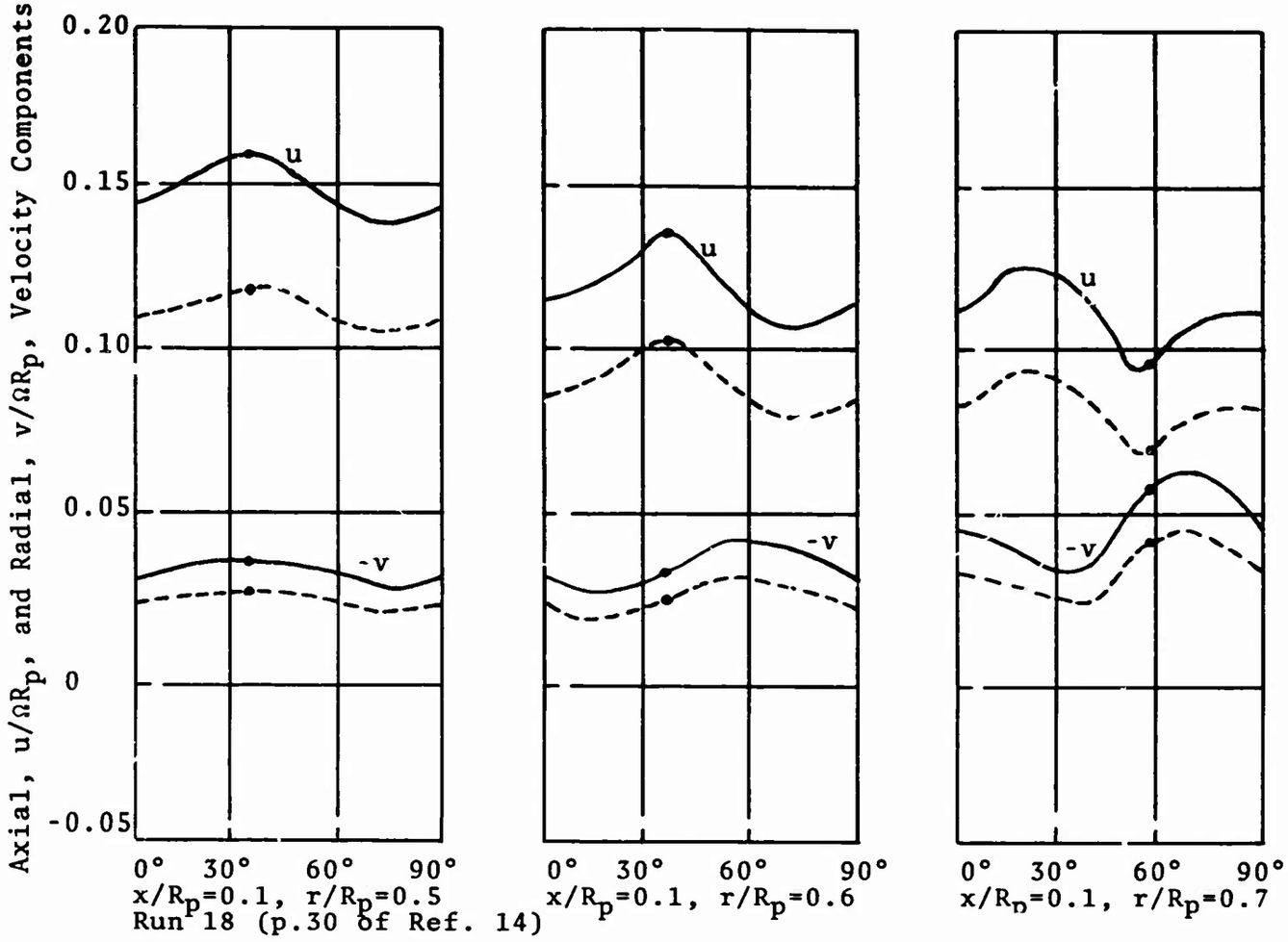

Figure 20. Contd.

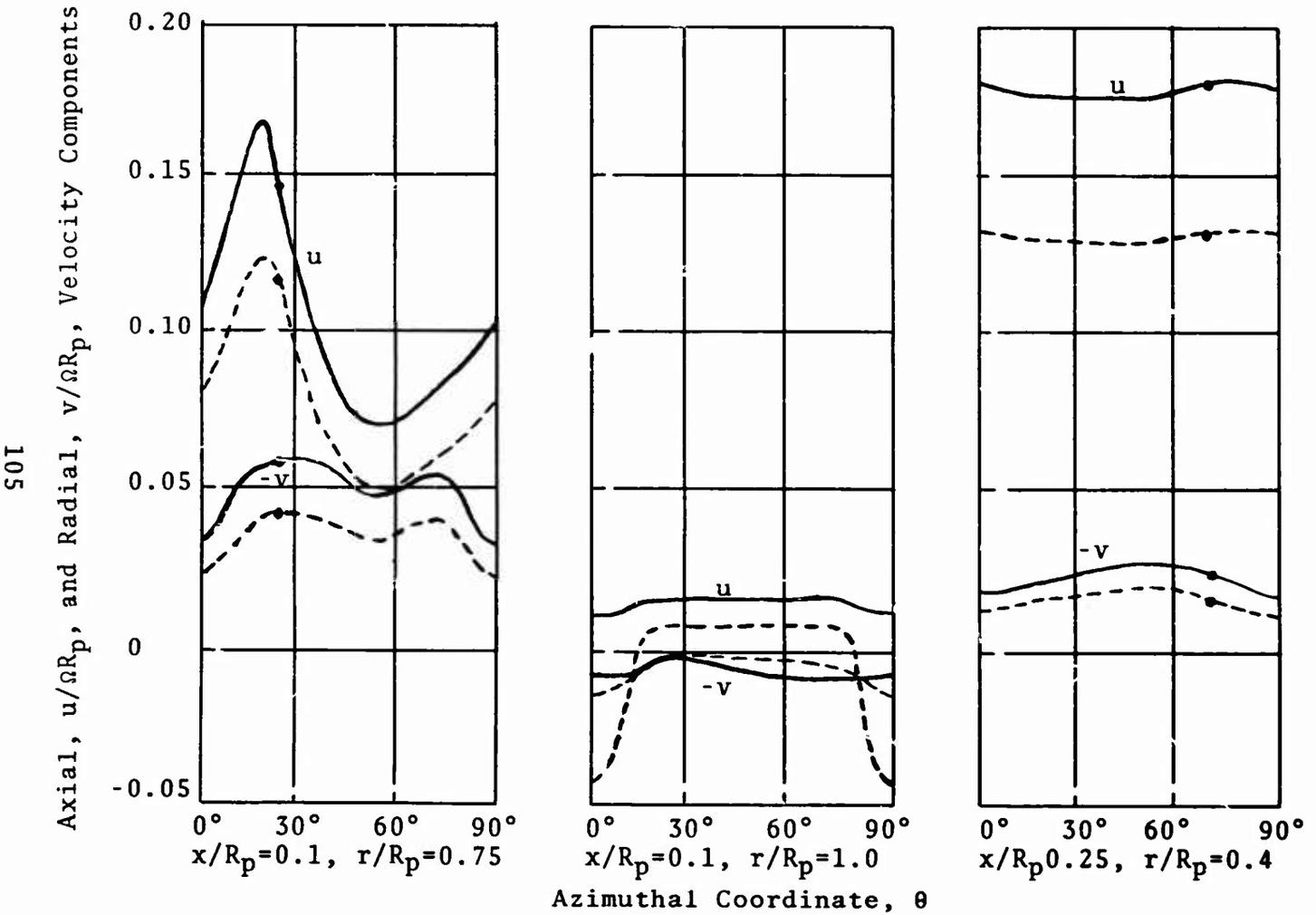

Figure 20. Contd.

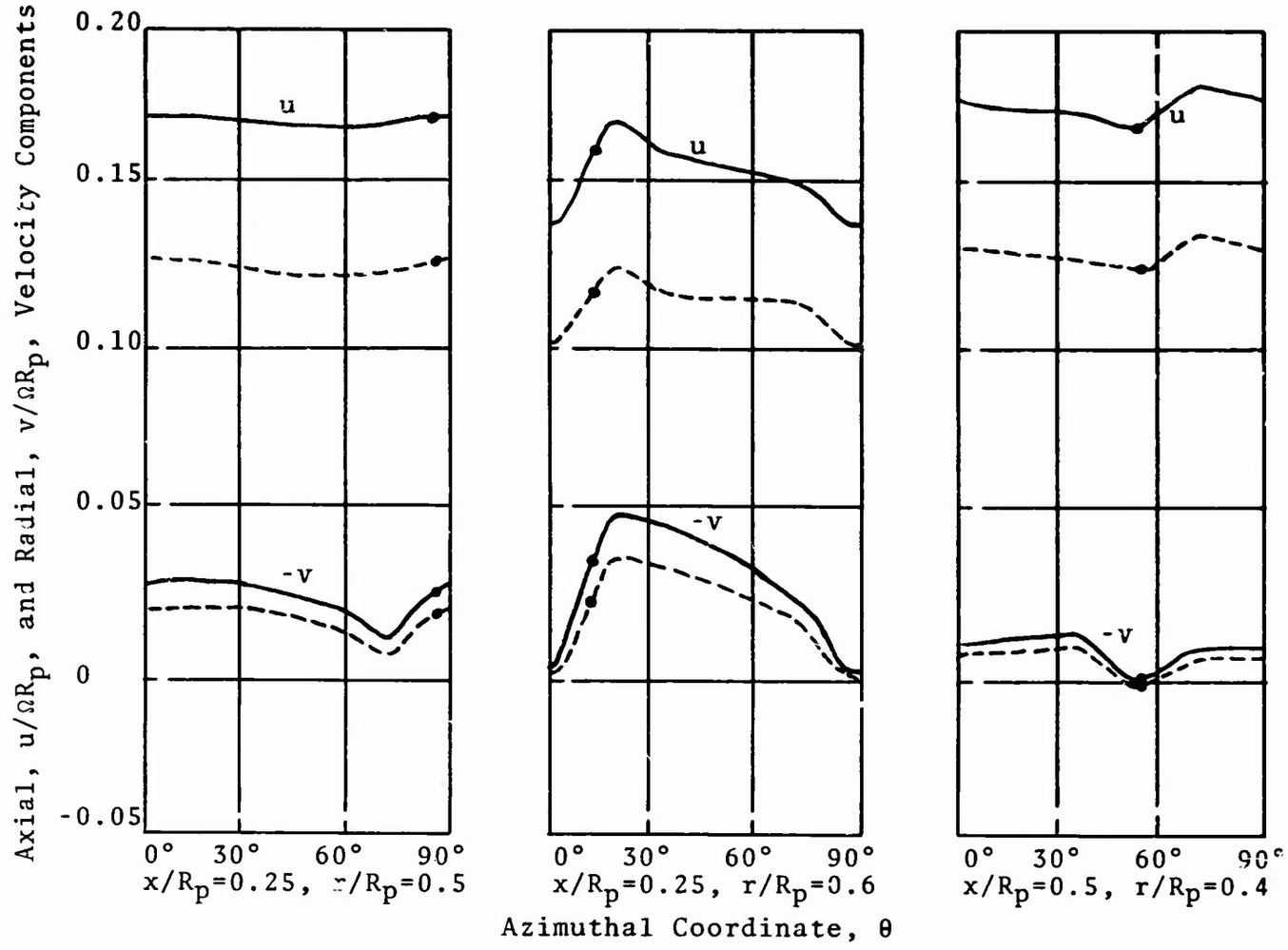

Figure 20. Contd.

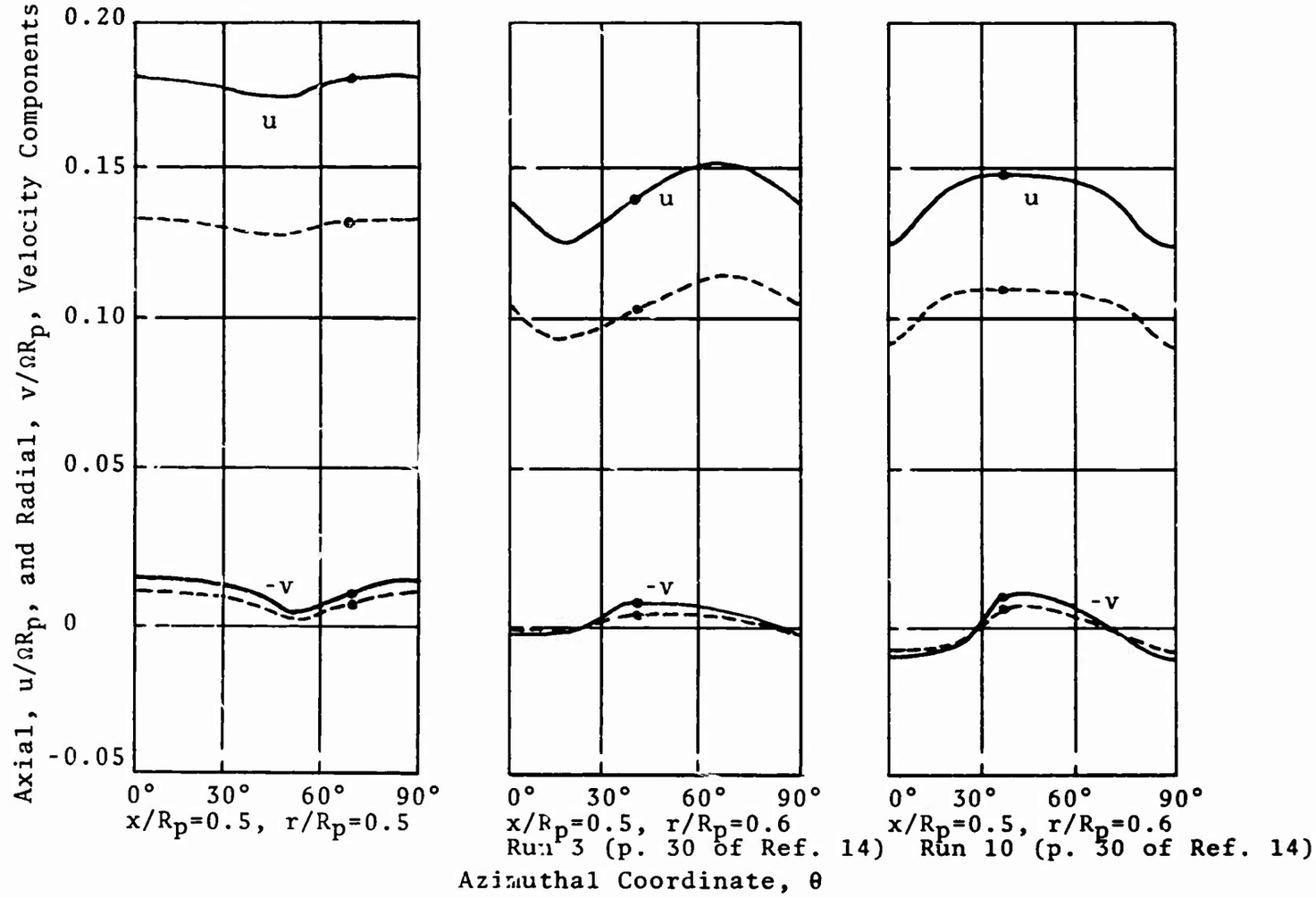

Figure 20. Contd.

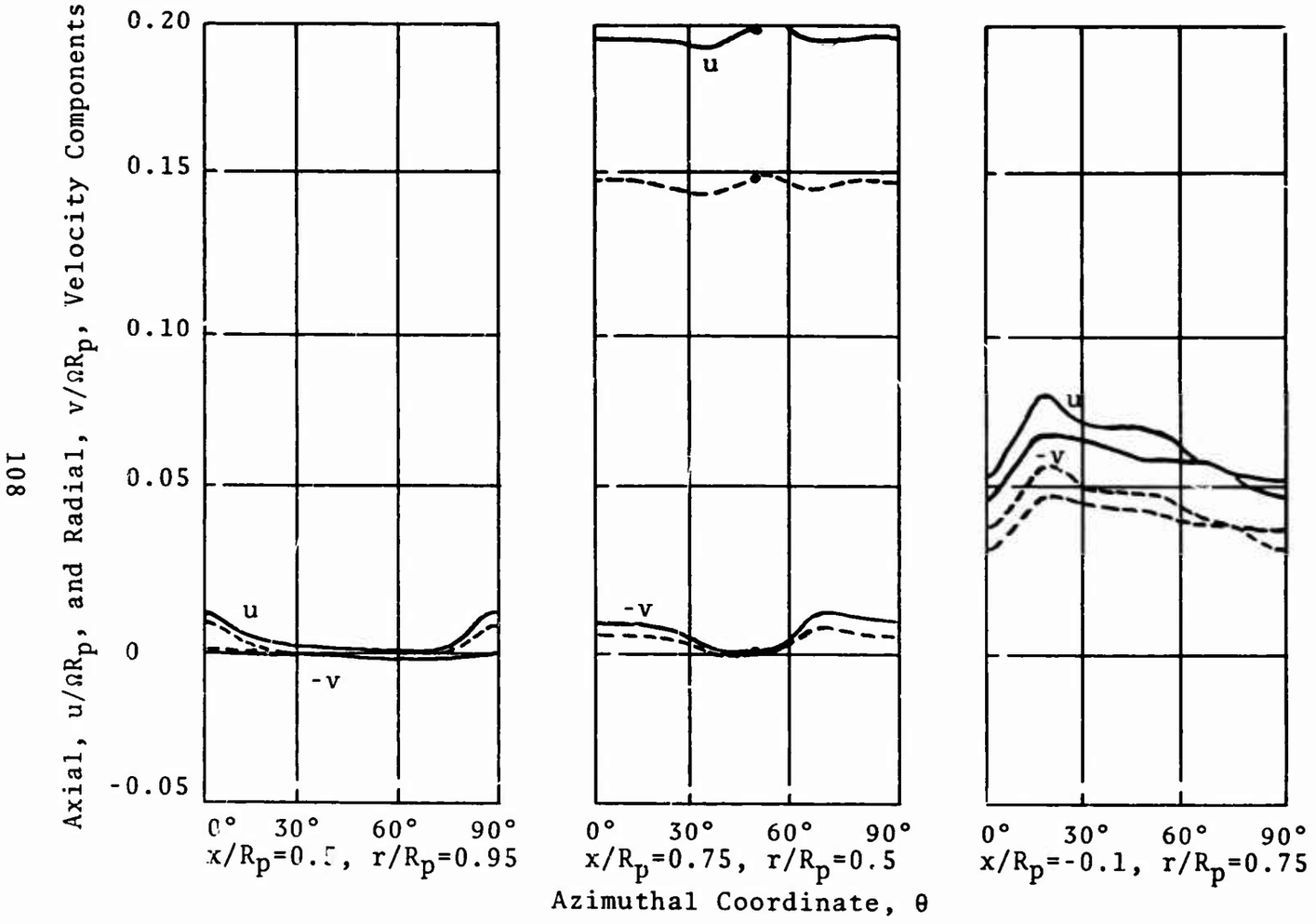

Figure 20. Contd.

For further discussions of the wake data, see the sections in Chapters 4 and 6 concerning the 65 AF propeller at the 8.2° pitch setting and the 120 AF propeller at the 10.0° pitch setting, respectively.

Unclassified
Security Classification

DOCUMENT CONTROL DATA - R & D

(Security classification of title, body of abstract and indexing annotation must be entered when the overall report is classified)

1. ORIGINATING ACTIVITY (Corporate author) Therm Advanced Research, Inc. Ithaca, New York	2a. REPORT SECURITY CLASSIFICATION Unclassified 2b. GROUP

3. REPORT TITLE

THEORETICAL AND EXPERIMENTAL INVESTIGATIONS OF V/STOL PROPELLER OPERATION IN A STATIC CONDITION

4. DESCRIPTIVE NOTES (Type of report and inclusive dates)

Final Report

5. AUTHOR(S) (First name, middle initial, last name)

John C. Erickson, Jr.

6. REPORT DATE	7a. TOTAL NO. OF PAGES	7b. NO. OF REFS
October 1969	125	31

8a. CONTRACT OR GRANT NO.	9a. ORIGINATOR'S REPORT NUMBER(S)
DA 44-177-AMC-379(T) b. PROJECT NO. 1F162204A142 c. d.	USAAVLABS Technical Report 69-55 9b. OTHER REPORT NO(S) (Any other numbers that may be assigned this report)

10. DISTRIBUTION STATEMENT

This document is subject to special export controls, and each transmittal to foreign governments or foreign nationals may be made only with prior approval of US Army Aviation Materiel Laboratories, Fort Eustis, Virginia 23604.

11. SUPPLEMENTARY NOTES	12. SPONSORING MILITARY ACTIVITY
	U. S. Army Aviation Materiel Laboratories Fort Eustis, Virginia

13. ABSTRACT

Successful design of propeller-driven V/STOL aircraft requires precise calculation and associated optimization of propeller performance in static operation. A general theory for performance prediction has been formulated based on continuous vortex representation along the lines of a classical lifting-line model. As opposed to forward flight, deformation of trailing vortex wake is appreciable just behind the propeller, and its determination constitutes the heart of the static thrust problem. Emphasis has been placed on determining a satisfactory force-free approximation to effective pitch of the trailing vortex sheets with the contraction pattern fixed according to a heavily loaded actuator disk theory. Numerical techniques and computer programs have been developed to calculate inflow to the propeller and velocity induced along arbitrarily described deformed trailing vortex sheets. In numerical calculations for a series of specific propellers and representative blade loadings, iterations were made on effective pitch variations and inflow. Comparisons of predicted and measured performance were not completely satisfactory for the pitch iterations, but indications were that the amount of contraction should also be iterated. Techniques for gathering and reducing instantaneous hot-wire measurements of wake velocity were developed. Measurements were carried out for two propellers, and nonrepeatable data were obtained in large regions behind the propellers. Theoretical calculations could not be iterated successfully in these cases, so significant theoretical and experimental comparisons could not be made. Detailed observations have been made on the character of the numerical computations, and certain generalizations have been made which lead to computational simplifications.

DD FORM 1 NOV 68 1473 REPLACES DD FORM 1473, 1 JAN 64, WHICH IS OBSOLETE FOR ARMY USE.

Unclassified
Security Classification

14. KEY WORDS	LINK A		LINK B		LINK C	
	ROLE	WT	ROLE	WT	ROLE	WT
Propeller Theory						
Rotor Theory						
Static Thrust Performance						
Propeller Tests						
Hot-Wire Anemometry						
Vortex Sheets						
V/STOL Propellers						

END

10016-69